Novel Plasma-based Ambient Desorption/ionization Source

A dissertation submitted in partial fulfillment
of the requirements for the degree of
PhD in Electronics and Electrical Engineering

The Graduate School of Science and Engineering
Doshisha University

Joey Kim Tumbali Soriano

September 2019

Synopsis

Ambient plasma-based ambient desorption/ionization source enables direct analysis of samples under ambient conditions that traditional atmospheric pressure ionization is incapable. It overcomes the tedious preprocessing and often detrimental and complicated sample introduction to the mass spectrometer for analysis. Existing plasma-based ambient desorption/ionization sources feature an electrical discharge typically formed between two electrodes by applying either a direct-current (DC) voltage or an alternating-current (AC) voltage with frequencies ranging from kilohertz to several megahertz. In this study, a novel plasma-based ambient desorption/ionization consists of a wire stabilized atmospheric pressure plasma produced by inductive coupling operated at very low power density supplied by a 13.56 MHz RF source. The ignition characteristics, stability and plasma properties of the wire stabilized atmospheric pressure plasma were studied.

In Chapter 2, the feasibility of low power production of atmospheric pressure plasma by inductive coupling are presented. Traditional inductively coupled plasma is operated at low pressure using high power and high gas flow. At high pressure, the plasma requires higher power and higher gas flow compared with low-pressure plasma. The stability of the atmospheric pressure plasma inductively coupled plasma is discussed in Chapter 3. In Chapter 4, improvements using external magnetic field is investigated. Further improvements using wire stabilization atmospheric pressure plasma is discussed in Chapter 5. Diagnostics of the ignition characteristics and stability are presented in Chapter 6. The possibility of simultaneous probe monitoring while being used for ion mobility spectrometer applications is studied in Chapter 7.

Acknowledgement

Once upon a time, a small boy from a small rural village in the Philippines started to learn about the name of the month, days, and year. He would browse old calendars like a children's book and everyday was captivated by the images featured in each page. When he got a little older, he learned that the beautiful images are from different cities in Japan. He dreamed and hoped that one day, he will visit those enchanting places. Today, that little boy is living his dream. It was not accident that I learned about Japan at a very early age. I believe that it's my destiny and part of my destiny is to meet people who supported me and made this dissertation possible. It is with my greatest gratitude and appreciation to acknowledge these people.

To **Professor Motoi Wada**, for his guidance, knowledge, and encouragement throughout my stay at Doshisha University. I am grateful for not giving up on me even though I have given up on myself. He has given me a lot of opportunities to bounce back when I often commit mistakes. I am greatly honored to be one of his advisees.

To **Monbusho Scholarship**, for their generous provision of my tuition and living allowance during my three years as a Ph.D. student in Japan.

To the faculty and members of **Plasma Physics Laboratory** at Doshisha University for all the support and motivation. Special thanks to **Takashi Torii**, who has always been there in helping me in ignition characterization of the atmospheric pressure plasma device and teaching me valuable insights especially in electronics. Special mention to **Kota and Maca** for helping me jumpstart my dissertation topic. To **Jhoelle and James**, for helping me polish my presentation and print my dissertation.

To team Hunny Flats, **Ino, Anton, Don, Nica, Minh, and Mano** for all the Pizza nights, Movie nights, Mario cart nights and many more. I am grateful for making my Japan life bearable. To my friends, **Bei, Cafa, Arn, Allen, Keano, Allie, James, and Maca** for all the helpful insights, dinners, and get-togethers. To all the members of **Assembly Kyoto Church**, for all the prayers and support.

To my family **Mama, Ate Hazel, Ate May, Ate Kate, and Maeleen**, for all the love and encouragement, for being extremely supportive, you are my inspiration!

Above all--- to God be all the glory, honor and praise!

ありがとうございました。*Thank you very much.* Maraming Salamat.

Table of Contents

Novel Plasma-based Ambient Desorption/ionization Source i

Synopsis iii

Acknowledgement iv

Table of Contents v

List of Tables ix

List of Figures x

Chapter 1 Introduction 1

1.1 Overview 1

1.2 Objectives and Motivations 4

1.3 Organization 5

Chapter 2 Design of Atmospheric Pressure Inductively Coupled Plasma 6

2.1 Desorption/ionization 6

2.1.1 An alternative method using inductive coupling 9

2.2 Introduction to inductively coupled plasma 10

2.2.1 Fundamentals of ICP 10

2.2.2 History of ICP 11

2.2.3 Theory of ICP 13

2.3 Design of ICP 14

2.3.1 Impedance matching network 14

2.3.2 Device assembly 16

2.3.3 Successful ignition 17

2.3.4 Effects of capacitance loading 19

2.3.5 Effects of coil size 20

2.3.6 Effects of stray inductance....21

2.3.7 Effects of coil distance....23

2.4 Summary....25

Chapter 3 Modes of Operational Mechanism....26

3.1 Introduction....26

3.2 Plasma filamentation....27

3.2.1 Homogenous glow mode of operation....27

3.2.2 Optical emission spectroscopy....28

3.2.3 Ion mobility spectrometer....30

3.3 Summary....35

Chapter 4 Magnetic Enhancements....36

4.1 Introduction....36

4.2 Theory....37

4.3 The orientation of the magnetic field....38

4.4 Experimental set-up....40

4.5 Qualitative evidence: plasma plume....41

4.5.1 Image analysis at position A....41

4.6 Quantitative evidence: ignition....43

4.7 Using permanent magnets....48

4.8 Summary....50

Chapter 5 Wire Stabilized Atmospheric Pressure Plasma....51

5.1 Floating wire....51

5.2 Experimental set-up....52

5.3 Enhanced ignition....53

5.4 Longer plasma plume....55

5.5 Signal stability 57

5.6 Summary 62

Chapter 6 Electric Probe Measurements of Atmospheric Pressure Plasma 63

6.1 Introduction 63

6.2 Double probe 65

6.2.1 Description of the probe 65

6.3 *I-V* measurements 66

6.3.1 Electron temperature 69

6.3.2 Space potential 71

6.4 Counter double electrostatic probe 72

6.4.1 Asymmetric in *I-V* measurements 73

6.4.2 Hysteresis 75

6.4.3 Signal fluctuation 77

6.5 Summary 80

Chapter 7 Electric Probe Measurements for Simultaneous Spectrometer Analysis 81

7.1 Introduction 81

7.2 *I-V* symmetry 82

7.3 Summary 84

Chapter 8 Conclusions 85

8.1 On the design of atmospheric pressure inductively coupled plasma 85

8.2 On plasma stability 88

8.3 On magnetic enhancements 89

8.4 On wire stabilized atmospheric pressure plasma 90

8.5 On electric probe measurements 90

8.6 On electric probe monitoring for simultaneous spectrometer applications 91

8.7 Further work.....92

References.....93

List of Tables

Table 1 Calculated ion mobility and the possible ion species of homogenous glow plasma and filamentary discharge. 34

List of Figures

Figure 2.1 Major instrumentations in desorption/ionization. 6
Figure 2.2 Schematic diagram of (a) direct analysis in real-time (DART), (b) flowing atmospheric pressure afterglow (FAPA), (c) low-temperature probe (LTP) and (d) direct barrier discharge ionization (DBDI). DART and FAPA use DC while LTP and DBDI use AC voltage [1]. 8
Figure 2.3 Schematic diagram of atmospheric pressure ICP coupled with a mass spectrometer. 9
Figure 2.4 Schematic diagram of the (a) ICP and the induced alternating magnetic field and the actual image of the plasma plume [14]. 10
Figure 2.5. Effects of resonance frequency to the (a) mode of discharge and (b) minimum sustaining power of Argon at various pressures. The schematic diagram of the (c) donut-shaped ICP discharge is shown with the corresponding skin depth [14]. 11
Figure 2.6 A schematic of Reed's induction plasma torch using a 26-mm outer diameter, air-cooled, quartz plasma confinement tube surrounded by a 5-turn, water-cooled, copper coil [11]. 12
Figure 2.7 Impedance matching circuit of inductively coupled plasma. 15
Figure 2.8 (a) Schematic diagram and (b) actual image of the atmospheric pressure ICP consisting of a 13.56 MHz RF power supply with a built-in matching network and plasma load enclosed inside an aluminum faraday shield. The plasma load consists of a copper coil inductor wound around a quartz glass tube connected to a 100 pF capacitor. 17
Figure 2.9 Plume images of the plasma excitation by inductive coupling using 3 L/min Ar gas for varied RF power. 18
Figure 2.10 Plume images of the plasma excitation by inductive coupling 40 W for varied gas flow rates. 18
Figure 2.11 Ignition characteristics of the low power atmospheric pressure plasma for varied Ar gas flow. 19
Figure 2.12 The decrease in the reflected power by variation of the loading of the CL· 20

Figure 2.13 Ignition characteristics of ICP as the copper coil wire diameter is varied. .21
Figure 2.14 Schematic diagram of the improved ICP with a built-in capacitor..... 22
Figure 2.15 The ignition characteristics for various capacitor used. The (a) ignition power, (b) sustaining power, (c) and reflected power measured using varied flowrates and (d) varied time. 23
Figure 2.16 Schematic diagram of the experimental set-up for changing the distance of the coil from the grounded base. 24
Figure 2.17 (a) Ignition power and (b) sustaining power and (c) reflected power measured when the coil position to the ground base is changed. 25
Figure 3.1 Transition from filamentary discharge to glow discharge at (a) top view and (b) side view. The reflected power is shown in the figure while the input power is kept at 70 W. 28
Figure 3.2 Homogenous glow plasma at varied RF power..... 28
Figure 3.3 The experimental set-up in measuring the optical spectra of the plasma plume. The optical fiber is placed at 50 cm distance from the tip of the plasma discharge. 29
Figure 3.4 Emission spectrum of the two modes of operation in the low power atmospheric pressure produced by inductive coupling. 30
Figure 3.5 Schematic set-up of the ion mobility and ion density measurements using Gerdien condenser. 31
Figure 3.6 Typical IV measurements using the Gerdien condenser. 32
Figure 3.7. Total ion density measurements using Gerdien condenser. 33
Figure 3.8 Positive ion spectrum of the filamentary discharge and homogenous glow plasma. 34
Figure 4.1 The orientation of the external magnetic field can be transverse or parallel to the plasma discharge. 39
Figure 4.2 (a) Schematic diagram of the magnet-assisted atmospheric ICP and (b) magnetic flux density in varied coil current. The copper coil used is not grounded which makes the plasma purely capacitively coupled. 41

Figure 4.3 Plume images for (a) positive magnet polarity and (b) negative magnet polarity. 42
Figure 4.4 Plume length measurements with increasing electromagnet current. 42
Figure 4.5 The effects of external magnets to the (a) ignition power and (b) sustaining power of the ICP. 43
Figure 4.6 (a) Schematic diagram of the experimental set-up when using the Gerdien condenser and the ICP is placed at position A. (b) Total ion density measurements for this experimental set-up. 44
Figure 4.7 (a) Schematic diagram of the experimental set-up when using the Gerdien condenser and the ICP is placed at position B. (b) Total ion density measurements for this experimental set-up. 45
Figure 4.8 (a) Schematic diagram of the experimental set-up when using the Gerdien condenser and the ICP is placed at position C. (b) Total ion density measurements for this experimental set-up. 45
Figure 4.9 The ion spectrum of the Ar plasma using (a) no external magnetic field, and with external magnetic field with intensity of (b) 60 Gauss, (c) 110 Gauss, (d) 170 Gauss, (e) 230 Gauss, (f) 290 Gauss, (g) 350 Gauss, and (h) 400 Gauss. 47
Figure 4.10 The position of external magnets in the ICP. 48
Figure 4.11 Magnetic field strength measurements from the tip of the nozzle. 48
Figure 4.12 (a) Plume length measurements and (b) intensity measurements of the Ar plasma with and without external permanent magnets 50
Figure 5.1 The wire stabilized atmospheric pressure plasma assembly. 53
Figure 5.2 Schematic of the experimental set-up in variation of ignition wire position. 54
Figure 5.3 (a) Ignition power, (b) sustaining power and (c) reflected power measured when the ignition wire tip position is changed with respect to the midsection of the copper solenoid coil. 55
Figure 5.4 Plasma plume images of the Ar atmospheric pressure plasma produced by inductive coupling without the use of ignition wire. The flowrate used is 3 L/min 56

Figure 5.5 Plasma plume images of the Ar atmospheric pressure plasma produced by inductive coupling using the ignition wire. The flowrate used is 3 L/min. 56
Figure 5.6 Schematic diagram of the Gerdien condenser coupled to the atmospheric plasma source. 57
Figure 5.7 Typical *I-V* measurements of the Gerdien condenser from the ICP with and without the ignition wire. 59
Figure 5.8 Amplitude measurements of the temporal change in ion current saturation with +5 V constantly applied voltage to the Gerdien condenser. 60
Figure 5.9 Fourier transform signal analysis using the Gerdien condenser. 61
Figure 6.1 Position (a) and description (b) of the electric probe. 65
Figure 6.2 Typical *I-V* measurements using the double probe. 66
Figure 6.3 Schematic diagram of the noise amplitude and offset. 67
Figure 6.4 Amplitude and offset measurements using varied RF power (a), Ar flow rate (b), and probe distance (c). 68
Figure 6.5 Negative and positive current saturation, and $|dI/dV|_{V=0}$ measurements using varied RF power (a), Ar flow rate (b) and probe distance (c). 69
Figure 6.6 Electron temperature measurements using increasing RF power for various Ar flowrate (a) and probe distance (b). 71
Figure 6.7 *I-V* curve (a) and current saturation and slope measurements (b) using a bias voltage in the ignition wire. 72
Figure 6.8 Schematic diagram of the counter double electrostatic probe. 73
Figure 6.9 *I-V* measurements of the Ar plasma using a 2 L/min gas flow rate. The RF power was varied from 20 W to 60 W. 74
Figure 6.10 Typical *I-V* measurements and the derivative of the *I-V* measurements using 50 W, 2 L/min. The asymmetry is apparent when comparing the values of the positive and negative current saturation. 75
Figure 6.11 Typical hysteresis in the *I-V* measurements of a single electric probe. Changes in current displacement and hysteresis area are measure with varying (b) time sweep. 76

Figure 6.12 Temporal variations of current saturation measure using an electric probe. 77
Figure 6.13 Decreasing current saturation through time. 78
Figure 6.14 (a) Ratio of the current saturation measured at 50 s and 10 s is correlated to the increase in coil temperature. (b) The y-axis range is decreased to 0.90-1.02 to give emphasis on the decreasing trend. 79
Figure 7.1 Double probe like structure in the upstream flow of Ar gas. 81
Figure 7.2 Typical *I-V* measurements. 82
Figure 7.3 Current saturation measurements and first derivative values for (a) varied Ar flowrates and (b) varied RF power. 83
Figure 7.4 *I-V* measurements using various RF power input. 84
Figure 8.1 The schematic diagram of the first design of the 13.56 MHZ RF atmospheric ICP that was developed as plasma-based ADI. 86
Figure 8.2 Schematic diagram of an improved design of the ICP with a built-in capacitor which minimized the stray capacitance and parasitic inductance in the circuit resulting in consistent temporal reflected power measurements. 86
Figure 8.3 Magnet-assisted atmospheric pressure ICP. 87
Figure 8.4 Wire-stabilized atmospheric pressure ICP. 88
Figure 8.5 schematic diagram of the wire stabilized atmospheric pressure plasma -mass spectroscopy 92

Chapter 1
Introduction

1.1 Overview

Desorption is a method that enables the production of intact heavy molecular ions from a condensed phase. The desorption of samples followed by ionization techniques produces the ions collected in the analytical device for separation, identification, and quantification of compounds present in the sample [1]. The desorption/ionization techniques could either be placed inside a vacuum (low pressure) or used in ambient conditions (atmospheric pressure). Desorption/ionization techniques in low pressure have the advantage of direct access between the ion source and the mass analyzer. This technique, however, requires sample processing and additional accessories such as ion gates and ion mobility spectrometers [2].

At atmospheric pressure, ions are directly created from the sample which is efficiently transferred from higher pressure into the mass analyzer. This method overcomes the complicated and often detrimental steps of pretreatments and sample preparations. The method classified between using spray based or plasma-based techniques [3]. For spray based technique, the well-known electrospray ionization (ESI) is often used [4]. This method generates ions from a solution of a sample by creating a fine spray of charged droplets from a fine, charged stainless steel capillary

needle. The needle is maintained at a high electric field by applying high voltage. The ions are transferred into the mass spectrometer inlet through a tiny capillary where the ions are analyzed. A major merit of ESI is that nonvolatiles and macromolecules can be ionized without fragmentation for analysis. This process of ionization is particularly helpful for mass spectroscopy of large biomolecules [4,5].

For the plasma-based techniques, the samples are inserted into the gap between the plasma source and mass spectrometer inlet [1,2,4]. The process produces protonated or deprotonated species when the afterglow from the plasma ionized the sample. Traditional atmospheric-pressure ionization such as liquid chromatography (LC) is not capable of direct analysis of samples under ambient conditions and usually requires some form of sample preprocessing and complicated introduction systems and transferred to the mass spectrometer inlet for analysis. The atmospheric pressure devices or also known as ambient desorption/ionization (ADI) sources were introduced to overcome these complicated and often detrimental steps by enabling direct analysis of samples under ambient conditions [6,7]. Characteristic for all ADI sources is their simple construction and, usually, easy interfacing with many types of mass spectrometers. Samples are desorbed/ionized in ambient air and transferred to the mass spectrometer inlet for analysis [4].

ADI has many advantages including simplicity, flexibility, portability, absence of solvents and high chemical activity. It also preserves the structural integrity of the molecules and provides molecular mass information and yields simple spectra for complex mixtures. There are important consequences with the increased number of atomic-molecular collisions in ADI due to the short mean free path. First, the influence of diffusion is reduced, leading to longer residence times in the source and enhanced chemical ionization efficiency. Second, excess energy generated during the ionization

reaction can be released through collisions with the buffer gas that helps to reduce fragmentation [8].

This dissertation presents a novel plasma-based ambient desorption/ionization source for ion mobility spectrometer (IMS) or mass spectrometry (MS). The plasma-based ADI source is a wire stabilized atmospheric pressure plasma operated by inductive coupling using a low power RF source. The feasibility of a low power inductively coupled plasma at atmospheric pressure was realized using the theoretical and experimental understanding of its fundamental instrumentation. Improvements of the ignition characteristics device by variations of the operational parameters were studied. Enhancements using an external magnetic field was attempted. Plasma stabilization using a grounded ignition wire instead of a previously studied floating wire lead to stable atmospheric pressure plasma. The ignition wire was discovered to play a crucial role in mitigating the undetermined plasma potential in the electric probe measurements. This lead to a new method of electric probe measurements in the upstream flow position where simultaneous electric probe measurements and ion mobility spectrometer analysis is possible.

Plasma-based ADI sources typically produce the electric discharge between two electrodes by applying either a direct-current voltage or an alternating-current voltage with frequencies ranging from kilohertz to several megahertz. The discharge is formed in a flowing gas, typically helium, but also argon, nitrogen, or air, which generates such reactive species as electrons, radicals, ionized or excited atoms, and molecules. The novel ADI source presented in this study, however, uses inductive coupling to produce the discharge. Inductively coupled plasma has been mainly used for materials processing, atomic emission spectrometry, and as a low-pressure plasma source in mass spectrometry. Moreover, typical inductively coupled plasma at atmospheric

pressure requires high power density and high gas flow input. An additional water cooling system is also expected which makes the device bulky and impractical for ambient MS or IMS applications.

Production of the atmospheric pressure plasma by inductive coupling in this study used low electrical input power and low gas flow rate made possible by pairing the inductive element to a capacitor and fine-tuning the impedance of the plasma load and the power supply. The system does not require a bulky water cooling system which makes it portable and easy to use. The wire electrode serves as the sensor to make a feed-back control of the plasma source while reducing initial ignition power to commence the discharge.

1.2 Objectives and Motivations

Direct analysis of solid and liquid samples without the tedious preprocessing and complicated sample introduction is of great interest, especially in organic chemical analysis. Ambient desorption/ionization sources realize this vision by creating the ions through direct exposure of the sample and efficiently transferring the ions from higher pressure into the mass analyzer. Ambient desorption/ionization has many advantages compared to traditional atmospheric pressure ionization including simplicity, flexibility, portability, absence of solvents and high chemical activity. It also preserves the structural integrity of the molecules and provides molecular mass information and yields simple spectra for complex mixtures [1].

Therefore, this research aims to establish the instrumentation of a novel ambient desorption/ionization source by inductive coupling instead of the traditional two electrodes.

1.3 Organization

This dissertation is composed of 5 main parts and 8 chapters after the introduction chapter. **Chapter 2** provides the fundamental theory related to plasma-based ambient desorption/ionization sources. Experimental results on the feasibility of low power production of atmospheric pressure plasma using inductive coupling are presented. The effects of the inductive element to the plasma ignition are also studied in **Chapter 2**. **Chapter 3** presents the plasma stability analysis of the ambient desorption/ionization source. Qualitative analysis such as plasma filamentation was investigated. Quantitative analysis such as **Chapter 4** discusses the improvements using an external magnet. **Chapter 5** presents the enhancements in the ambient desorption/ionization source using the wire stabilized atmospheric pressure plasma. **Chapter 6** use electric probe measurements for diagnostics studies of the atmospheric pressure plasma. **Chapter 7** showcase the new method of electric probe measurements where simultaneous electric probe measurements and ion mobility spectrometer analysis is possible. Finally, **Chapter 8** summarizes the research findings of this dissertation and recommends related further research.

Chapter 2
Design of Atmospheric Pressure Inductively Coupled Plasma

2.1 Desorption/ionization

Desorption/ionization coupled with mass spectrometry is a powerful technique for detecting low levels of chemical species with very high specificity. Samples in condensed phased undergo desorption/ionization to enable the production of intact heavy molecular ions which are transported to the mass analyzer for identification and quantification. The existing major instrumentations are classified between the low pressure and atmospheric pressure as shown in Figure 2.1. For devices using low pressure, solid samples can be directly analyzed by chemical ionization and matrix-assisted laser desorption/ionization. Devices using atmospheric pressure are further classified between spray based and plasma-based sources [1,9,10].

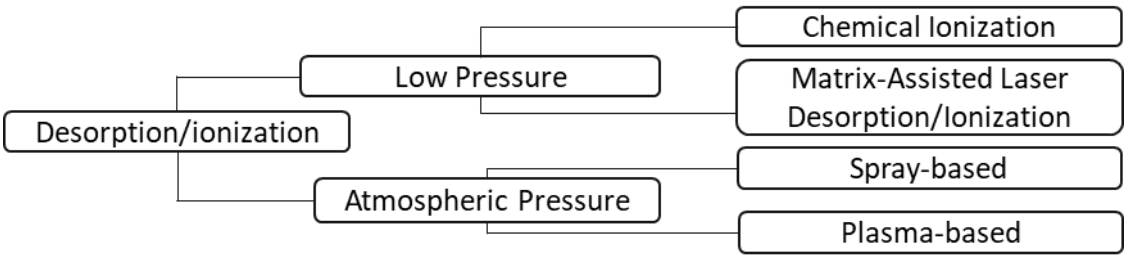

Figure 2.1 Major instrumentations in desorption/ionization.

In chemical ionization, collisions of ionized gases with the target analyte produce the ions which are separated according to mass and transported into the detector. The samples are required to be in the gas phase where solid and liquid samples undergo many steps of sample preparations before the analysis [9]. In matrix-assisted laser desorption/ionization, the sample which is co-crystallized with the organic matrix is irradiated with a UV laser/ causing the generation of an ion plume. The ions are transported into the mass separator then into the faraday cup detector [10].

Analysis of liquid samples can be more difficult and is often accomplished at atmospheric pressure using spray-based or plasma-based devices [1,3–5]. For spray-based devices, the method generates ions from a solution of the sample by creating a fine spray of charged droplets from a fine, charged stainless steel capillary needle [4]. The needle is maintained at a high electric field by applying high voltage. The ions are transferred into the mass spectrometer inlet through a tiny capillary where the ions are analyzed. For the plasma-based devices, the samples are inserted into the gap between the plasma source and mass spectrometer inlet [1]. The process is regarded as a soft ionization which produces protonated or deprotonated species when the afterglow from the plasma ionized the sample. In soft ionization, the sample undergoes several mechanisms including proton transfer, charge transfer, Penning ionization, ion or electron attachment, and proton abstraction.

Different types of plasma-based techniques shown in Figure 2.2(a)-(d) have slightly different ionization mechanisms due to the applied voltage used whether it is a direct current DC or alternating current AC [1,3,4,6]. For devices using DC, examples are direct analysis in real-time (DART) and flowing atmospheric pressure afterglow (FAPA) while low-temperature probe (LTP) and direct barrier discharge ionization (DBDI) use AC.

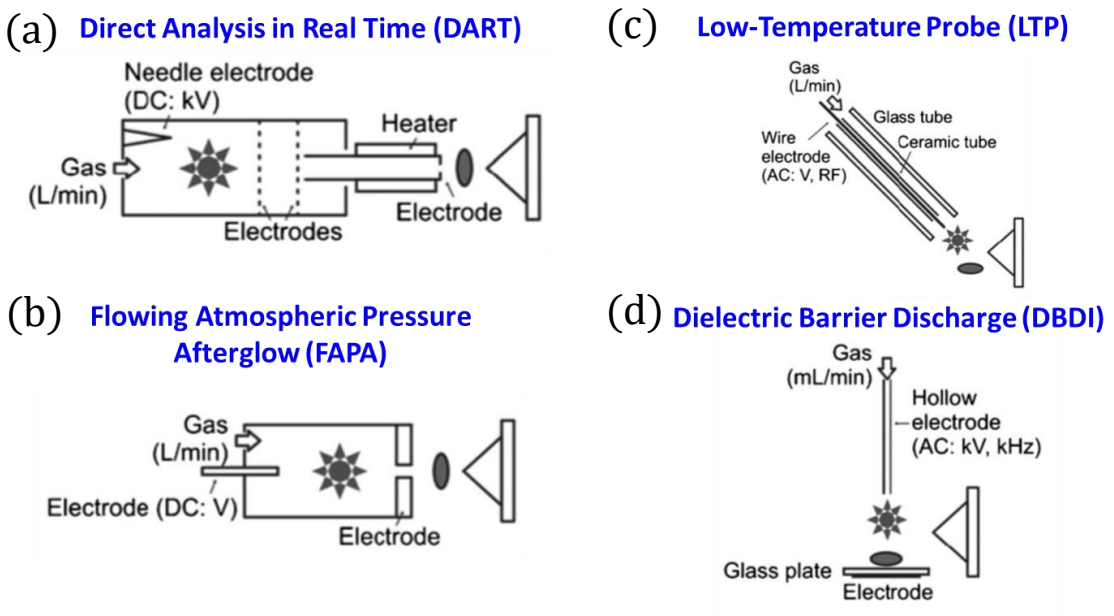

Figure 2.2 Schematic diagram of (a) direct analysis in real-time (DART), (b) flowing atmospheric pressure afterglow (FAPA), (c) low-temperature probe (LTP) and (d) direct barrier discharge ionization (DBDI). DART and FAPA use DC while LTP and DBDI use AC voltage [1].

The discharge in the DART source is localized in the enclosed discharge chamber and plasma-generated ions are partially filtered by use of one or two additional grid electrodes as shown in Figure 2.2(a) [2]. The discharge in the FAPA source is generated in the enclosed chamber between a pin cathode and a plate or capillary anode [Figure 2.2(b)]. Voltages in the kilovolt range are used and discharge gas, mostly helium, is introduced at liter-per-minute flow rates [1]. For the LTP, kilohertz AC voltages are applied to one of the electrodes, and the other is grounded [Figure 2.2(c)]. The electrodes are a pin electrode and a foil ring electrode separated by a dielectric barrier. The plasma is generated within the glass tube with its afterglow directly interacting with the sample. In many cases, additional heating of the sample is needed to enhance

thermal desorption and maximize the signal, because of the low temperature of the plasma [1,3,4].

The DBDI source shown in Figure 2.2(d) utilizes the same type of discharge with the power consumption of approximately 30 W. It features a glass plate as a dielectric barrier between a needle electrode and a plate electrode. In contrast with the LTP probe, samples are deposited directly on the dielectric barrier and the discharge is formed directly on the sample for analysis [6].

2.1.1 An alternative method using inductive coupling

In general, plasma-based ADI sources feature two electrodes which generate the ions for analysis. An alternative method to the discussed plasma-based ion sources is inductively coupled plasma (ICP) that could be coupled to an ion mobility spectrometer or mass spectrometer. The ICP-MS is not a new technique in low pressure. However, the coupling of atmospheric pressure ICP to mass spectrometer has never been done before. A schematic diagram of the atmospheric pressure ICP-MS is shown in Figure 2.3.

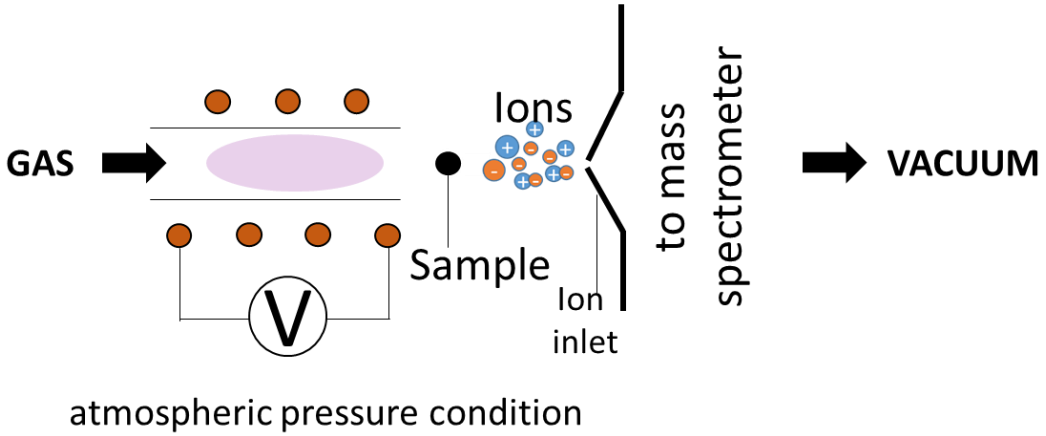

Figure 2.3 Schematic diagram of atmospheric pressure ICP coupled with a mass spectrometer.

2.2 Introduction to inductively coupled plasma

2.2.1 Fundamentals of ICP

The simple configuration of ICP uses a helical coil wound around a dielectric tube to couple energy from an RF power source to the discharge [Figure 2.4(a)]. Ignition of the plasma starts with excitation by the alternating magnetic field as a result of the conductance current in a closed loop. An example of an ignited plasma using ICP is shown in Figure 2.4(b). Major parameters in the design of an inductively coupled plasma torch are resonating frequency, skin depth, and energy coupling efficiency [11–13].

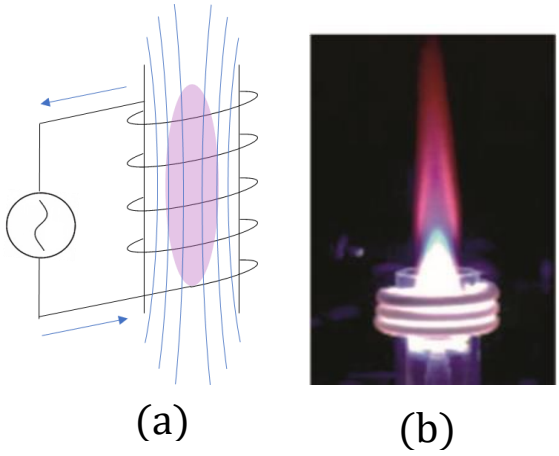

Figure 2.4 Schematic diagram of the (a) ICP and the induced alternating magnetic field and the actual image of the plasma plume [14].

The resonating frequency affects the energy coupling mechanism in the ICP. Two distinct energy coupling mechanisms are E-type discharges and H-type discharges. Figure 2.5(a) shows the power and frequency boundaries for these discharges. E-discharges are powered by electrostatic energy while H-type discharges are caused by electromagnetic energy. The E-type discharges use less power at low frequencies while

increasing the power cause H-type discharges. At high frequency and pressure [Figure 2.5(b)], minimum power is required to generate H-type-discharges [14].

Skin depth is the thickness where the energy is coupled to the outer shell of the load [Figure 2.5(c)]. It is a function of the average electrical conductivity of the plasma, the oscillator frequency, and the magnetic permeability of the medium. The skin depth is important for choosing the discharge opening of the plasma. With the increasing frequency, the skin depth decreased. For smaller tube diameter discharge opening, it requires high resonating frequency [11,15].

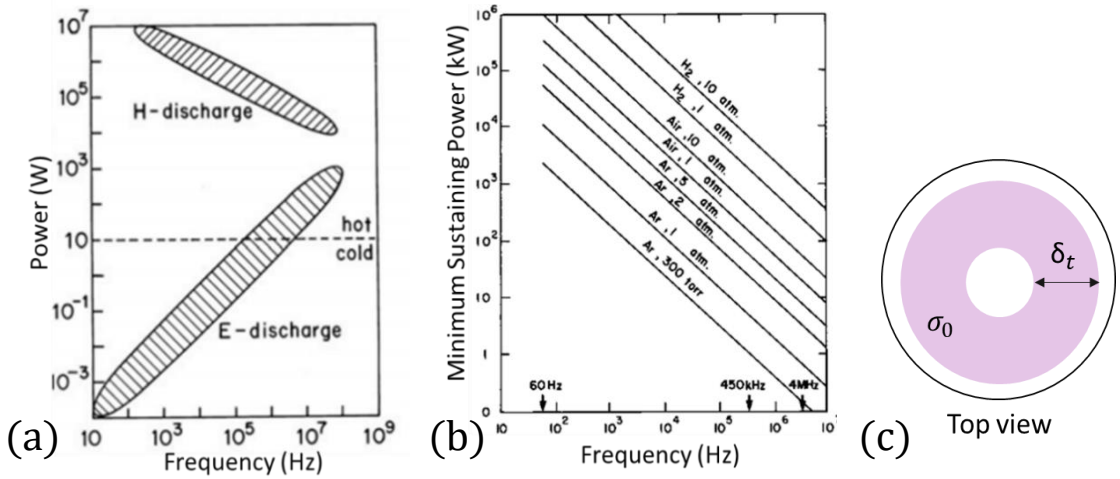

Figure 2.5. Effects of resonance frequency to the (a) mode of discharge and (b) minimum sustaining power of Argon at various pressures. The schematic diagram of the (c) donut-shaped ICP discharge is shown with the corresponding skin depth [14].

2.2.2 History of ICP

The study on inductively coupled plasma, which is often referred to as radiofrequency or high-frequency discharge started with Reed in 1961 [11]. He demonstrated that inductively coupled plasmas can be maintained in an open tube in the presence of gas flow. A schematic of Reed's induction plasma torch is shown in

Figure 2.6. This was built using a 26-mm outer diameter, air-cooled, quartz plasma confinement tube surrounded by a 5-turn, water-cooled, copper coil. Electric power was supplied to the coil by a generator having a maximum power output of 10 kW.

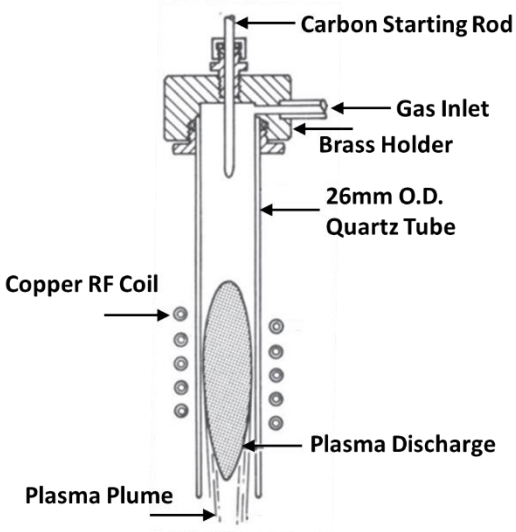

Figure 2.6 A schematic of Reed's induction plasma torch using a 26-mm outer diameter, air-cooled, quartz plasma confinement tube surrounded by a 5-turn, water-cooled, copper coil [11].

A lot of improvements have been made in ICP such as changes in the dielectric barrier, from a quartz dielectric barrier to the metal wall and ceramic wall torches. Also, improvements in the plasma mechanism are done using the DC-RF hybrid torch. Size reduction of the ICP system is still being considered as one of the easiest and better choice in improving ICP. The decrease in the tube diameter size results to lower power and gas consumption as revealed by advances in inductively coupled microplasmas. The microplasma shown is used by Sato and others using a 1mm discharge opening. The microplasma was used in VUV spectroscopy and optical emission spectrometer applications.

2.2.3 Theory of ICP

ICP couple the RF power source to the inductive elements to produce plasma. The inductive coupling element is driven in an electrical resonance condition where high potentials exist in the structure which makes ICP arguably entirely inductively coupled. In the low discharge power region, capacitive coupling predominates over inductive coupling; thus, the so-called ICP source actually operates in an electrostatic (E) mode in the ignition phase. In a high discharged power region, although capacitive coupling still exists, it contributes less than inductive coupling, and the discharge in this region is thus named the electromagnetic mode (H mode) [16]. In general, these high-density plasma sources which are only partly inductively coupled may be in the form of helical inductive couplers, helical resonators, spiral inductive couplers, immersed inductive couplers and transformer-coupled plasma.

The time derivative of the magnetic flux Φ determines the electric field.

$$E_\theta = \frac{1}{2\mathrm{R}} \frac{d\Phi}{dt} \tag{2.1}$$

while Φ is determined from the inductance L, current I, and the number of coil turns N.

$$\Phi = \frac{LI}{N} \tag{2.2}$$

For helical inductive couplers, the inductance (L) of the coil with N turns, radius R_c and length l, is approximated using Nagaoka coefficient $\aleph$ in the following equation:

$$L = \aleph \mu_0 \mu_s \pi {R_c}^2 \frac{N^2}{l} \tag{2.3}$$

where μ_0 is permeability in a vacuum. The particle motion is determined by the magnetic flux density B,

$$B = {}^{\Phi}/_{\pi R^2} \tag{2.4}$$

There are two components of the induced electric field, one along the axis of the solenoid (E_z) and one in the azimuthal direction (E_θ) derived using Faraday's law,

$$E_z = \frac{\mu_0 \omega N^2 \pi {R_c}^2 I}{l} \text{ and } E_\theta = \frac{R_c L}{2\pi R^2 N}\left(\frac{dI}{dt}\right) = \frac{\aleph \mu_0 \mu_s \omega N R I}{2l} \tag{2.5}$$

where ω is the frequency of the energy source. Under normal condition, $E_z > E_\theta$ until a breakdown in azimuthal direction occurs and E_z will be reduced by the plasma electrical conductivity.

The azimuthal electric field can become stronger as the distance R_c from the coil center becomes larger so that the electrons are strongly accelerated near the wall: $r = R_c$. Therefore, as the distance from the center of the coil increases, plasma with high electron density is generated and the ICP forms a donut-shaped plasma. Due to this phenomenon, an efficient introduction of the sample to the mass analyzer is possible.

2.3 Design of ICP

The basic principle of IPC used in atmospheric pressure is not different from low-pressure ICP. At atmospheric pressure, the inductively coupled plasma system is not enclosed in a vacuum chamber, the gas is introduced to the atmosphere to generate plasma. Excitation gas used in atmospheric pressure plasma includes various types of gases such as nitrogen, carbon dioxide, oxygen and helium in addition to argon. The type of gas is applied depending on the plasma application.

2.3.1 Impedance matching network

A crucial problem in the design of an RF discharge circuit is the efficient coupling of the RF power to the plasma source which can be achieved through a matching network. In general, the plasma load can be considered a combination of inductance L,

capacitance C, and resistance R. The built-in matching network consists of variable capacitors and inductors in series as shown in Figure 2.7. The efficiency of energy transfer between the electrical circuit and the plasma load depends on the proper tuning of the phasing and loading of variable capacitors C_1 and C_2. Tuning the phasing and loading of these variable capacitors results in high current flow, high power absorption, and low reflected power.

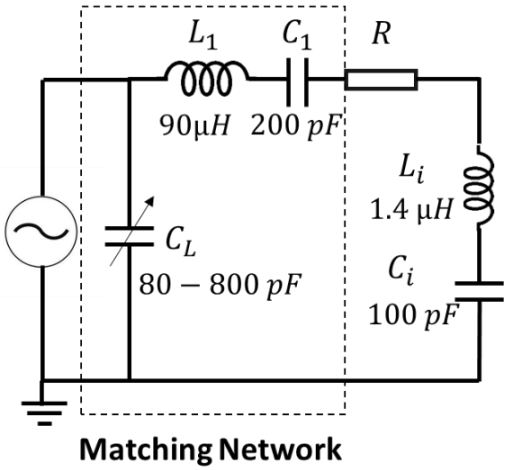

Figure 2.7 Impedance matching circuit of inductively coupled plasma.

The electric field formed inside the inductor is proportional to the current as shown in Equation 2.5. Considering the inductance and capacitance in the matching network and in the plasma assembly, the electric field in the power supply is

$$\begin{pmatrix} E \\ 0 \end{pmatrix} = \begin{pmatrix} \frac{1}{j\omega C_L} & -\frac{1}{j\omega C_L} \\ -\frac{1}{j\omega C_L} & j\left(\omega L - \frac{1}{j\omega C_L}\right) \end{pmatrix} \begin{pmatrix} I_1 \\ I_2 \end{pmatrix} \tag{2.6}$$

$$L = L_1 + L_\mathrm{i} \tag{2.7}$$

$$C = \frac{C_1 C_i}{C_1 + C_i} \tag{2.8}$$

The power supply resonance condition is

$$L + \frac{1}{\omega^2 C_L} - \frac{1}{\omega^2 C} = 0 \quad (2.9)$$

When this resonance condition is satisfied, the current flowing in the coil is maximized and the plasma can be generated efficiently. After the excitation of plasma, the impedance of the plasma also changes. It is therefore recommended to impedance matching before and after plasma ignition.

2.3.2 Device assembly

The plasma assembly is composed of a power supply and plasma load. A schematic diagram of the device is shown in Figure 2.8(a) while an actual image is shown in Figure 2.8(b). In general, the plasma load can be considered to be a combination of inductance L and capacitance C. A constant 100 pF capacitor is used at the end of the helical coil to form an LC resonant circuit resulting to maximum current flow when

$$\omega L = 1/\omega C. \quad (2.9)$$

Ignition of the plasma is not possible without the capacitor.

The inductor used is composed of helical copper coil (2-mm diameter thickness), wound around a 5.7 cm long quartz glass tube (5 mm inner diameter, 7mm outer diameter), and one end of the coil is connected to a capacitor and the other end is connected to the power supply through a 1.0 m coaxial cable wire. A tubing connection from a gas cylinder creates an Ar gas flow inside the quartz tube regulated by a flow meter from 1 to 5 L/min. An aluminum enclosure was used to keep all the elements intact and also has the purpose as a faraday shield. A hole in the aluminum shield served as an entry for air cooling. However, it was observed later that it was not necessary.

The 13.56 MHz RF power supply (RF Generator T847B, Creative Design Corp., Kawasaki, Japan) has a built-in matching network which consists of variable capacitors and an inductor connected in series shown in Figure 2.7. The power supply uses a 1 m

coaxial cable wire to connect to the plasma load. Specifically, an n-type connector is used to connect the coaxial cable wire to the inductor. The system does not include a water cooling system since it only operates at low power (<100 W).

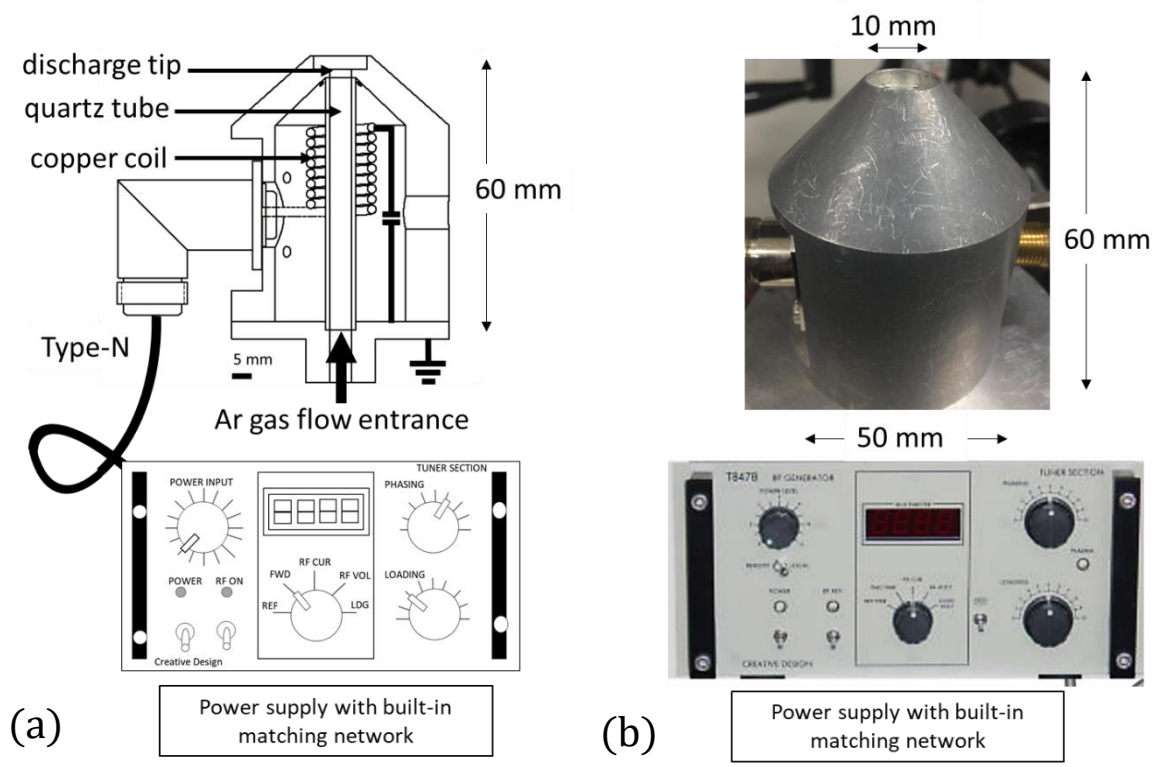

Figure 2.8 (a) Schematic diagram and (b) actual image of the atmospheric pressure ICP consisting of a 13.56 MHz RF power supply with a built-in matching network and plasma load enclosed inside an aluminum faraday shield. The plasma load consists of a copper coil inductor wound around a quartz glass tube connected to a 100 pF capacitor.

2.3.3 Successful ignition

Successful ignition of the low power atmospheric pressure plasma by inductive coupling was done using an ignition power of 37 W using 3 L/min Ar gas. Even though the ignition required 37 W RF power, the plasma is sustained at lower power such as

35 W and 30 W using 3 L/min. Increasing the gas flow rate, however, requires higher power to sustain the plasma.

Images of the plasma plume for varying power is shown in Figure 2.9. The plume length increased with the addition of power input. The symmetry of the plume also improved with increased power. The plume is denser near the tube due to the higher electric field in this area as E_θ increases with r. However, the afterglow would converge at the center of the tube forming a cone-shaped plume.

Figure 2.9 Plume images of the plasma excitation by inductive coupling using 3 L/min Ar gas for varied RF power.

Images of the plasma plume for varying gas flowrate is shown in Figure 2.10. The plume increased in length with increased gas flowrate. At a very low flow rate of 1 L/min, the plasma plume is very faint.

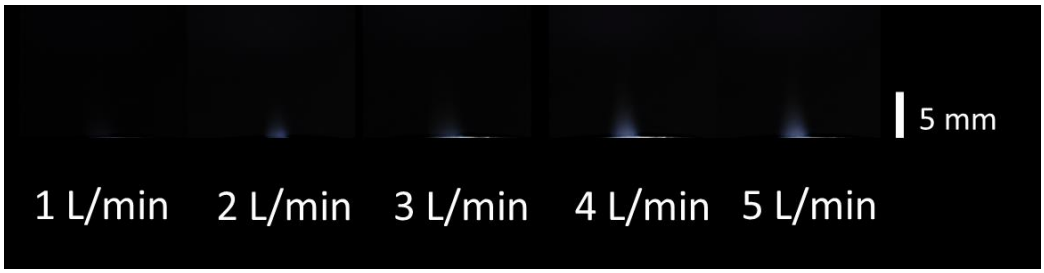

Figure 2.10 Plume images of the plasma excitation by inductive coupling 40 W for varied gas flow rates.

The ignition characteristics of the plasma are shown in Figure 2.11 for varied Ar gas flow. The gas flowrate characteristics include the ignition power, sustaining power and the reflected power measurements. The sustaining power is the power before the plasma is extinguished. The ignition power is almost the same using 1-4 L/min Ar gas flow rate. Higher ignition and sustaining power are required for a higher gas flow rate which is 5 L/min Ar gas. There is no significant effect on the reflected power measurements for varied gas flow.

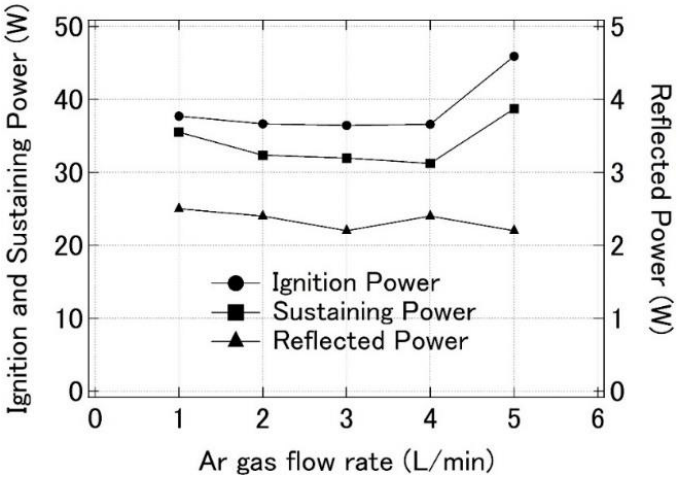

Figure 2.11 Ignition characteristics of the low power atmospheric pressure plasma for varied Ar gas flow.

2.3.4 Effects of capacitance loading

Impedance matching ensures maximum power delivery to the plasma load. The loading of the C_L and phasing of the C_P are varied and these variations affect the reflected power was observed. Figure 2.12 shows the decrease in the reflected power by variation of the loading of the C_L in the impedance matching network. A parabolic trend is observed where minimum reflected power is observed within the middle range 50-70% of the total loading of C_L. The same trend is observed for varied input power.

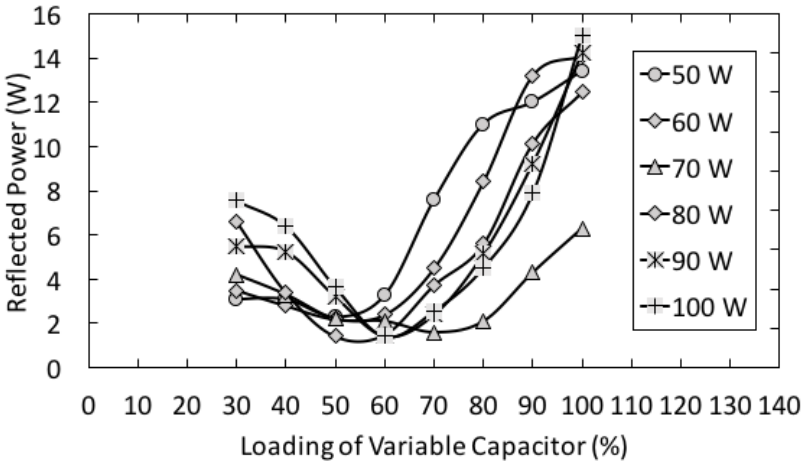

Figure 2.12 The decrease in the reflected power by variation of the loading of the CL.

2.3.5 Effects of coil size

Different coil configurations were used to minimize the impedance and optimize the power absorption of the plasma load. Increasing the wire diameters of the copper coil from 0.7-3 mm varied the inductance of the coil used. Figure 2.13 shows the effects of changing the copper wire diameter to the ignition and sustaining power. Minimum ignition and sustaining power are attained using a coil diameter of 3 mm. Sustaining a plasma discharge depends on a simple equilibrium between local energy dissipation through ohmic heating of the plasma, and energy loss from the discharge.

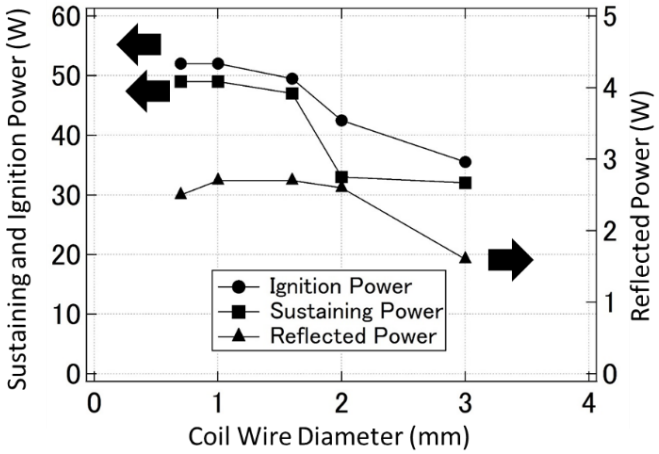

Figure 2.13 Ignition characteristics of ICP as the copper coil wire diameter is varied.

2.3.6 Effects of stray inductance

A double layer capacitor is designed to improve the ignition characteristics of the plasma. The simple LC series circuit is composed of an inductor which ignites and sustains the plasma and a capacitor designed to obey the series resonance circuit with the inductor. The resonant frequency is the frequency at which the total impedance of a series RLC circuit becomes purely "real", that is no imaginary impedances exist. A copper coil inductor and a double layer capacitor were fabricated and designed to attain the resonant frequency. At this point, a bigger aluminum Faraday shield enveloped the system to accommodate the capacitor assembly. Figure 2.14 shows the improved ICP with a built-in capacitor and a bigger cylindrical Faraday shield.

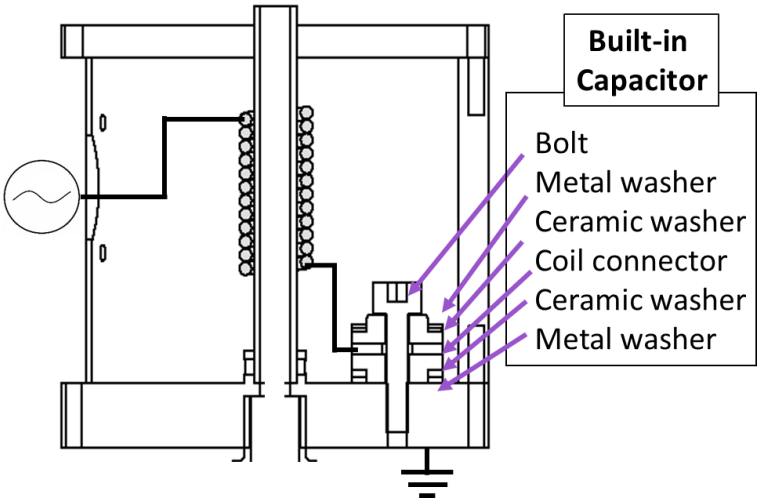

Figure 2.14 Schematic diagram of the improved ICP with a built-in capacitor.

The effects of the built-in capacitor and commercial capacitor to the ignition characteristics are presented in Figure 2.15(a)-(c). The ignition power, sustaining power and reflected power measurements are compared when using the commercial capacitor and the built-in capacitor, and also varying the argon flow rate. The ignition power measurements are shown in Figure 2.15(a), the sustaining power measurements are shown in Figure 2.15(b) and the reflected power measurements are shown in Figure 2.15(c). The ignition power, sustaining power, and reflected power are consistently lower in values when using the built-in capacitor compared when using the commercial capacitor. This is due to a more sturdy connection between the inductor and the capacitor. The connection between the inductor and the capacitor improves using the built-in capacitor which decreased the impedance of the circuit. The commercial capacitor's wire is looped around the end of the inductor which results in parasitic inductance. Parasitic components are unwanted characteristics in high-frequency circuits which limits the performance of the device. The impedance of the

circuit decreased without the stray inductance. This leads to consistent reflected power measurements shown in Figure 2.15(d).

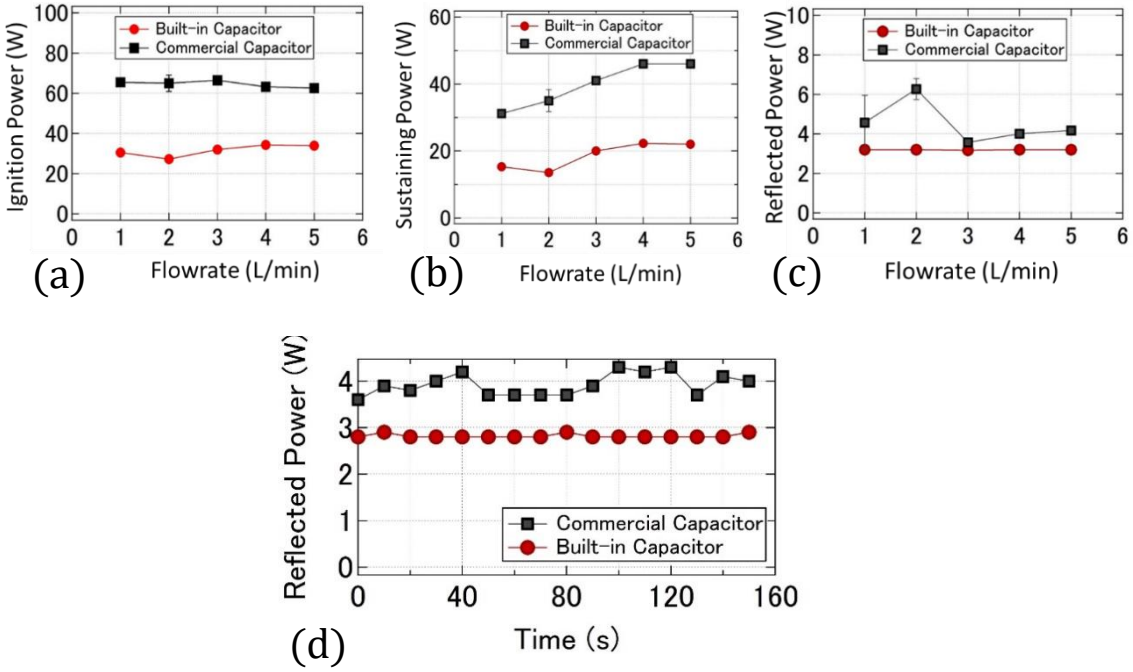

Figure 2.15 The ignition characteristics for various capacitor used. The (a) ignition power, (b) sustaining power, (c) and reflected power measured using varied flowrates and (d) varied time.

2.3.7 Effects of coil distance

The distance of the coil from the grounded base of the plasma tube container was changed as shown in Figure 2.16. The ignition characteristics of the plasma were studied for 1 to 7 mm distance of coil to the grounded base and the number of coil turns was changed from 6 to 12 turns.

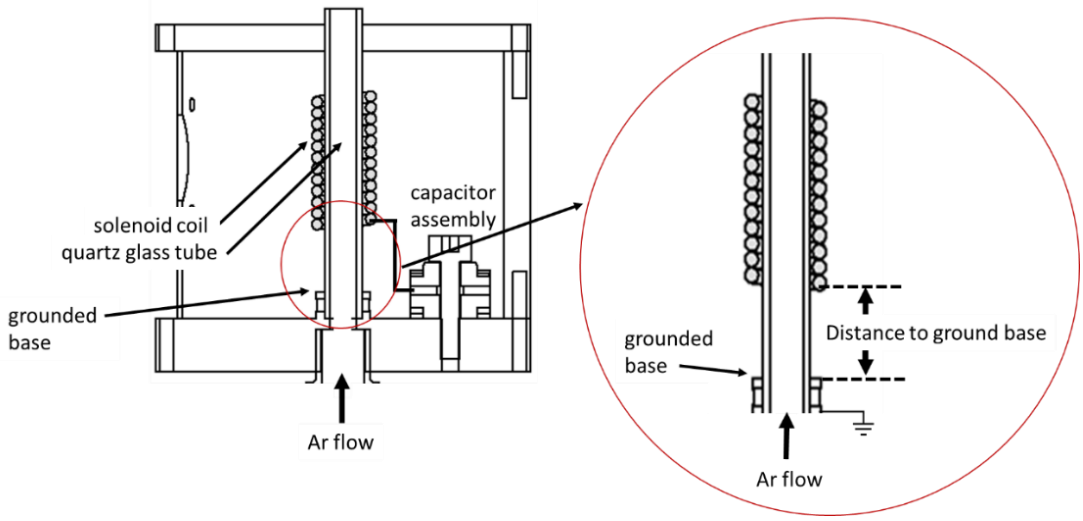

Figure 2.16 Schematic diagram of the experimental set-up for changing the distance of the coil from the grounded base.

Figure 2.17(a)-(c) shows the ignition characteristics of the plasma when the coil position is changed with respect to the aluminum grounded base. Enlarging the distance of the coil and the base significantly increases the ignition power and sustaining power. The ignition seems facilitated by the E-mode discharge due to the difference in the electric potential of the coil to the grounded base. This is further confirmed by the increase in reflected power when moving the coil position away from the grounded base. Increasing the number of coil turns from 6 to 12 significantly lowered the ignition and sustaining power. The minimum reflected power of 1.6 W is attained using the 12 coil turns.

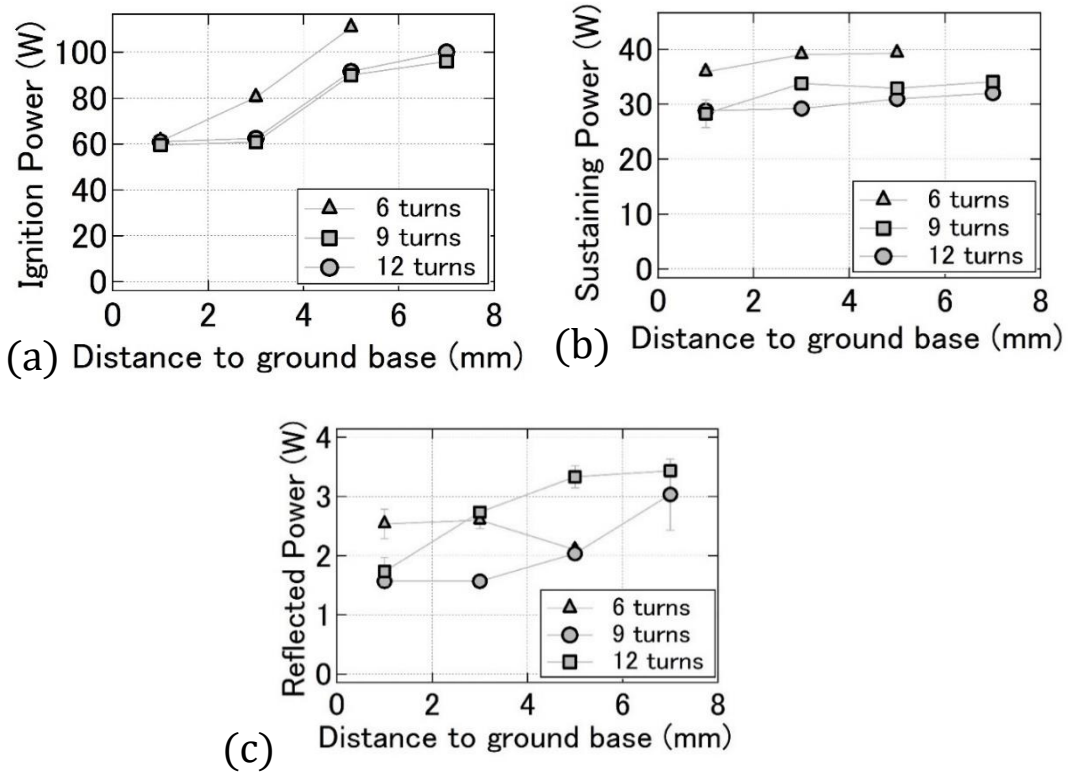

Figure 2.17 (a) Ignition power and (b) sustaining power and (c) reflected power measured when the coil position to the ground base is changed.

2.4 Summary

A 13.56 MHz atmospheric pressure ICP was developed which is a small, portable, and easy to ignite using low power (<100 W) and low Ar gas input (1-5 L/min). Sustaining a plasma discharge depends on parameters of the components in the impedance matching network and plasma load. The impedance of the circuit decreased with 50-80% capacitance loading, 2-3 mm coil wire diameter, and minimized stray inductance. E-discharge facilitates the ignition of plasma. A better coupling was observed with more number of turns up to twelve. However, the improvements from increasing the turns from six to twelve were not substantial.

Chapter 3
Modes of Operational Mechanism

3.1 Introduction

The two modes of operational mechanism in atmospheric pressure plasma are defined: the homogenous glow and filamentary discharge. The homogenous glow is driven by transient changes in the potential difference between the two electrodes over time while the filamentary discharge is caused by high static potential differences. In most cases, both modes of discharge exist in inductively coupled plasma. However, different operation conditions allow a clear distinction of the individual contributions. In this chapter, the characterization of the different modes of operation was done for the low power atmospheric pressure plasma produced by inductive coupling.

This chapter describes the qualitative and quantitative characteristics of ambient plasma-based desorption/ionization sources. For the qualitative characteristics, the study is focused on the unstable filamentation of the ion source. Using an optical emission spectrometer wavelength spectra were observed to identify the differences in the filamentary discharge and homogeneous glow.

For the quantitative characteristics, ion density measurements using the ion mobility spectrometer were done.

3.2 Plasma filamentation

The homogenous glow driven by equally distributed RF power is more stable and favorable as an atmospheric pressure ion source. Meanwhile, the filamentary discharge resembles arcing caused by potential differences and unstable plasma production. The transient versus steady-state characteristics of the individual discharge suggests the driving force for the current flow be inductive and capacitive, respectively. In most cases, both discharges exist in an RF excited plasma. However, different operation conditions allow a clear distinction of the individual coupling contributions. In this chapter, the characterization of the different modes of operation was done for the low power atmospheric pressure plasma produced by inductive coupling [6].

3.2.1 Homogenous glow mode of operation

The dominant mode of operation of the low power atmospheric pressure plasma is filamentary discharges. The homogenous glow is only observed when using RF power greater than 70 W and minimizing the reflected power from 5 W to 1.6 W. Figure 3.1 shows the transition from filamentary discharge to homogenous glow when minimizing the reflected power. The top view shows the brighter and denser light for the individual filament. The number of filaments increased by minimizing the reflected power. The donut-shaped inductively coupled plasma formed by the passage of electrical current induced by the transient magnetic field becomes more apparent with the increasing RF power coupling efficiency for the homogenous glow mode. Another feature of the homogenous glow is its longer plume length.

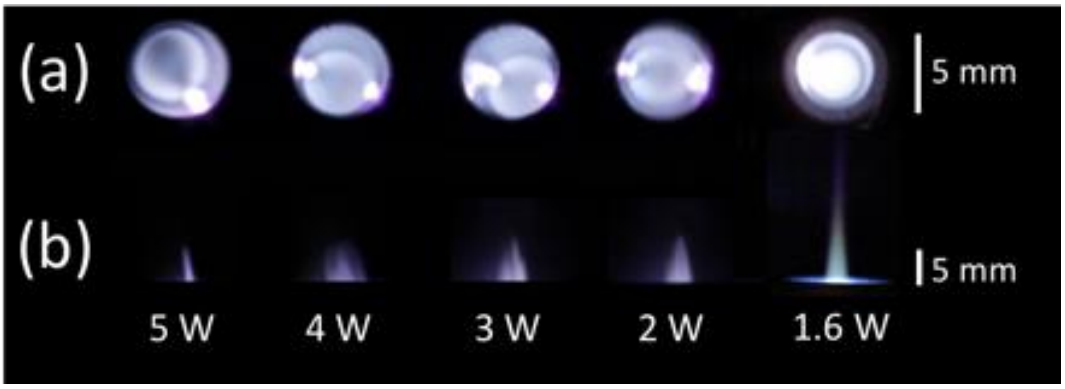

Figure 3.1 Transition from filamentary discharge to glow discharge at (a) top view and (b) side view. The reflected power is shown in the figure while the input power is kept at 70 W.

Once the homogenous glow is achieved at 70 W, the same mode is observed when gradually decreasing the power until it reaches 50 W and the plasma is extinguished. Figure 3.2 shows the images of the homogenous glow for varied RF power induced to excite the plasma. Decreased plume length is observed when reducing the input power from 70 W to 60 W. There is no significant difference in the plume length and plume intensity from 70 W to 100 W.

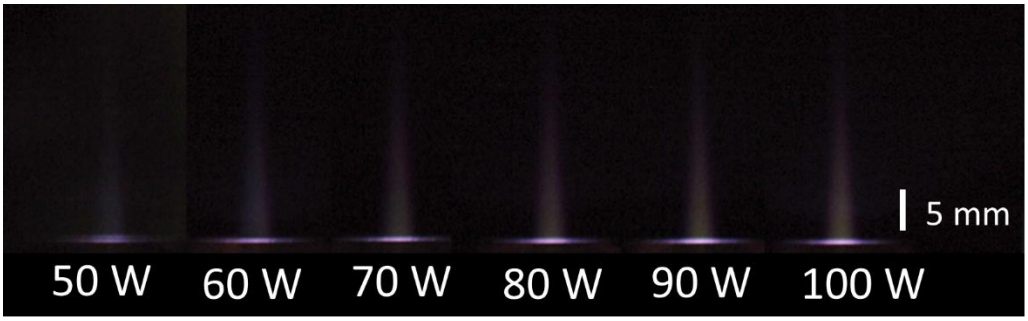

Figure 3.2 Homogenous glow plasma at varied RF power.

3.2.2 Optical emission spectroscopy

Optical emission spectroscopy (OES) is one of the fundamental plasma diagnostic methods which collects the intensity emitted by the excited atomic and molecular

species in the plasma. Plasma creates a unique emission spectrum specific to each element and these emission spectral lines yield information useful to identify the species composition of the plasma.

Figure 3.3 presents the schematic diagram of the optical diagnostic method and the emission spectrum of the filamentary and glow plasma. The OES used is HR 400 (350–1100 nm) in the filamentary discharge and the homogenous glow. The optical fiber of the OES was placed 50 cm from the discharged tube. The emission spectra of the filamentary and homogenous glow plasma were gathered.

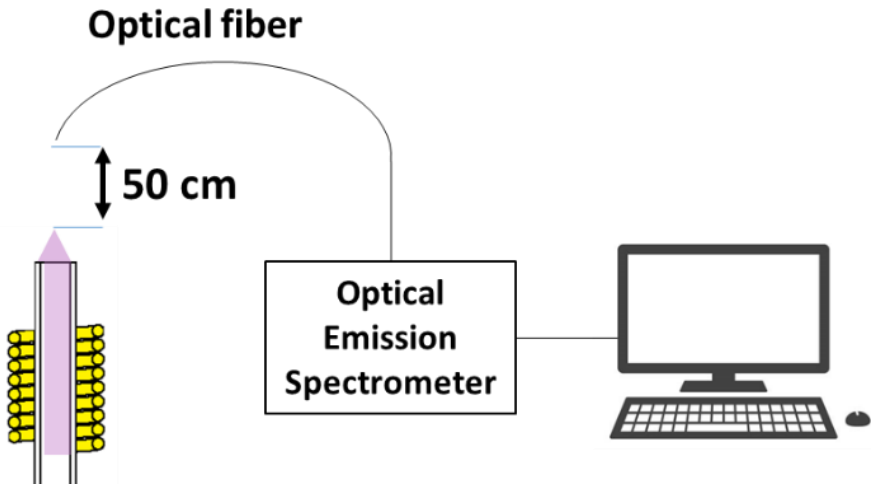

Figure 3.3 The experimental set-up in measuring the optical spectra of the plasma plume. The optical fiber is placed at 50 cm distance from the tip of the plasma discharge.

The emission spectrum shown in Figure 3.4 compares the line intensities that are present between glow and filamentary plasma. The line intensities of the filamentary discharge are greater than the homogenous glow in all the present species (O I, N I, Ar I). This is due to greater power absorbed by the filamentary plasma compared with the homogenous glow. Both modes of operation contain the same wavelengths of the line intensities.

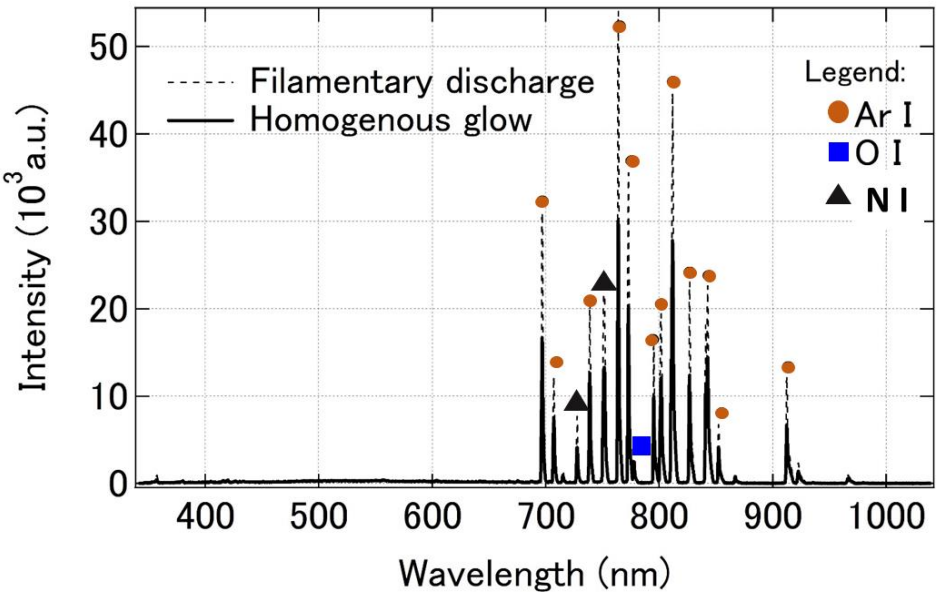

Figure 3.4 Emission spectrum of the two modes of operation in the low power atmospheric pressure produced by inductive coupling.

3.2.3 Ion mobility spectrometer

The Gerdien condenser, also known as the aspiration ion mobility spectrometer, is a simple structure instrument designed for ion-mobility analysis. It provides information on the ion mobility-ion density distribution of gaseous samples from a current. The Gerdien condenser schematic diagram is shown in Figure 3.5(a). The Gerdien condenser is composed of concentric electrodes that create the electrostatic field for collecting the ions from the plasma plume. The device is placed in front of the plasma plume as shown in Figure 3.5(b). A fan blower causes the diffusion of the ions from the plasma into the collector. Measurement of ion current from the plasma is done by applying a voltage to its collector.

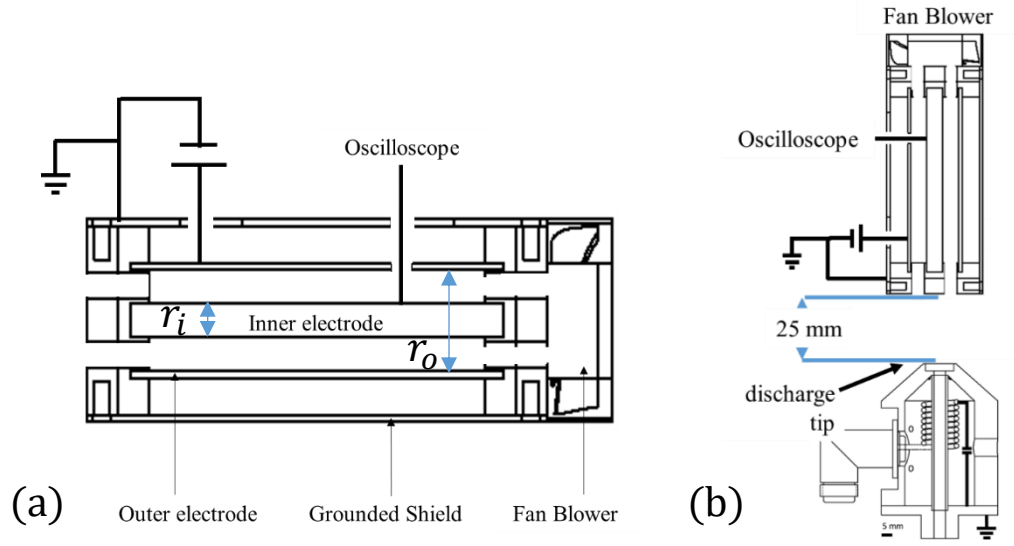

Figure 3.5 Schematic set-up of the ion mobility and ion density measurements using Gerdien condenser.

The typical *I-V* measurement using the Gerdien condenser is presented in Figure 3.6. The negative sweep and positive sweep of the voltage results in increased current magnitude. The negative current has greater value than the positive current. The saturation current I_s is proportional to the ion density n. The ion density is

$$n = \frac{I_s}{qV_fA} \tag{3.1}$$

where q is the charge constant, V_fA is the volumetric flow rate produced by a blower fan.

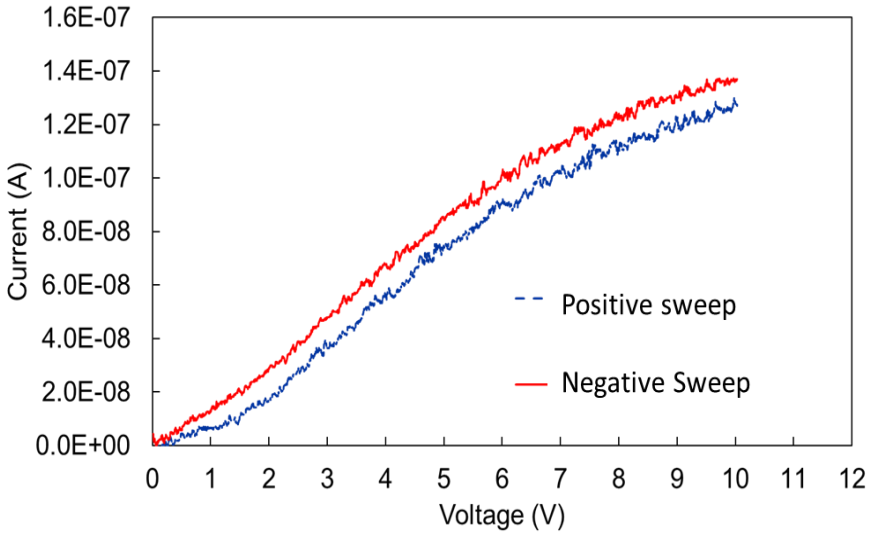

Figure 3.6 Typical IV measurements using the Gerdien condenser.

In this study, the Gerdien condenser is set-up at 50 cm from the discharge tip of the plasma. The total ion density measurements for varied RF power and Ar flow rates are shown in Figure 3.7. An increase in total ion density is observed with increasing forward power and the Ar flow rate. The total ion density of the homogenous glow is less than the filamentary discharge since the homogenous glow is faint-like and appears to be less dense. However, increasing the flow rate increased $A \cdot v_f$ the density of the homogenous glow higher that the filamentary discharge. A possible explanation for this apparently higher ion density may be due to an ion density local concentration held in a filamentary discharge.

At 4-5 L/min, the filament size was observed to decrease. At high flow rates, the effective momentum transfer collisions are not achieved resulting in a sudden decrease in size/number of filaments. At these values, it was observed that a stationary single filament develops instead of the usual multiple filaments.

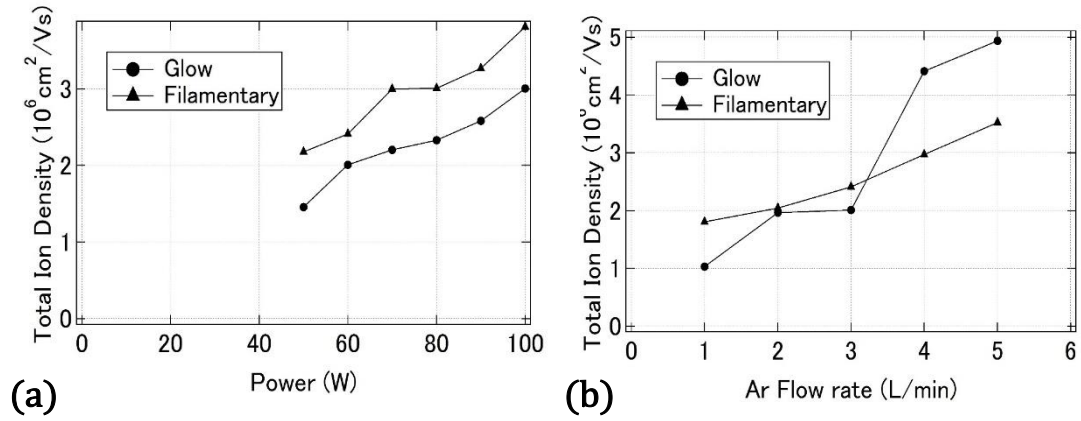

Figure 3.7. Total ion density measurements using Gerdien condenser.

The ion species k are identified with the corresponding calculated ion mobility. The ion mobility μ_k is calculated using

$$\mu_k = \frac{\ln\frac{r_0}{r_i}\left(\frac{dI}{dV}\right)}{2\pi q_k n_k l} \tag{3.2}$$

where r_0 is the outer electrode radius, r_i is the collector electrode radius (see Figure 3.4), q_k is the charge constant, n_k is the density of the ion species, dI/dV is determined from the slope of the *I-V* curve. Figure 3.8 shows the positive ion spectrum of the glow and filamentary plasma which corresponds to the *I-V* results when using 50 W and 3 L/min Ar. The filamentary spectrum contains a broader spectrum and it has ions with higher mobility values than in homogenous glow. Table 1 shows the possible ion species of the glow and filamentary plasma. The plasma contains argon, nitrogen, and oxygen ions. It is also observed that O^+ has a minimum density in a homogenous glow which is maximum density in a glow discharge.

Basically, the ion mobilities are higher for lighter atoms and molecules. Figure 3.6 indicates the glow mode creates larger mobility ions or disintegrates produced ions.

From the point of view of preserving large mass number molecules for the bio-medical applications, stable induction of filamentary discharge may be useful.

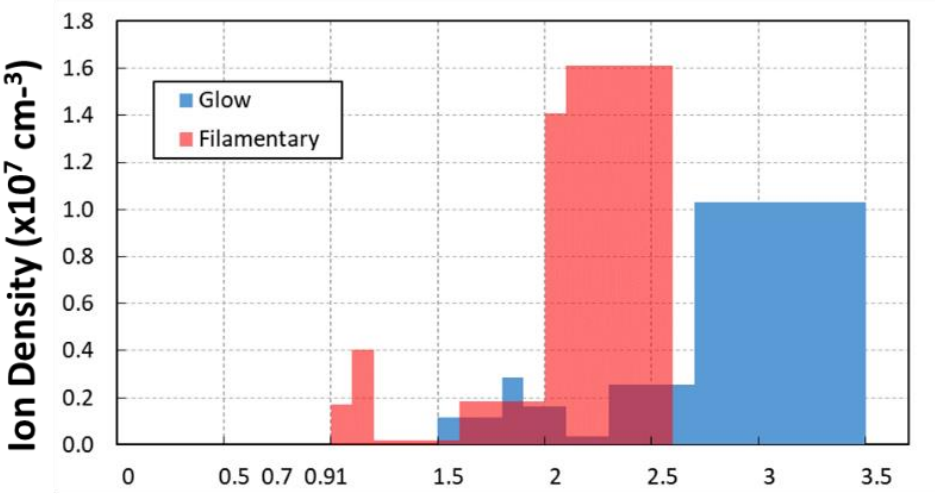

Figure 3.8 Positive ion spectrum of the filamentary discharge and homogenous glow plasma.

Table 1 Calculated ion mobility and the possible ion species of homogenous glow plasma and filamentary discharge.

mobility, μ_k, (cm^2/Vs)	Possible Ion Species
3.3	O^+ (*)
2.5	Ar^{++}
1.99	O_2^+, N_2^+
1.73	Ar^+
1.2	O_2^+
0.93	Ar^+

(*) present in glow plasma only

3.3 Summary

The homogeneity and stability of the atmospheric pressure plasma are crucial in chemical analysis for a plasma-based ambient desorption/ionization source. The Ar plasma produced by inductive coupling at atmospheric pressure often exhibited filamentary discharge which is very unstable. A stable homogenous glow plasma was only observed the discharge was started at 70 W, and then the reflection power was reduced.

Diagnostics of the filamentary and homogenous glow plasma reveals greater line intensity of the emission spectrum of the filamentary discharge compared with the homogenous glow plasma. The maximum intensity for both modes of operation is observed at 763.5 nm. Moreover, both modes of operation showed the same line intensity distributions.

Coupling the device to Gerdien condenser, also known as an aspiration ion mobility spectrometer, results in higher total ion density measurements in filamentary discharge compared to the homogenous glow plasma. The filamentary discharge also contains a broader ion spectrum with higher mobility values than in homogenous glow plasma. Identification of the present ions from the *I-V* measurements of the Gerdien condenser reveals the presence of argon, nitrogen, and oxygen ions. It is also observed that O^+ has a minimum density in an inhomogenous glow which is maximum density in filamentary discharge. The observed spectra for the two different modes particularly filamentary discharge shows the presence of large molecules of low mobilities.

Chapter 4
Magnetic Enhancements

4.1 Introduction

Recently, the external magnetic field is being employed to improve the stability and ion production efficiency of atmospheric plasma jet [11]. The use of an external magnetic field has been widely studied for low-pressure plasma where plasma can be controlled by a strong magnetic field [17,18]. Plasma is constricted by the strong magnetic field resulting in significant enhancements in the density, temperature and light intensity from the produced plasma. For atmospheric pressure plasma, only a few studies focused on the effects of the external magnetic field while the effect of applying a magnetic field to an atmospheric pressure plasma is not often obvious [19]. Due to the short mean free path, electron collisions with neutral particles are predominant which means that the cyclotron frequency is outnumbered. However, the use of external magnets was observed to increase chemically active oxygen species [20,21]. This was possibly caused by activated collision frequency of energetic electrons to oxygen gas molecules due to cyclotron and drift motions of electrons. There are also possibilities of enhancement of glow discharge of APP, such as improving its size and uniformity for efficient plasma generation (Jiang et. al, 2014).

4.2 Theory

The mean free path of atmospheric pressure plasma is very short compared to the typical Larmor radius of a charged particle. The mean free path is the average distance traveled by a particle for a collision to occur. For atmospheric pressure plasma, the mean free path is approximately

$$\lambda_e = \frac{1}{n_{neutral}\sigma} = 400\ nm \tag{4.1}$$

where the corresponding cross-section σ_c is

$$\sigma_c = \pi \left[\frac{Z_1 Z_2 e^2}{4\pi\varepsilon_0(3kT)}\right]^2 = 1.13 \times 10^{-16} cm^2 \tag{4.2}$$

For an atmospheric condition, the Lamor radius can be less than the mean free path, $r_L < 90\ nm$, to make the effect due to the magnetic field substantial. The Larmor radius is given by

$$r_L = \frac{mv}{eB} \tag{4.3}$$

Where m is the electron mass $(9.10938356 \times 10 - 31\ kg.)$, e is electron charge $(1.60217662 \times 10 - 19\ C)$, B is the magnetic field and v is approximately considered as the electron drift velocity $\mu_e E$, where E is the electric field and μ_e is the electron mobility which is for argon atmospheric pressure plasma is approximately

$$\mu_e = \frac{e}{mv_m} = \frac{1.76x10^{15} cm^2}{v_m[s^{-1}]\ V{\cdot}s} = 4.3 \times 10^2\ \frac{cm^2}{V{\cdot}s} \tag{4.4}$$

The electron temperature is a fundamental parameter for atmospheric pressure plasma. The mean free path is also highlighted where it shows the dependence on magnetic flux density greater than a critical value to show a significant effect on the plasma.

Integrating the mean free path into the equation, using equation (4.1) and (4.3), when the magnetic field is transverse to atmospheric pressure plasma, the minimum external magnetic field that affects the plasma is

$$B > \frac{m\mu_e E}{e\lambda_e}[T] \tag{4.5}$$

The electric field E is to be determined for the local RF field. Meanwhile, the very fact that we observed ionization of Ar let us assume electrons are accelerated up to the ionization energy of Ar (15.6eV). A rough estimation of the critical magnetic flux density can be obtained

$$B \cong \frac{m\mu_e E}{e\lambda_e}[T] = 33.5\ T \tag{4.6}$$

or for electrons of temperature T(k)

$$B \cong \frac{m\mu_e E}{e\lambda_e}[T] \sim 9.6 \times 10^{-12}\sqrt{T(k)}\ [T]. \tag{4.7}$$

For 300K electrons, it still needs 1.7 Tesla of 17 kG. Thus, there is no reason for expecting a resonance behavior but one expects the contribution from $\vec{j}\times\vec{B}$ force, where $\vec{j}$ is the current density of the plasma.

4.3 The orientation of the magnetic field

The orientation of the magnetic field could be transverse or parallel to the atmospheric pressure plasma discharge as shown in Figure 4.1. The transverse external magnetic field was utilized by [21] and [20] using the Helmholtz coil. The induced current density j: (j_x, j_y, j_z) due to the transverse magnetic force can be deduced from MHD ohm's law

$$j_y = \sigma_e\left(V_z B_x + E_y\right) \tag{4.8}$$

where E_y is the induced electrostatic field, and σ_e here is the electrical conductivity of the plasma.

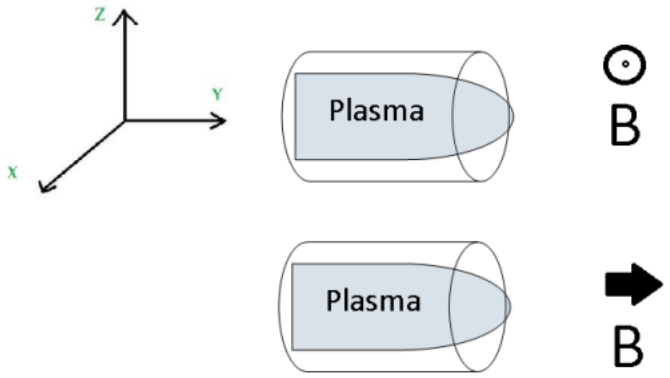

Figure 4.1 The orientation of the external magnetic field can be transverse or parallel to the plasma discharge.

This process leads to the transport of charged particles from the plasma zone and in turn, often shrinks the plasma number density [19]. This magnetic field orientation has disadvantages for surface treatments but has benefits for plasma reactors such as corona discharges for air pollutant removal. It was observed that the magnetic field induces cyclotron motion and associated drifts of the energetic electrons, making the residual time longer in the ozone-producing space, and the collision frequency of electrons to oxygen molecules also greatly increased" [20]. However, using permanent magnets such as $Nd_2Fe_{14}B$ magnets, the external magnetic field caused the current density in corona discharge to increase resulting in the stability in the discharge. It also improved the performance in plasma jet resulting in lower power consumption, enlarged plasma size, improved plasma uniformity, enhanced plasma chemical activity and low gas temperature [22].

In atmospheric plasma parallel to magnetic field, using Helmholtz coil, the induced current density due to the transverse magnetic force can be deduced from MHD ohm's law

$$j_\theta = \sigma_e(V_z B_r + E_\theta) \tag{4.9}$$

This process reduces plasma loss to the walls leading to enhanced plasma density and plasma jet irradiance [19]. Its applications include stabilization and acceleration of rotating gliding arc [23].

4.4 Experimental set-up

A solenoid magnet employed to enhance the ignition characteristics and increase ionization reaction efficiency in the ICP. The schematic diagram of the magnet-assisted ICP is shown in Figure 4.2(a) side by side to the magnetic flux density measurements at the axial centerline of the solenoid using Gaussmeter for different coil current shown in Figure 4.2(b). The RF plasma positions where varied according to the labeled position A, B, and C. Note that the copper coil used in this experiment is not directly grounded which makes the plasma purely capacitively coupled. The magnetic flux density is almost constant at position B, decreasing in position A, and increasing in position C. Namely, we have B_r components in these region.

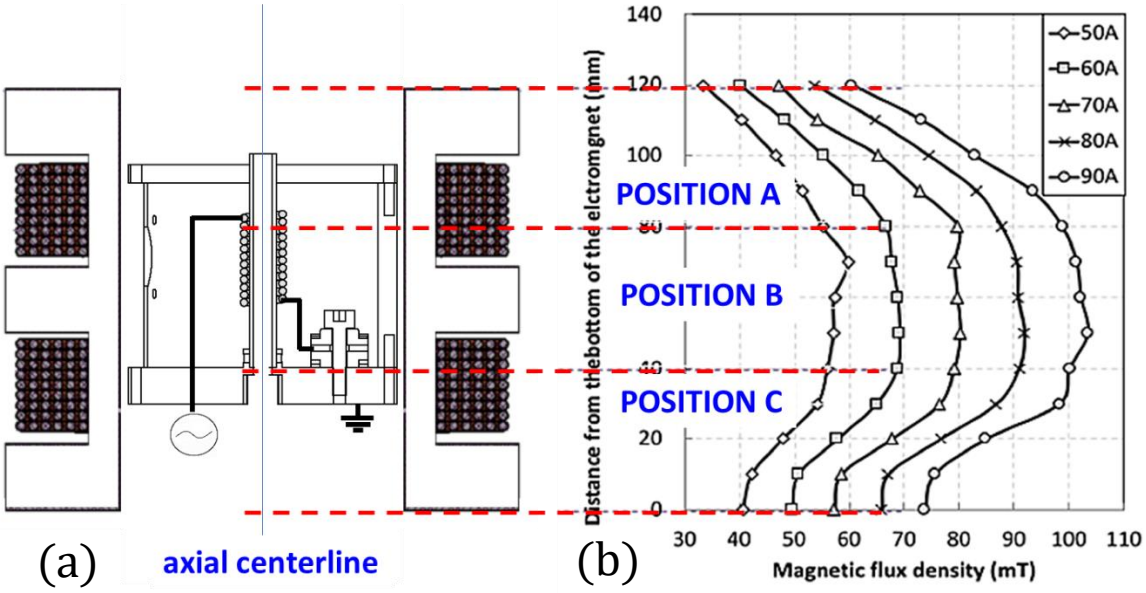

Figure 4.2 (a) Schematic diagram of the magnet-assisted atmospheric ICP and (b) magnetic flux density in varied coil current. The copper coil used is not grounded which makes the plasma purely capacitively coupled.

4.5 Qualitative evidence: plasma plume

4.5.1 Image analysis at position A

The lower base of the ICP is placed 80 mm from the lower base of the electromagnet. Several images of the plasma plume were captured with increasing coil current. The camera settings include a shutter speed of 1/40 s and aperture opening of F5.6. For the image analysis, *ImageJ* software has been utilized to obtain optical radiation intensity distribution and the plasma plume length was measured using the distance where optical intensity is greater than zero. Figure 4.3(a) and Figure 4.3(b) show the images of the plume captured at increasing coil current at positive and negative polarity respectively. The plume length measurements are shown in Figure 4.4 which indicates a significant increase when the magnet polarity is positive and

significant decrease when the magnet polarity is negative. The difference in effects in polarity may probably due to the decreasing magnetic flux density at this position.

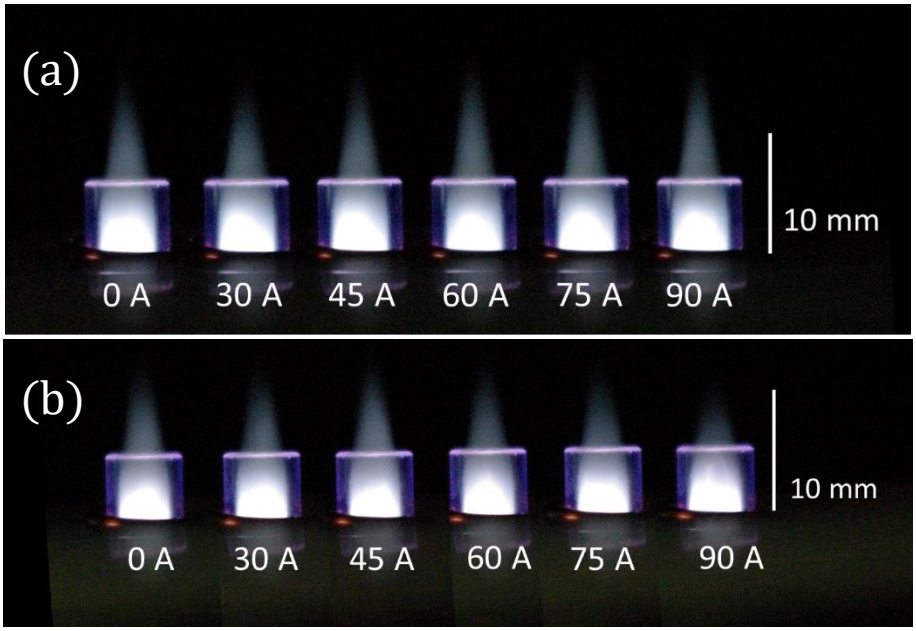

Figure 4.3 Plume images for (a) positive magnet polarity and (b) negative magnet polarity.

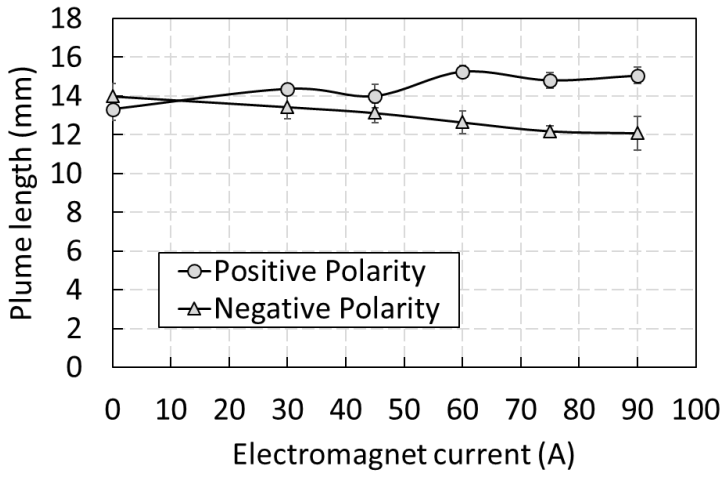

Figure 4.4 Plume length measurements with increasing electromagnet current.

4.6 Quantitative evidence: ignition

The ignition power and sustaining power were measured for increasing flow rates using 50 A and 90 A electromagnet current. The ICP is placed at position B [refer to Figure 4.2b]. Figure 4.5 (a) shows the ignition power measurements with the presence and absence of a magnetic field while Figure 4.5(b) shows the sustaining power measurements with and without the magnetic field. The ignition power decreased using 1-3 L/min Ar flowrate and electromagnet current of 50 A and 90 A. There are no effects in the sustaining power of ICP.

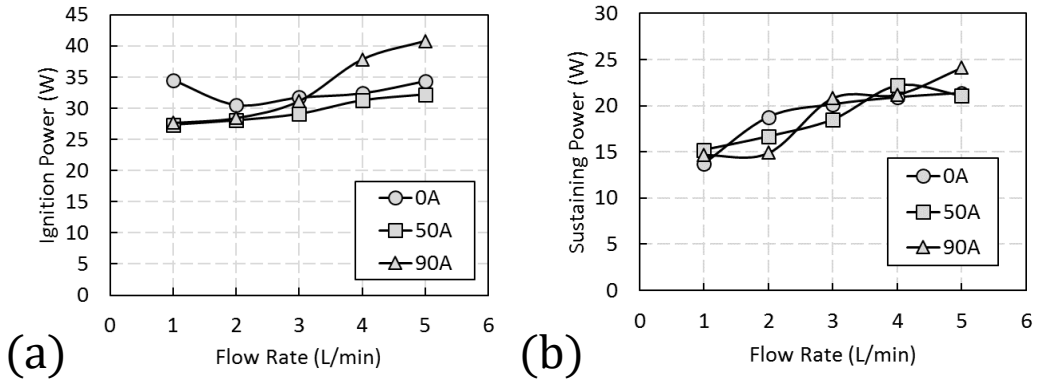

Figure 4.5 The effects of external magnets to the (a) ignition power and (b) sustaining power of the ICP.

The total ion density measurements using the Gerdien condenser are shown in Figure 4.6(b) when the location of the ICP is at position A as shown in Figure 4.6(a). The negative and positive ions are collected using 30 W forward power and 3 L/min Ar flow rate. An external magnet is applied using electromagnet current of 5-35 A. The effects of the magnetic field to the total ion density measurements are observed to be

more significant with the negative ions than the positive ions. However, the positive ion density still increased by >20 % using external magnet density >300 Gauss.

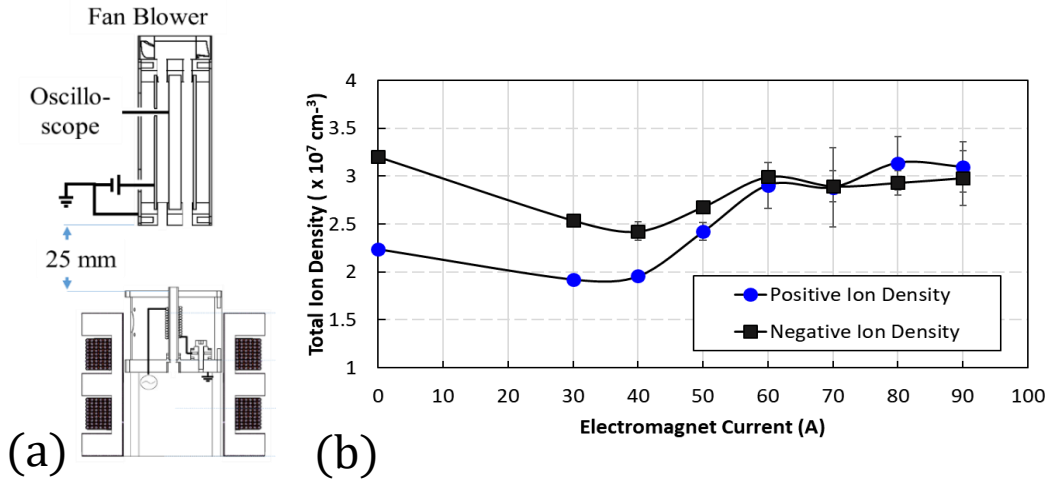

Figure 4.6 (a) Schematic diagram of the experimental set-up when using the Gerdien condenser and the ICP is placed at position A. (b) Total ion density measurements for this experimental set-up.

Moving the ICP at position B as shown in Figure 4.7(a), the total ion densities are measured as shown in Figure 4.7(b). At this point, the magnetic profile is constant. Both the positive and negative ion densities increase with an increased magnetic field. Increase magnetic field density, therefore, increased the ion densities. Also, The presence of the azimuthal electric field perpendicular to the magnetic field accelerates the electrons.

Figure 4.8(a) shows the experimental set-up when the ICP was moved to position C. The Gerdien condenser position at this point is larger at this configuration because the BNC connector of the Gerdien condenser is obstructing the decrease in the position of the Gerdien condenser. The ion density measurements are shown in Figure 4.8(b).

At this position, the positive ion density is greater compared to negative ion density. The convergent nature of the magnetic field caused an increase in positive ions.

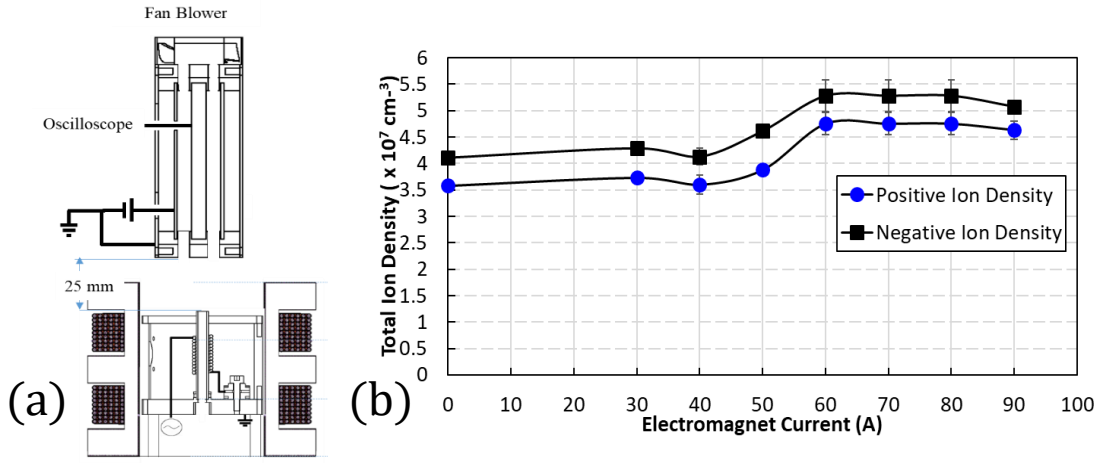

Figure 4.7 (a) Schematic diagram of the experimental set-up when using the Gerdien condenser and the ICP is placed at position B. (b) Total ion density measurements for this experimental set-up.

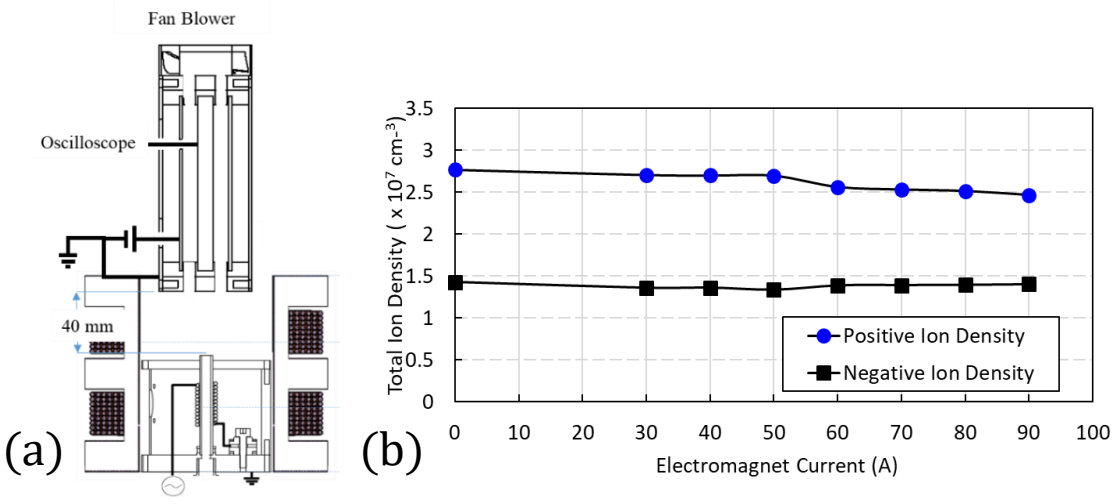

Figure 4.8 (a) Schematic diagram of the experimental set-up when using the Gerdien condenser and the ICP is placed at position C. (b) Total ion density measurements for this experimental set-up.

The ion spectrum for varied magnetic flux intensity is shown in Figure 4.9(a)-(h). The ion spectrum contains the ion density with respect to the ion mobility values. The right y-axis corresponds to the total ion density of the positive ions. The average ion mobility range is 0.5-2.5 cm^2/Vs for the positive ions and 0.5-1.5 cm^2/Vs for the negative ions. The density of the positive and negative ion increased with an increase in the applied magnetic field although the ion density distribution appears to be similar from Figure 4.9(a)-(f). The positive ion distribution drastically changes using 350 Gauss and 400 Gauss as shown in Figure 4.9(g) and Figure 4.9(h). The positive ion density peaks shift to higher mobility values while the negative ion density distribution remains the same. At the higher magnetic field intensity, the $\vec{j}\times\vec{B}$ force should increase and since $\vec{j}$ changes the sign while $\vec{B}$ directs the same, we have a hald cycle plasma shift to a wall and the other to the center. During the better plasma confinement period, disintegration of the larger molecules in the plasma is enhanced. The speculation requires further study by enlarging the intensity of the magnetic field.

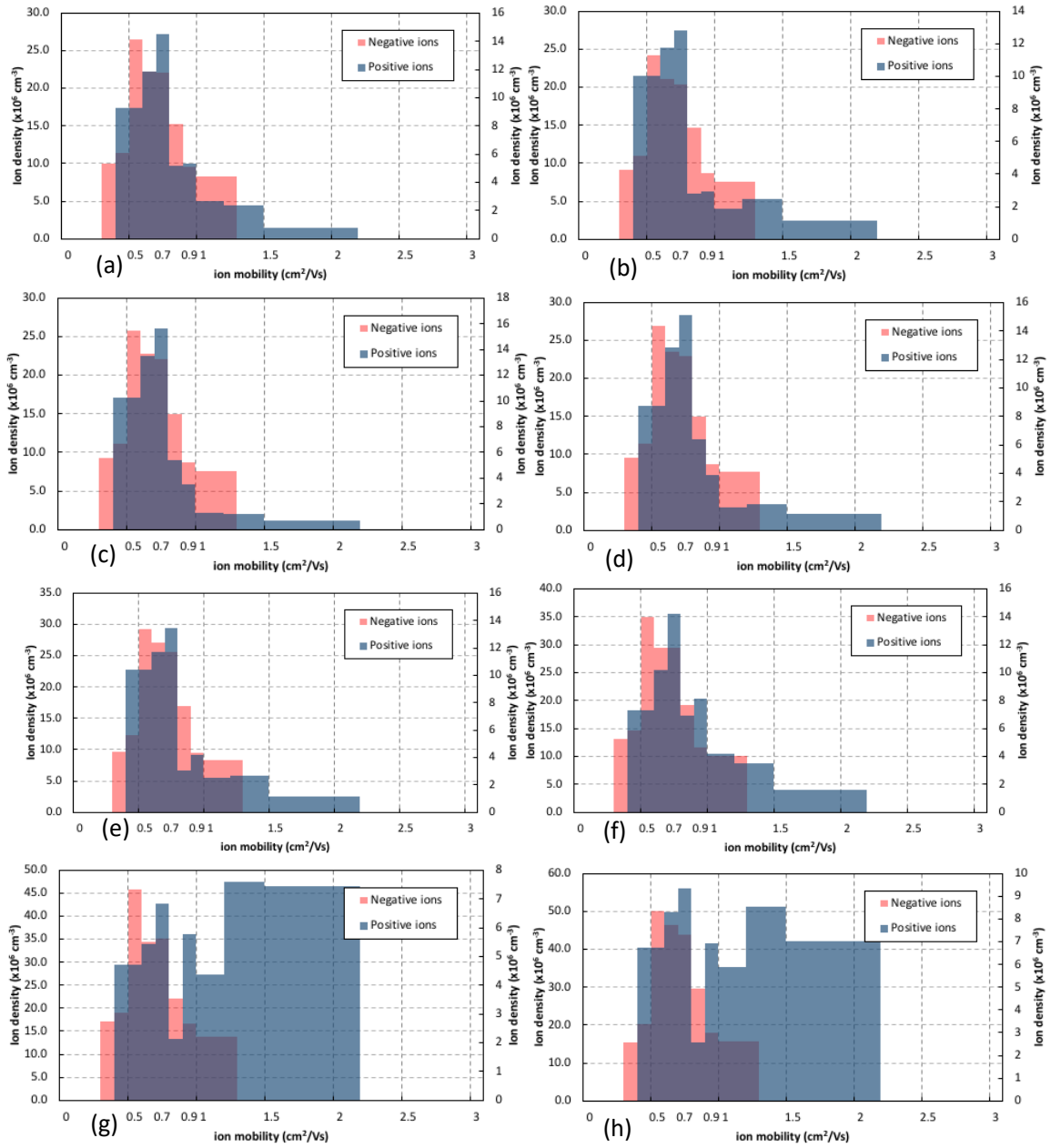

Figure 4.9 The ion spectrum of the Ar plasma using (a) no external magnetic field, and with external magnetic field with intensity of (b) 60 Gauss, (c) 110 Gauss, (d) 170 Gauss, (e) 230 Gauss, (f) 290 Gauss, (g) 350 Gauss, and (h) 400 Gauss.

4.7 Using permanent magnets

A permanent magnet was coupled to an RF atmospheric pressure source to see if it is possible to make a compact system. A Nd2Fe14B ring magnet was placed in the discharge opening of the plasma device as shown in Figure 4.10. The magnetic field measured from the nozzle tip is shown in Figure 4.11. Several images of the plume were taken for image analysis using the ImageJ software.

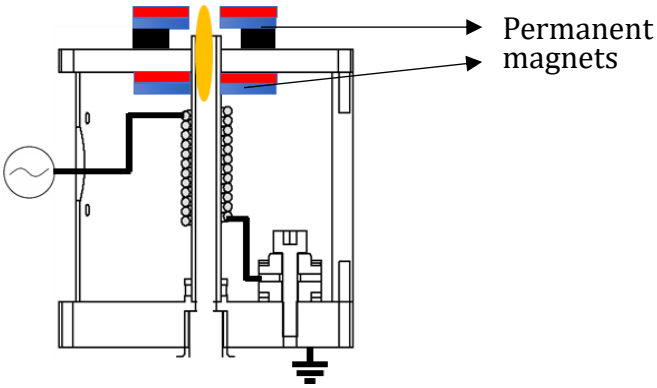

Figure 4.10 The position of external magnets in the ICP.

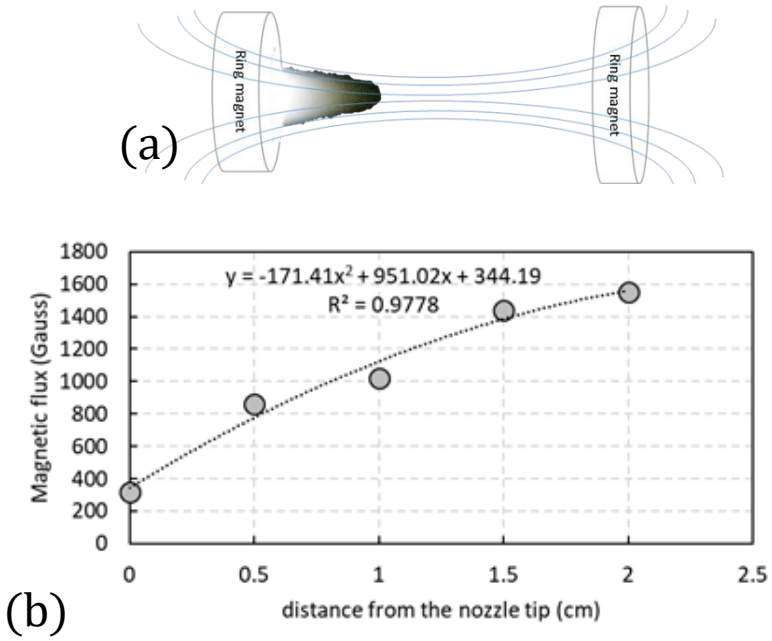

Figure 4.11 Magnetic field strength measurements from the tip of the nozzle.

Several images of the plasma plume were captured with and without the magnetic field. The camera settings include a shutter speed of 1/40 s and aperture opening of F5.6. For the image analysis, *ImageJ* software has been utilized to obtain optical radiation intensity distribution in the transverse and axial direction. The plasma plume length was measured using the maximum distance where optical intensity is greater than zero. The relative intensity is the measure of the gray area by ImageJ versus the plume length which is the axial centerline distance from the nozzle tip.

Shown in Figure 4.12(a) and Figure 4.12(b) are the plume length and intensity measurements of the inductively coupled plasma with and without the external magnetic field. There are no significant changes in the plume length and intensity of plasma when the external magnetic field is introduced. The increase in plume length and intensity is considered associated with improved ionization of argon molecules indicating enhanced plasma chemical activity. At a higher plasma excitation power, there is enough energy to cause ionization and further addition of the magnetic field may have little effect on the plume length and intensity of plasma. The present result seems to indicate the field effects do not improve the system efficiency. However, due to the shape and size of the magnet, only one field geometry configuration was examined. A more careful field geometry calculation is required to realize the efficiency improvement that was observed using an electromagnet system.

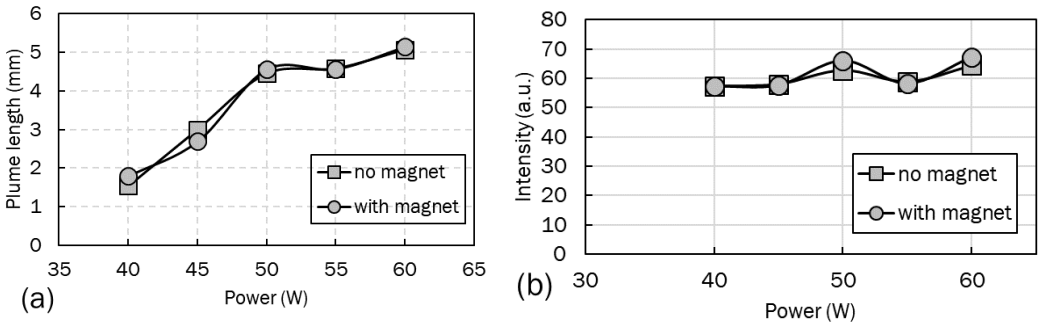

Figure 4.12 (a) Plume length measurements and (b) intensity measurements of the Ar plasma with and without external permanent magnets

4.8 Summary

The minimum magnetic flux density to cause significant effects in the plasma depends on the local electric field applied according to the generated equation when comparing the Larmor radius and mean free path. Results show significant effects of increased magnetic flux to Ar plasma plume where the plume length increased with positive magnet polarity and it decreased with negative polarity. The increased magnetic flux also affects the total ion density measurements. The ion density of nitrogen (N_2^+, O_2^+) drastically increased to 400 Gauss. Although the magnetic flux has significant effects on the ignition characteristics, plasma plume, and ion density, the intensity of the magnetic flux for the electromagnet and that for the permanent magnet is not sufficient to stabilize the atmospheric pressure plasma.

Chapter 5
Wire Stabilized Atmospheric Pressure Plasma

5.1 Floating wire

A critical requirement in chemical analysis for a plasma-based ambient desorption/ionization source is its stability. The stability of the plasma source can be defined by the spatial profile and the temporal change of the plasma characteristics. It was observed from the previous chapter that the atmospheric pressure plasma is very unstable especially when the mode of operation is filamentary discharge. This chapter discussed the stabilization process in atmospheric pressure plasma produced by inserting an ignition wire in the plasma.

The use of floating wire to enhance the ignition characteristics of inductively coupled plasma was investigated by Sato et al., 2013 [24]. The floating wire placed inside successfully enhanced the ignition of the inductively coupled microplasma source used as a vacuum ultraviolet (VUV) light source. The microplasma source consisted of a quartz capillary tube (OD: Ø1.5 mm, ID: Ø1 mm) surrounded by a coil antenna. The same technique is used to enhance the ignition characteristic of the Ar atmospheric pressure plasma produced by inductive coupling. This study further investigates the stabilization process of the atmospheric pressure plasma caused by the wire. Moreover, instead of an electrically floating wire, the wire used is connected to the ground electrode.

5.2 Experimental set-up

The plasma assembly is shown in Figure 5.1. The 13.56 MHz RF power supply connected to the series of inductors and capacitor assembly. The plasma production structure is composed of helical copper coil (2-mm diameter thickness), wound around a 5.7 cm long quartz glass tube (5 mm inner diameter, 7mm outer diameter), and one end of the coil is connected to a capacitor assembly and the other end is connected to the power supply through a 1.0 m long coaxial cable wire. A tubing connection from a gas cylinder creates an Ar gas flow inside the quartz tube regulated by a flow meter from 1 to 5 L/min. An ignition wire assembly is placed at the center of the discharge tube.

The ignition wire assembly is composed of 90 mm long tungsten wire (0.7 mm diameter) placed inside two concentric ceramic tubes to keep the wire in the center position of the quartz tube. The ignition wire was originally placed as floating wire but later attached to the ground terminal since it was found out that this electrical circuit configuration makes the evaluation of ion saturation current possible.

The capacitor assembly is composed of two ceramic spacers (15 mm OD, 2 mm thickness) and the ring wire connector to the inductor placed in between the spacers. These two ceramic spacers are fixed between two metal rings held at the ground electrical potential. A 2 mm diameter screw fixes the capacitor assembly in place.

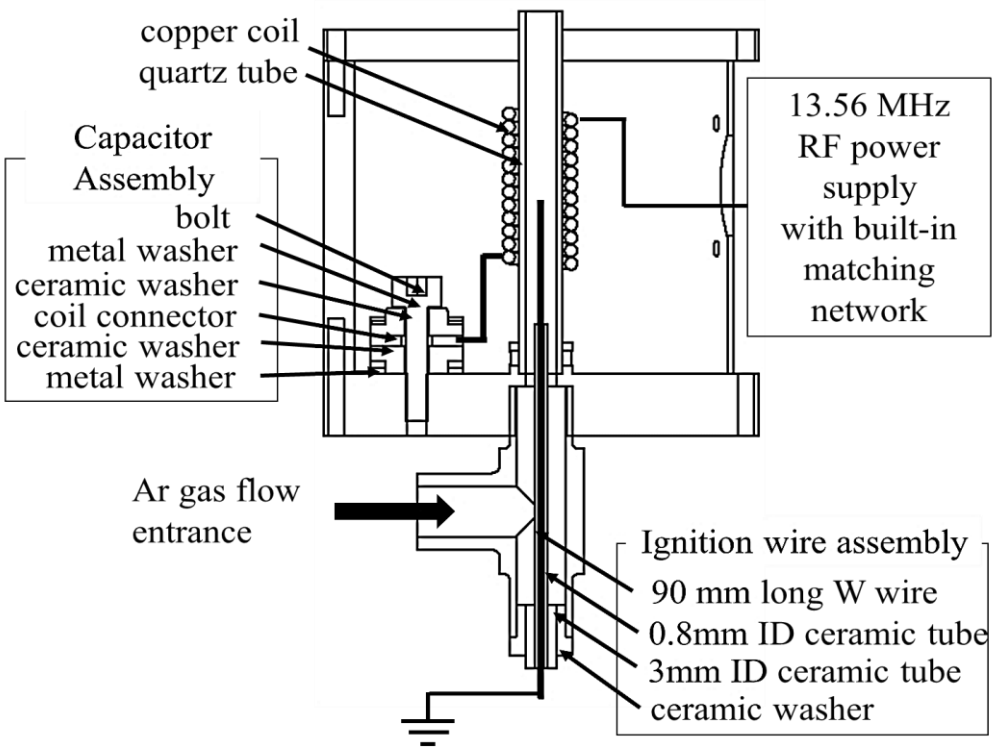

Figure 5.1 The wire stabilized atmospheric pressure plasma assembly.

5.3 Enhanced ignition

Figure 5.2 shows the schematic diagram of the axial position of the wire tip with respect to the midsection of the copper solenoid coil. The changes in ignition characteristics of the plasma were observed when the wire tip position was changed. A position adjuster that mechanically drives the entire ignition wire assembly tunes the position of the ignition wire end.

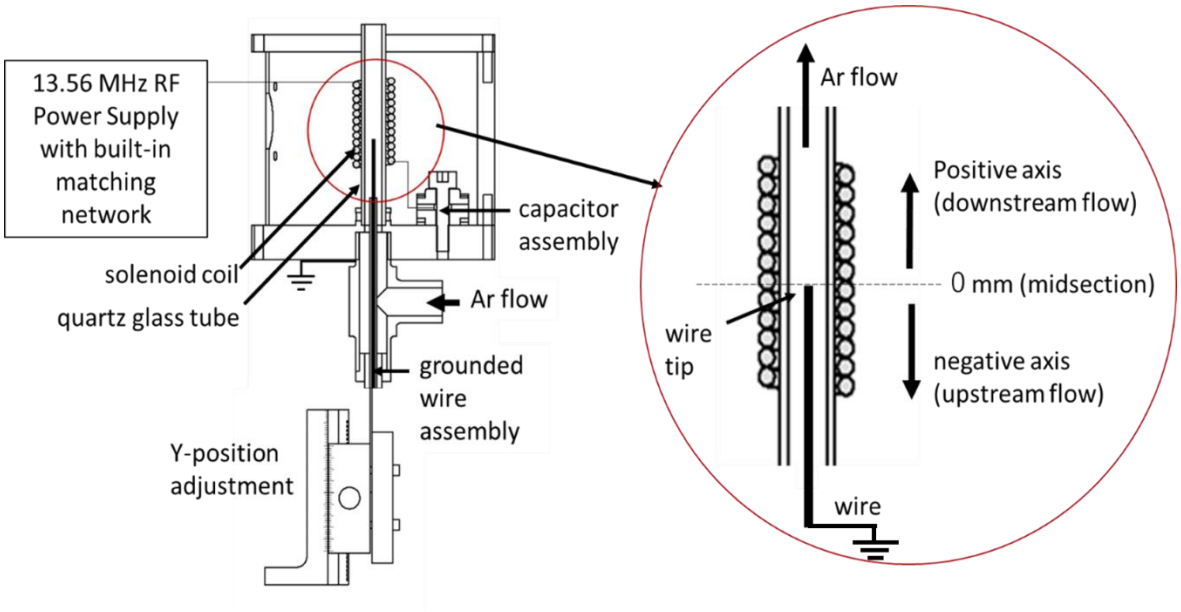

Figure 5.2 Schematic of the experimental set-up in variation of ignition wire position.

Figure 5.3(a) shows the ignition characteristics of Ar plasma when the axial position of the tungsten wire is varied. The ignition power of Ar plasma is observed to decrease when the wire tip position is moved towards the flow downstream. The ignition power also significantly lowered by increasing the number of coil turns as observed previously without the wire. Ignition occurs due to the difference in electric potential from the wire tip located near the coil across the glass tube wall to the grounded terminal called the ground base in Chapter 2. Large electric potential difference can be formed by inductive coupling to the tungsten wire.

The sustaining power is shown in Figure 5.3(b) and has a similar trend with the ignition power. The reflected power also significantly decreases with the addition in the number of coil turns. The optimum ion source setting is obtained by setting the number of coil turns to 12 and the ignition wire tip axial position located at the midsection of the coil.

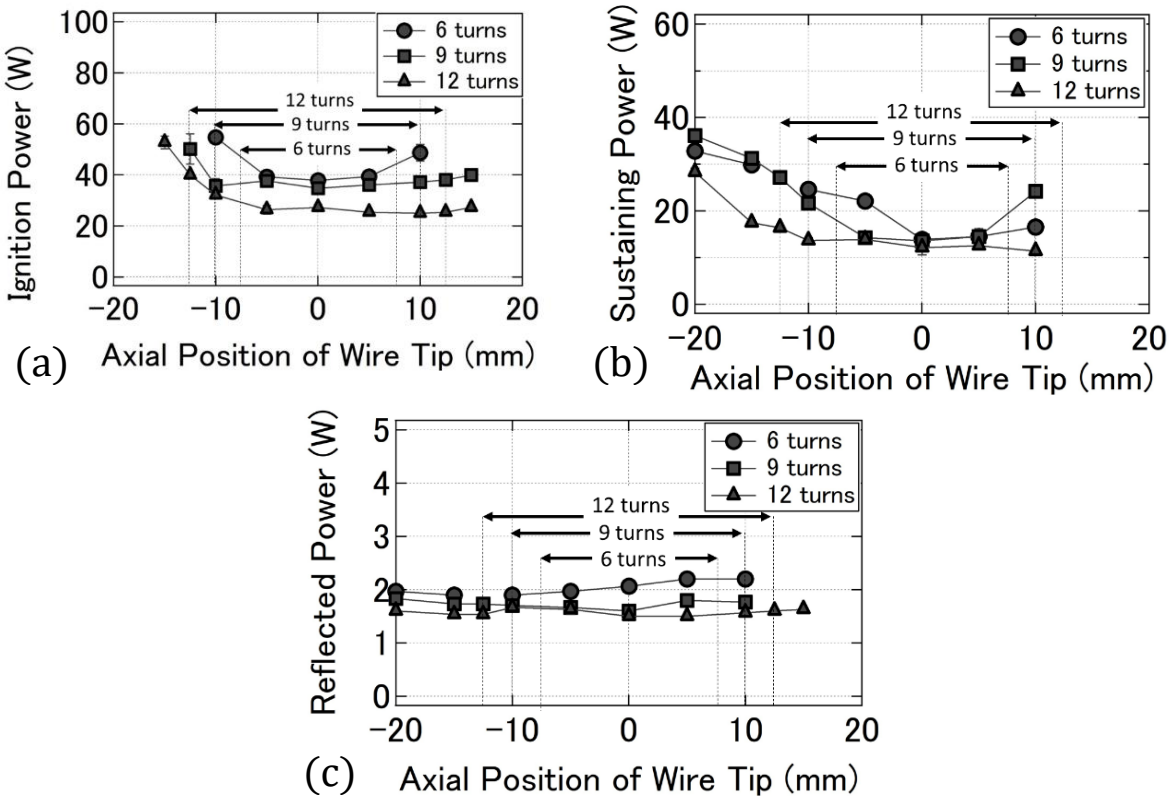

Figure 5.3 (a) Ignition power, (b) sustaining power and (c) reflected power measured when the ignition wire tip position is changed with respect to the midsection of the copper solenoid coil.

5.4 Longer plasma plume

The plasma plume with and without the ignition wire is shown in Figure 5.4. The plume length variation is shown when the power is changed for the operating mode when the ignition wire is not inserted. The plume is skewed towards the corner of the tube. The electric field is reconstructed to be higher near the tube walls, or the flow pattern was affected by the insertion of the wire.

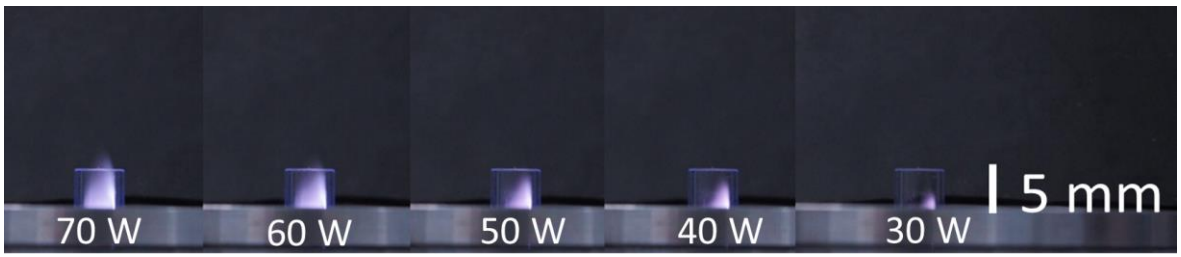

Figure 5.4 Plasma plume images of the Ar atmospheric pressure plasma produced by inductive coupling without the use of ignition wire. The flowrate used is 3 L/min.

Figure 5.5 shows the change in plume length when using the ignition wire. The plume length is generally longer when using the ignition wire compared when it is not used. The plume also converged towards the center which is in contrast when the ignition wire is not used. The electric field is higher near the edges of the ignition wire at this point causing the denser plasma to form at the wire's edge. A very important consequence of using the ignition wire is the repressed formation of the filamentary discharges. Homogenous glow plasma is the dominant mode of operation for the wire stabilized atmospheric pressure plasma.

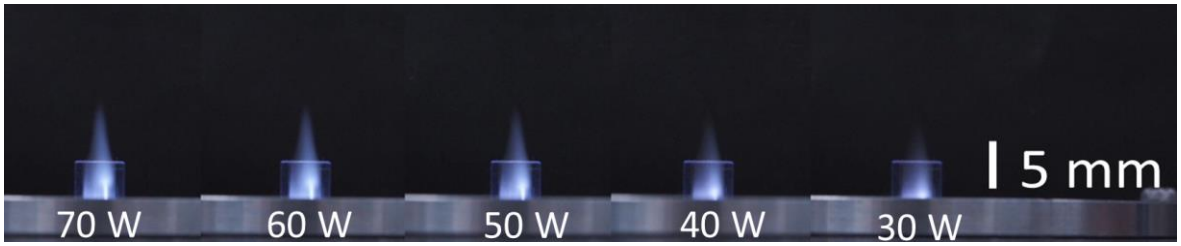

Figure 5.5 Plasma plume images of the Ar atmospheric pressure plasma produced by inductive coupling using the ignition wire. The flowrate used is 3 L/min.

5.5 Signal stability

The signal stability analysis was done using the ion mobility spectrometer. The Gerdien condenser is composed of concentric cylindrical electrodes and a fan blower as shown in Figure 5.6. The outer electrode sweeps the voltage from -15 V to +15 V while the inner electrode measures the ion currents passing through a highly sensitive ammeter referenced at the ground potential. A fan blower controls the flow of incoming ions depending upon the airspeed drawn into the conduit. Improvement of the Gerdien condenser was done using a conical glass tube in the orifice of the device. The conical glass tube guides the flow of incoming ions without neutralizing them on the wall. The orifice of the Gerdien condenser was positioned 17 mm from the discharge tip of the inductively coupled plasma. Measurements of ion density and ion mobility were done using the *I-V* characteristics.

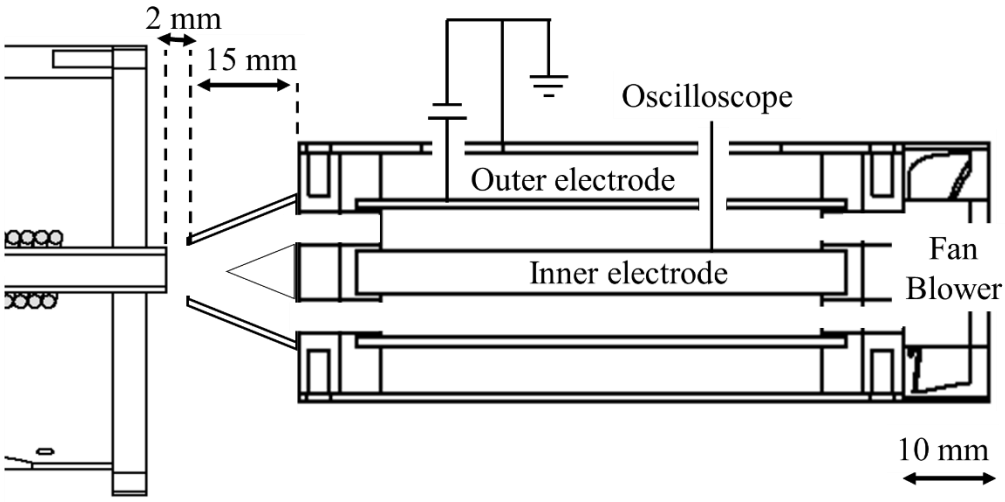

Figure 5.6 Schematic diagram of the Gerdien condenser coupled to the atmospheric plasma source.

The typical graphs of the *I-V* curve using the Gerdien condenser is shown in Figure 5.7 using 20-50 W RF power, 1 L/min Ar plasma for different plasma conditions. At 40 W, the saturation values of the negative and positive ions increase when using the ignition wire. A lower voltage using 5 V resulted in ion saturation with plasma condition without using the ignition wire while a higher sweep voltage of 15 V resulted in ion saturation for the plasma condition using the ignition wire. An asymmetric *I-V* curve is present with high RF power which is 50 W (without wire) and 40 W (with ignition wire). This may be due to the increased oxidation with the increase in ion density. The total positive ion density rises to 10.8 $x\ 10^6$ cm^{-3} when the RF power is increased from 20 W to 40 W (with wire). Without the wire, the total positive ion density measured to increase up to a 5.8 $x\ 10^6$ cm^{-3} by increasing the RF power from 40 W to 50 W. Ion mobility measurements reveal the possible presence of O^+ ions. There are several ways to recover the asymmetry including a reduction in the applied RF power as shown by the symmetric *I-V* curve when the plasma was excited at 40 W without the wire, and 20 W with the wire.

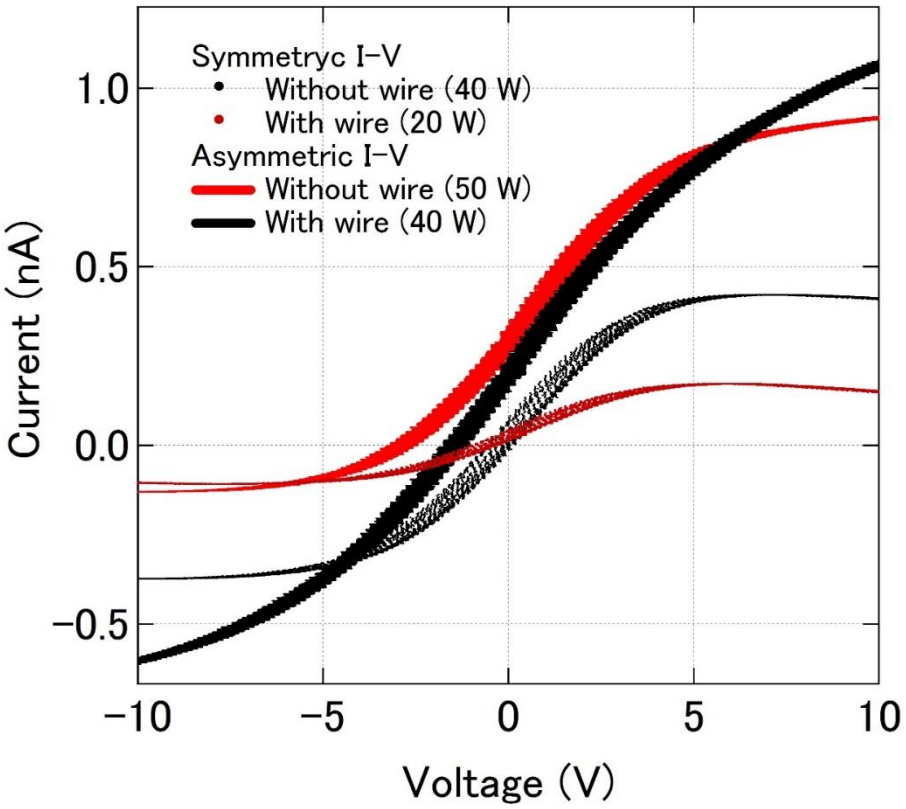

Figure 5.7 Typical *I-V* measurements of the Gerdien condenser from the ICP with and without the ignition wire.

The amplitude of the temporal changes in ion saturation current, which can be the noise onto the signal, of the output of the ion mobility spectrometer was measured for a constant applied outer electrode voltage of +5 V. The results are plotted in Figure 5.8. An increase in amplitude is observed with an additional input of RF power. The amplitude also significantly increased when the ignition wire was used compared with the condition when no ignition wire was used. A minimum amplitude was measured when plasma was sustained with the minimum power of 15 W (with wire).

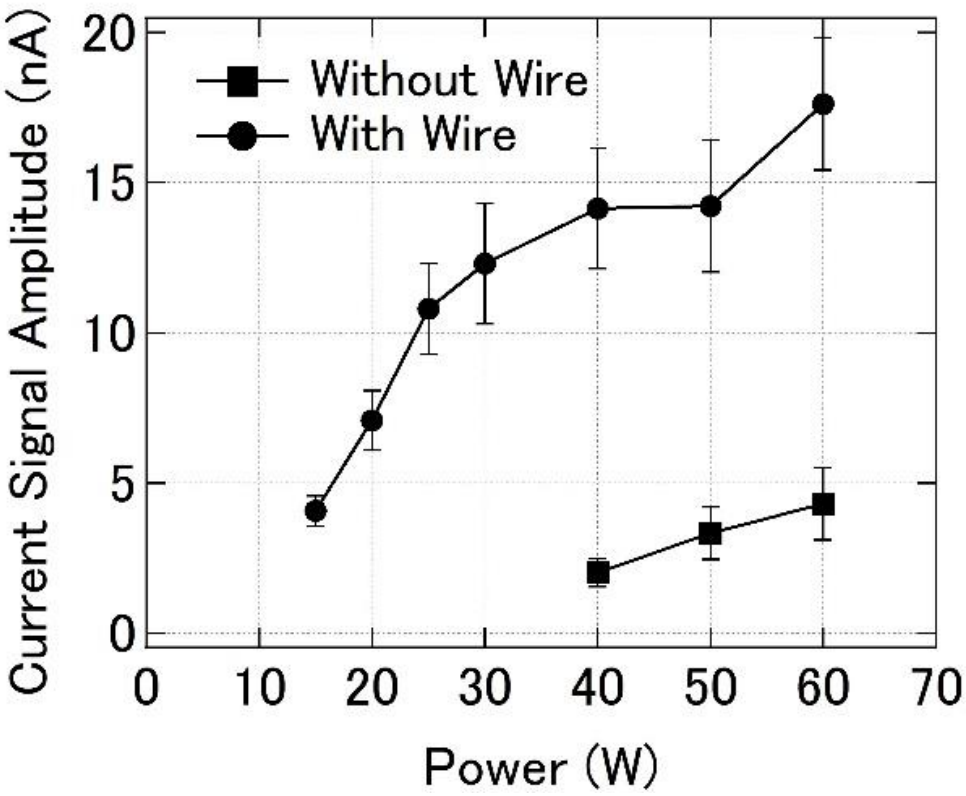

Figure 5.8 Amplitude measurements of the temporal change in ion current saturation with +5 V constantly applied voltage to the Gerdien condenser.

Frequency spectrum analyses of the signal measured by the Gerdien condenser is shown in Fig. 5.9. The peak signal changes in accordance with the power input. A consistent peak of less than 40 Hz was observed when using the ignition wire with 40-60 W RF power. For a frequency below 40 Hz, the measured noise may possibly due to the thermal fluctuations and mechanical vibrations due to the blower fan of the Gerdien condenser.

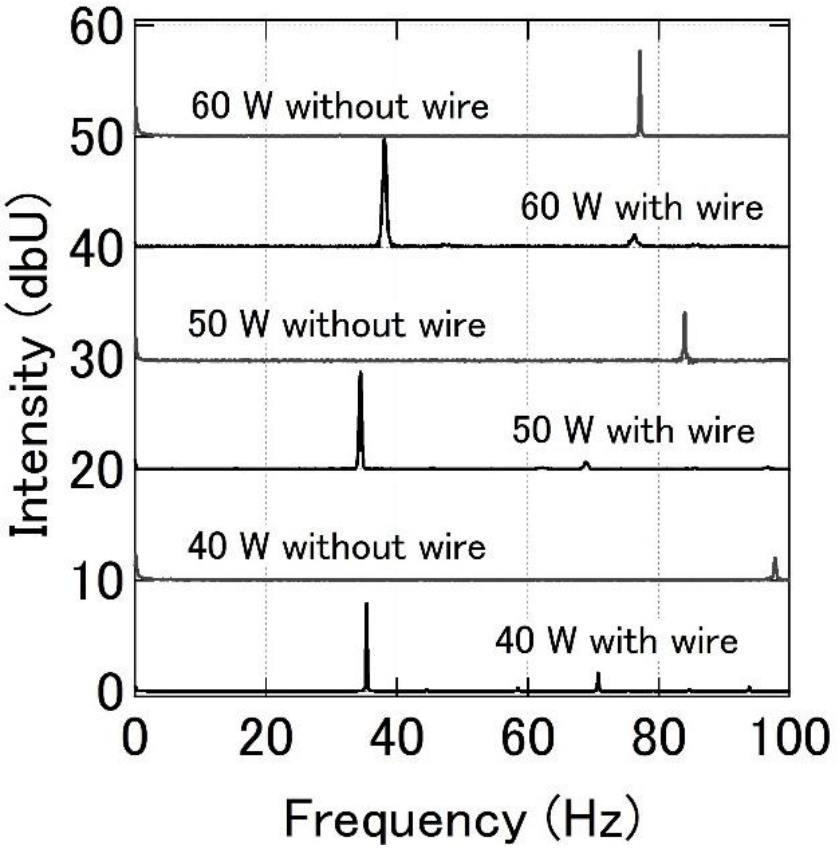

Figure 5.9 Fourier transform signal analysis using the Gerdien condenser.

5.6 Summary

The stability of an atmospheric pressure plasma source (APPS) for ion mobility spectrometer applications was investigated. Optimizations of the APPS for the operating conditions such as coil size and position for a plasma inductive excitation and the ignition wire location were attempted. Ignition of Ar plasma is facilitated by the difference in electric potential inside the coil and the distance between the coil and the aluminum base attached to the ground terminal. Characterization of the ignition conditions, *I-V* measurements using a Gerdien condenser, and noise level in the ion current output signals were done for the developed APPS. The insertion of the ignition wire was found to affect the amplitude and value of the transported ion current through the Gerdien condenser.

Smooth ignition of Ar plasma is facilitated by inserting a metal wire inside the glass tube held in the RF coil winding. Improved ignition was also observed with a change in wire tip location. The insertion of ignition wire tip results in more signal but it also increased the noise on the collected current. The power necessary to ignite Ar plasma by the developed APPS was reduced with an increase of the coil turn number and a decrease in the coil aluminum base distance.

Chapter 6
Electric Probe Measurements of Atmospheric Pressure Plasma

6.1 Introduction

Prior to the introduction into a high-resolution mass analyzer system, ion mobility devices separate lighter mass ions from the target large size molecules in the atmospheric phase. Fragmentations of molecules are determined by the ionization process, and studies are being made to improve ion source performance to realize a highly accurate chemical analysis system. The ionization process is therefore studied using an electric probe. The electric probe has a simple configuration to clarify plasma parameters, quantify concentrations of charged particles, and determine electron temperature [25].

The theory to use electric probes for atmospheric pressure plasma largely differs from the one for reduced pressure plasma due to a decrease in mean free path and ambiguous plasma potential [26]. The plasma potential fluctuates when plasma drifts forming a path of electric current, or due to the presence of RF field which leads to erroneous plasma parameters [27]. On the other hand, double probes and emissive probes are more efficiently used for fluctuating plasma potential [25–28]. The double probe is a floating probe used to obtain saturation as the two probes are referenced to each other. The derivative of the symmetric *I-V* measurements in double probes is used

to obtain the electron temperature. Varied probe separation can also be used to obtain the plasma conductivity and determine charge density species [25].

Meanwhile, emissive probes are heated probes used to measure local plasma potential [29–32]. The hot probe emits electrons which are released into the plasma below the plasma potential and trapped into the probe sheath above the plasma potential [29]. Different heating techniques are being used including Joule heating, indirect heating, self-emission, secondary electron, capacitive emissive probes, and laser heating [32]. Every heating scheme is simple and easy to employ but each has its own demerits.

The problem of undetermined plasma potential also arises when the ion source excites a plasma in an insulating tube through inductively coupling the radio frequency (RF) power to the plasma. This study investigates the effect of the ignition wire to the *I-V* measurements in atmospheric pressure plasma. Probe location, diameter, and the source operation parameters were changed to investigate the effects of the probe *I-V* characteristics. Moreover, the hysteresis in the *I-V* characteristics is observed and associated with the desorption process in the atmospheric pressure plasma. The hysteresis in the *I-V* characteristics is mostly linked to impurities in low-pressure plasma.

6.2 Double probe

6.2.1 Description of the probe

The double electric probe is composed of two 0.35 mm diameter, 90 mm long tungsten wire inserted inside a *V*-shaped double hole ceramic tube. The position of the probe inside the quartz tube is shown in Figure 6.1(a) and the description of the probe is shown in Figure 6.1(b). One of the wires is connected to a voltage source while the other wire is a reference wire which is connected to the ground terminal. The probe voltage was swept from -35 V to +35 V between the tips and the current was simultaneously measured.

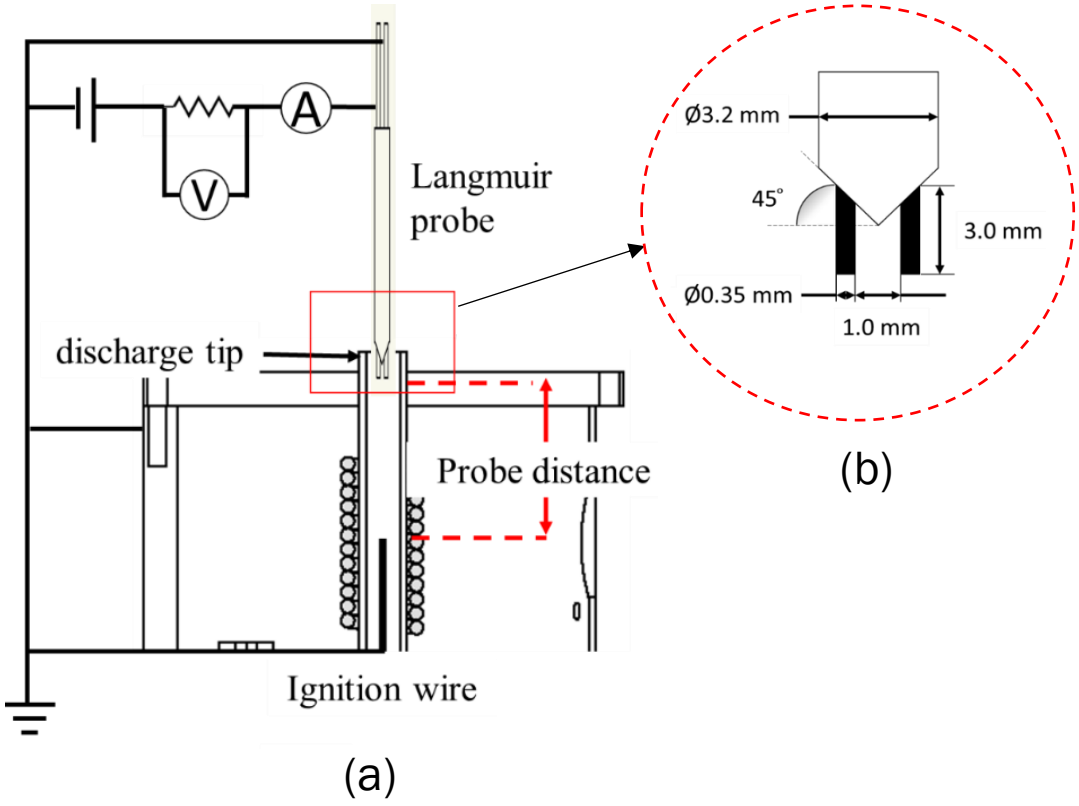

Figure 6.1 Position (a) and description (b) of the electric probe.

6.3 *I-V* measurements

Figure 6.2 shows the raw data of the typical *I-V* measurements and the derivative of the *I-V* measurements. The arrows point the curves to their corresponding axis. The *I-V* measurements are symmetric with respect to the zero-axis as revealed by the uniform distribution in the $|dI/dV|$ with respect to the probe voltage.

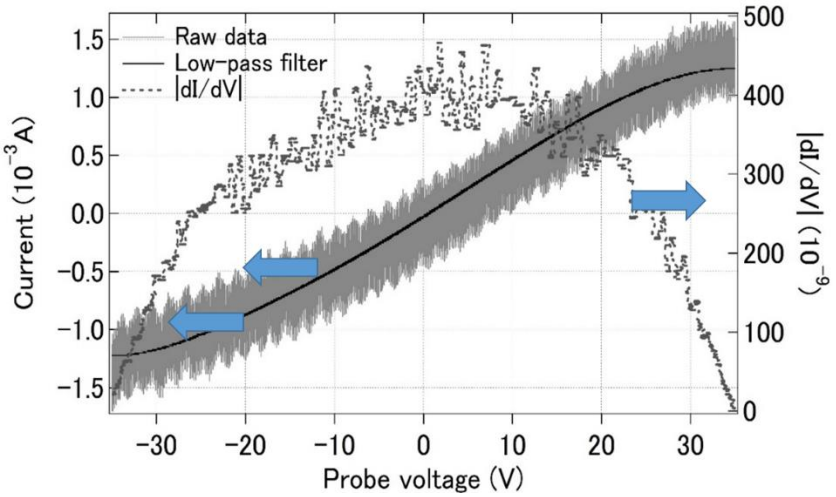

Figure 6.2 Typical *I-V* measurements using the double probe.

The noise in the *I-V* measurement of the electric probe is characterized by the amplitude and offset in the raw data. The amplitude of the sinusoidal current from the raw data and the current offset measured using the *y*-axis (current) displacement (at $x=0$) using the low-pass filter curve are measured as shown in Figure 6.3.

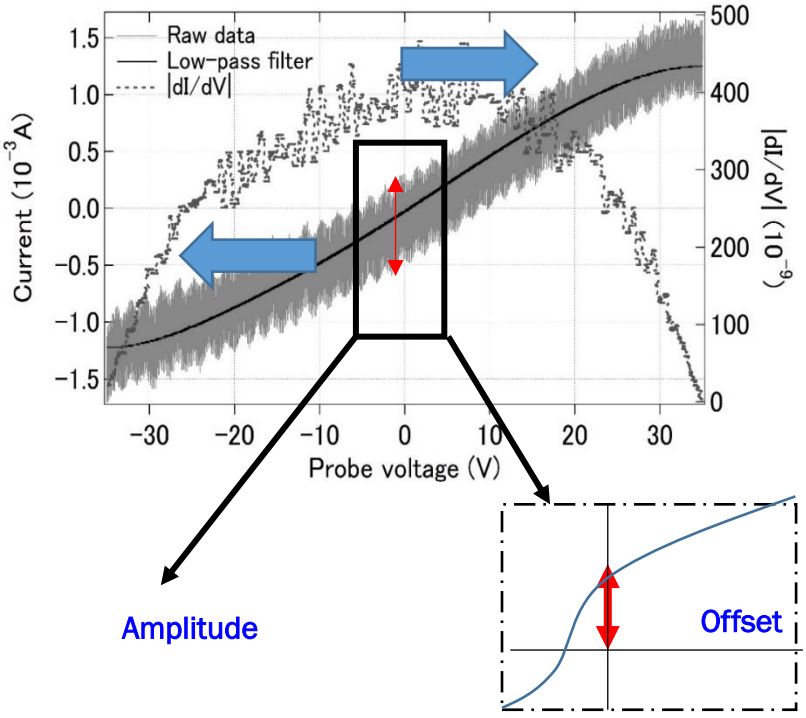

Figure 6.3 Schematic diagram of the noise amplitude and offset.

Figure 6.4(a)-Figure 6.4(c) shows the noise amplitude and offset measurements with increasing RF power, Ar flowrate, and probe distance. The amplitude and offset increased with additional input of RF Power and Ar flowrate. An increase in probe distance reduced the noise amplitude and offset. Minimum RF power and Ar flowrate results in minimum signal amplitude and offset. The heating of the ignition wire mainly caused an increase in the noise amplitude. The same problem of the enhanced noise was observed on the ion mobility spectrometer signal. The larger RF input power can cause higher electrode temperature resulting in the emission of adsorbed gas from the electrode into plasma. Filamentations of the plasma are often observed at higher Ar flow rates to fluctuate the path of the electric current but the possible reasons for observing noise still need to be addressed.

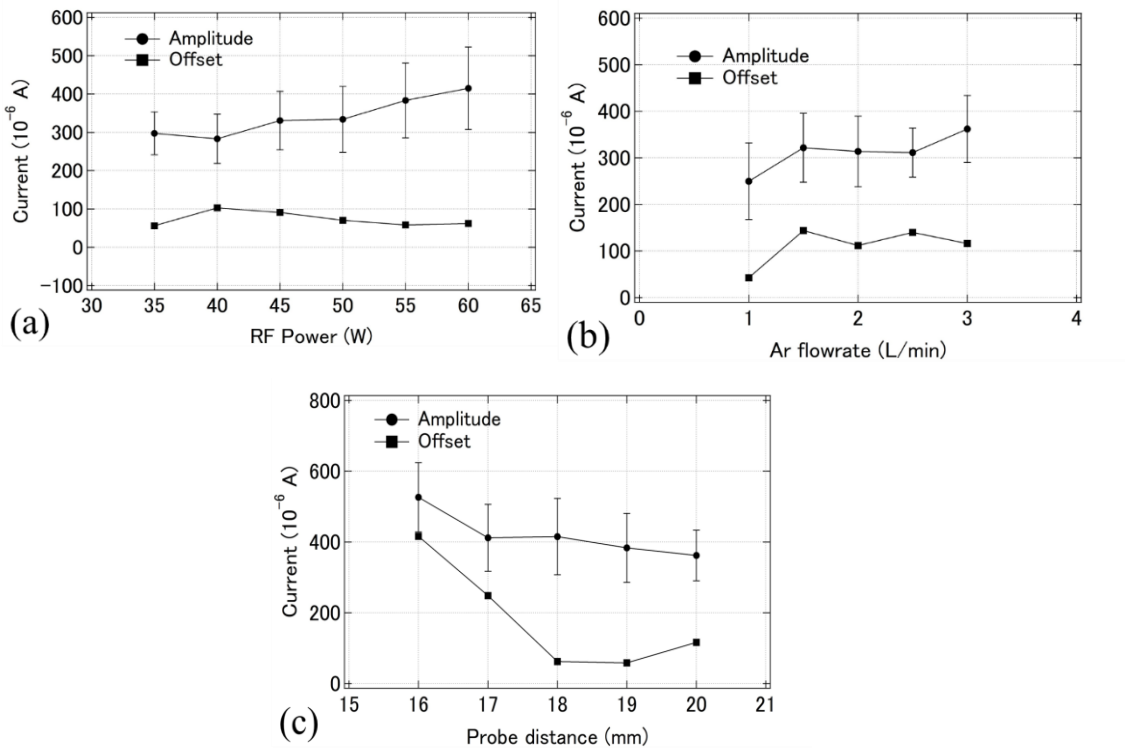

Figure 6.4 Amplitude and offset measurements using varied RF power (a), Ar flow rate (b), and probe distance (c).

Figure 6.5(a)-Figure 6.5(c) shows the negative and positive saturation currents and the slope of the *I-V* characteristic at *V*=0 measured for varied RF power, Ar flow rate, and probe distance. The saturation currents increased with additional input of RF power and decreased with higher Ar flow rate and larger probe distance. The symmetric *I-V* characteristics show equal current collection by both electrodes; they are identical in current collection performance. The symmetry is broken with increased RF power where the negative current saturation is slightly greater than the positive current saturation. At 60 W, the symmetry appeared to improve when the Ar flow rate was set at 1.5 L/min. The *I-V* measurements become more asymmetric with

increasing probe distance, possibly indicating the development of a homogeneous plasma far from the electrode which can possibly serve as the electron source that can heat up electron collecting probe surface.

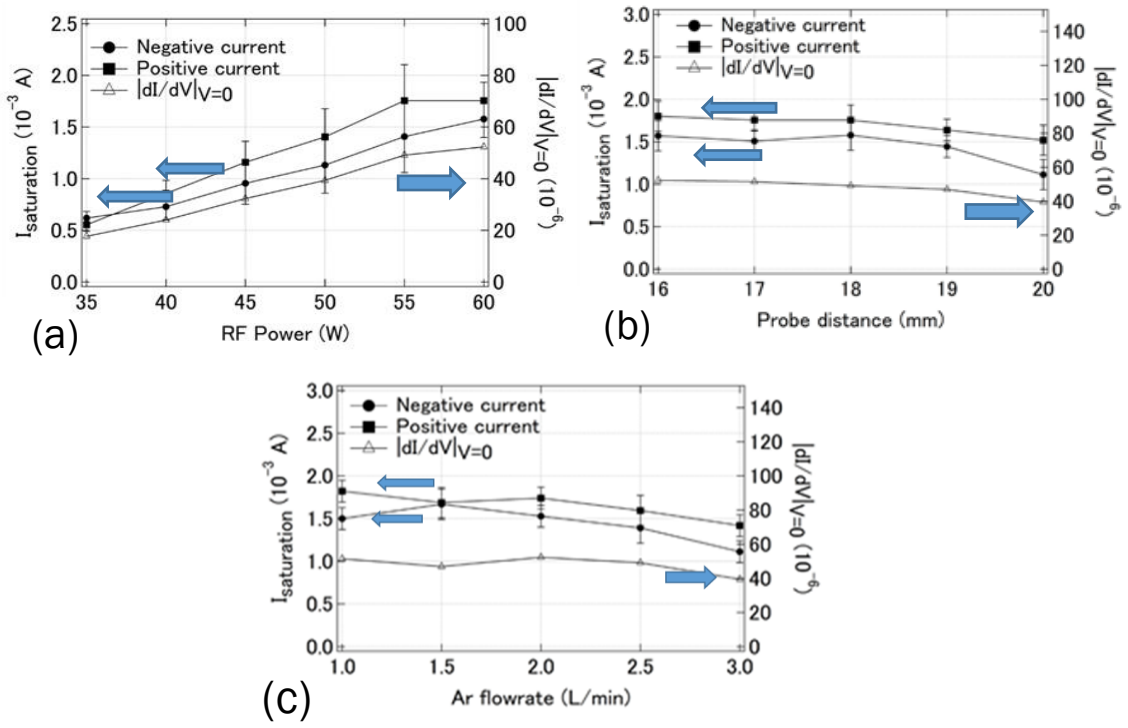

Figure 6.5 Negative and positive current saturation, and $|dI/dV|_{V=0}$ measurements using varied RF power (a), Ar flow rate (b) and probe distance (c).

6.3.1 Electron temperature

The electron temperature for typical double probe measurements can be derived from the probe currents [33] for probe-1 and probe-2 which can be written as

$$I_{p(1,2)} = A_{(1,2)} \frac{en_e}{4} \sqrt{\frac{8\kappa T_e}{\pi m_e}} \exp(\phi_{p(1,2)} - I_{iS(1,2)}) \tag{6.1}$$

where e is the electronic charge, $n_e(m^{-3})$, $T_e(K)$ and $m_e(kg)$ are the density, temperature, and mass of the electron, $A_{(1,2)}(m^2)$, and $I_{iS(1,2)}(A)$ are the surface area

and the ion saturation current for probe-1 and probe-2, respectively. The nondimensional probe potential $\phi_{p(1,2)}$ is

$$\phi_{p(1,2)} = -\frac{e(\varphi - V_{p(1,2)})}{\kappa T_e}. \tag{6.2}$$

The gradient of the graph of *I-V* characteristics curve for symmetric double probe at $I_p = 0$ can be written as

$$\left(\frac{d\phi_p}{dI_p}\right)_{I_p=0} = \frac{\eta(A)}{I_{i,sat}} \tag{6.3}$$

where $I_{i,sat}$ is the saturation current, $\eta(A)$ is a function of Debye ratio, ion and electron temperatures ratio, and area ratio of the two probes. The value of $\eta(A)$ is approximately

$$\eta(A) = c_1\left(1 + \frac{1}{\sqrt{A}}\right) = 3.08 \times \left(1 + \frac{1}{\sqrt{A}}\right) \tag{6.4}$$

where c_1 is the electric current factor and A is just equal to 1. The detailed approximation of these variables is found elsewhere[33]. Finally, the electron temperature is

$$T_{eV} = \left(\frac{I_{i,sat}}{6.16}\right) \Big/ \left(\frac{dI_p}{dV_p}\right)_{V_p=0} \tag{6.5}$$

The high-pressure and flowing nature of the plasma can affect measurements of T_{eV} if electrons are sufficiently cooled by heat transfer to the colder probe, thus the measured temperature is lower than the bulk temperature.

The electron temperature measurements are shown in Figure 6.6(a)-Figure 6.6(b). The electron temperature ranges from 5.13 eV to 6.33 eV. There are no significant effects of changing the power, Ar flowrate and probe distance in the electron temperature of the atmospheric pressure plasma. It may be due to the small range of RF power, Ar flowrates and probe distance used.

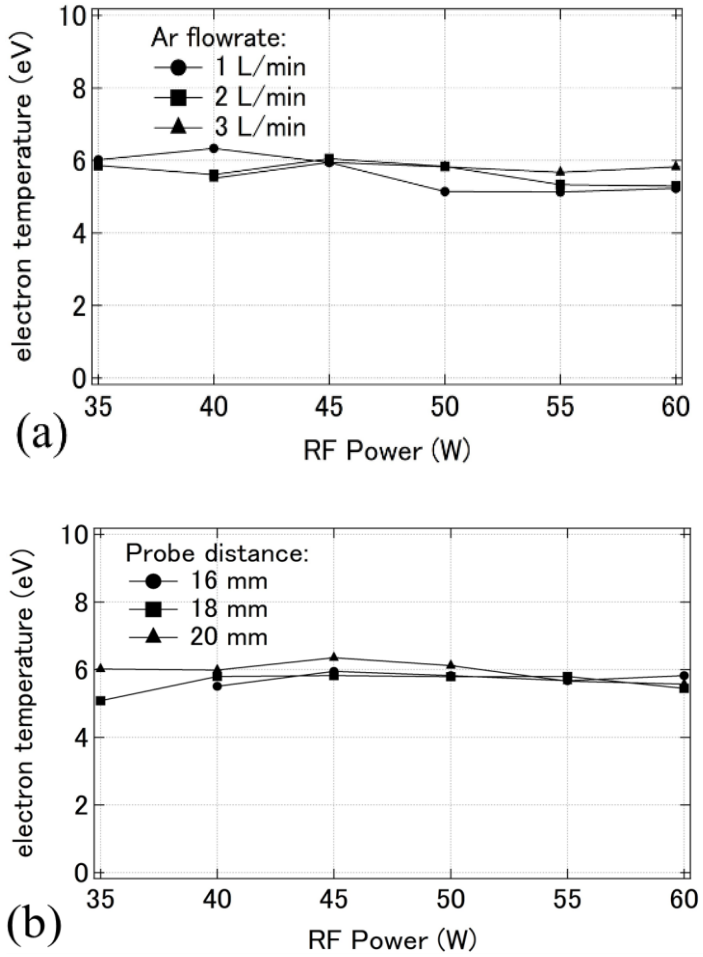

Figure 6.6 Electron temperature measurements using increasing RF power for various Ar flowrate (a) and probe distance (b).

6.3.2 Space potential

A bias voltage was applied to the ignition wire to see if it is possible to vary the plasma space potential of the atmospheric pressure plasma by electrically biasing the wire. The effects of the bias voltage to the *I-V* measurements are shown in Figure 6.7(a) which is still symmetric with respect to zero axes. The current saturation and slope measurements are shown in Figure 6.7(b). Positive bias voltage increased the positive

current saturation while negative bias voltage decreased the negative current saturation. The bias voltage drastically decreased the slope of the *I-V* curve resulting in enlarging the uncertainties in electron temperature measurements.

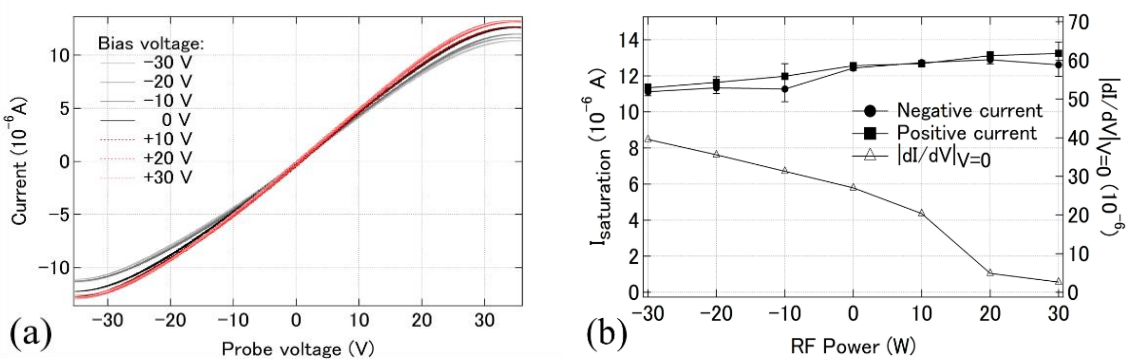

Figure 6.7 *I-V* curve (a) and current saturation and slope measurements (b) using a bias voltage in the ignition wire.

6.4 Counter double electrostatic probe

The presence of the ignition wire which is connected to the ground terminal was utilized as a counter reference electrode to a biased electrostatic probe. In this set-up, the wire electrode invented to ease the ignition of an atmospheric pressure plasma can also determine the local plasma potential as it is biased with respect to the probe driving electrical circuit [24]. This set-up also made it possible for the measurement of the temporal variations of the current saturation. Scanning the temporal variations of current saturation is useful for determining plasma stability.

The schematic diagram of the counter double electrostatic probe is shown in Figure 6.8. A bias voltage was applied to probe placed near the opening of the plasma discharge. Since the ignition wire is grounded, the floating potential of the plasma remained fixed near the zero potential. The probe is composed of 0.35 mm thickness,

90 mm long tungsten wire placed inside a ceramic tube. The ignition wire's diameter was then changed to 0.35 mm and placed in a ceramic tube to match the probe.

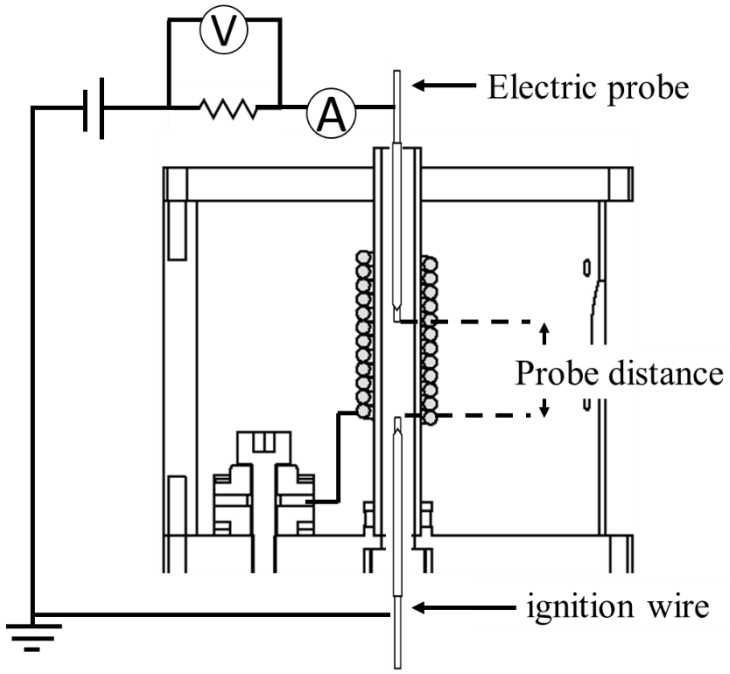

Figure 6.8 Schematic diagram of the counter double electrostatic probe.

6.4.1 Asymmetric in *I-V* measurements

Figure 6.9 shows the *I-V* measurements of the Ar plasma using a 2 L/min gas flow rate and probe distance 10 mm. The RF power was varied from 20 W to 60 W. Asymmetric *I-V* measurements are collected due to the counterflow of ions and electrons in one of the probes. The positive saturation current is larger in magnitude than the negative current. Increasing power also increased the magnitude of positive and negative current saturations.

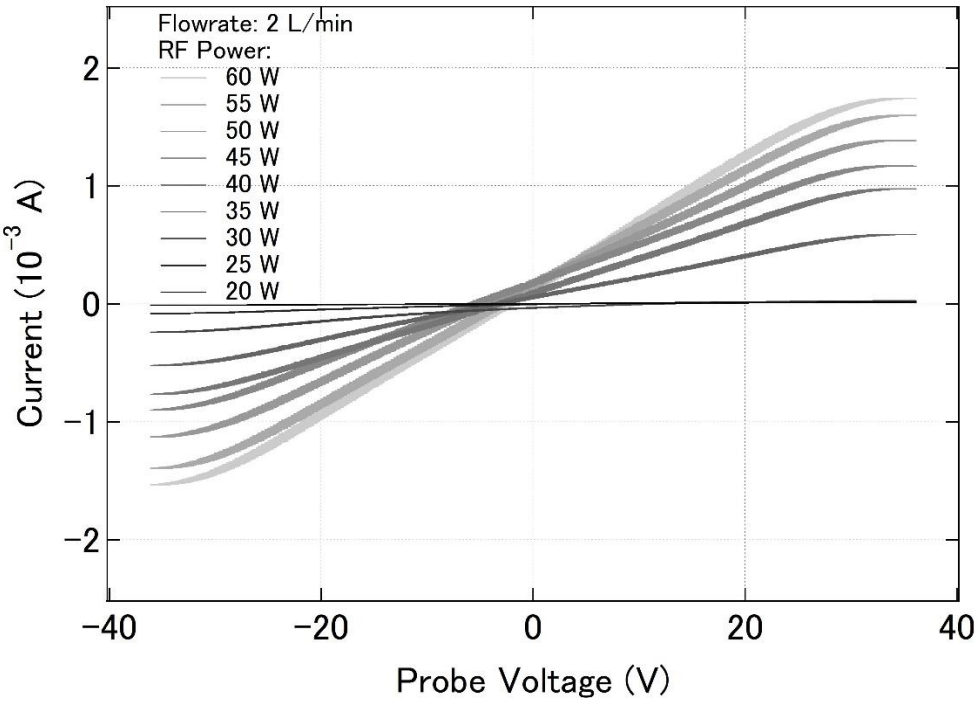

Figure 6.9 *I-V* measurements of the Ar plasma using a 2 L/min gas flow rate. The RF power was varied from 20 W to 60 W.

The asymmetry is the *I-V* measurements of the counter double probe electrostatic probe is further investigated in Figure 6.10. This graph also shows the derivative of the *I-V* measurements using 50 W power, 2 L/min Ar flow and probe distance of 10 mm. A higher magnitude of the positive current saturation which is 1.6 μA is measured compared to the 1.15 μA measured in the negative current saturation. Asymmetry is caused by the counterflow of gas in one of the probe wire.

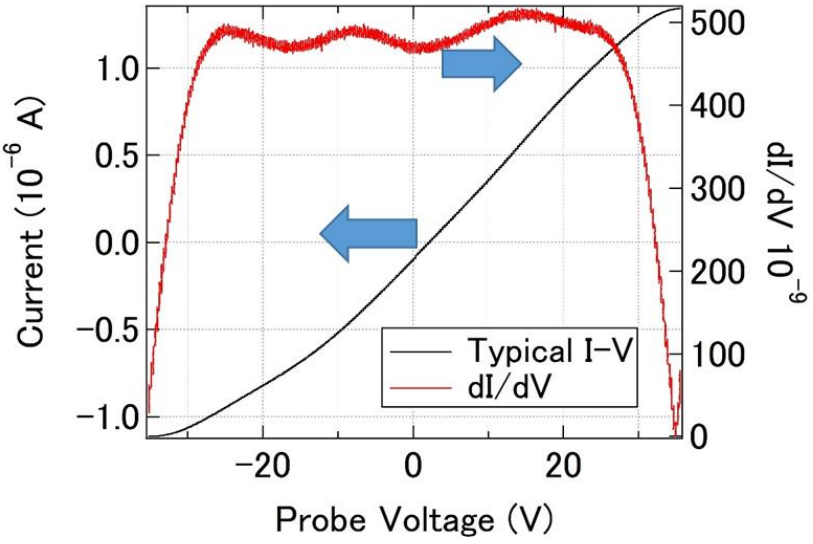

Figure 6.10 Typical *I-V* measurements and the derivative of the *I-V* measurements using 50 W, 2 L/min. The asymmetry is apparent when comparing the values of the positive and negative current saturation.

6.4.2 Hysteresis

Figure 6.11(a) shows the typical hysteresis in the *I-V* measurements using the single electric probe. The *I-V* measurements are collected from increasing biased voltage first which is from -44 V to +44 V. Afterwhich, the voltage is swept from +44 V to -44 V. The current is displaced causing the hysteresis in the *I-V* measurements. Impurities on the surface of the probe are the main cause of current hysteresis in low-pressure plasma. However, in this study, the main cause of impurities can arise from the ignition wire. The properties of the surface of the ignition wire are unstable through time caused by thermal fluctuations from turning the device on and off. This presence of hysteresis in the *I-V* measurements, therefore, suggests the desorption process in the ignition wire caused by the surrounding energetic atmospheric pressure plasma; for example formation of tungsten oxide.

If this method is used as an ambient desorption/ionization source in mass spectroscopy, the effect of the unstable surface properties of the ignition wire should be minimized. Minimizing the effects of hysteresis in the *I-V* measurements is observed with a decrease in total time sweep as shown in Figure 6.11(b).

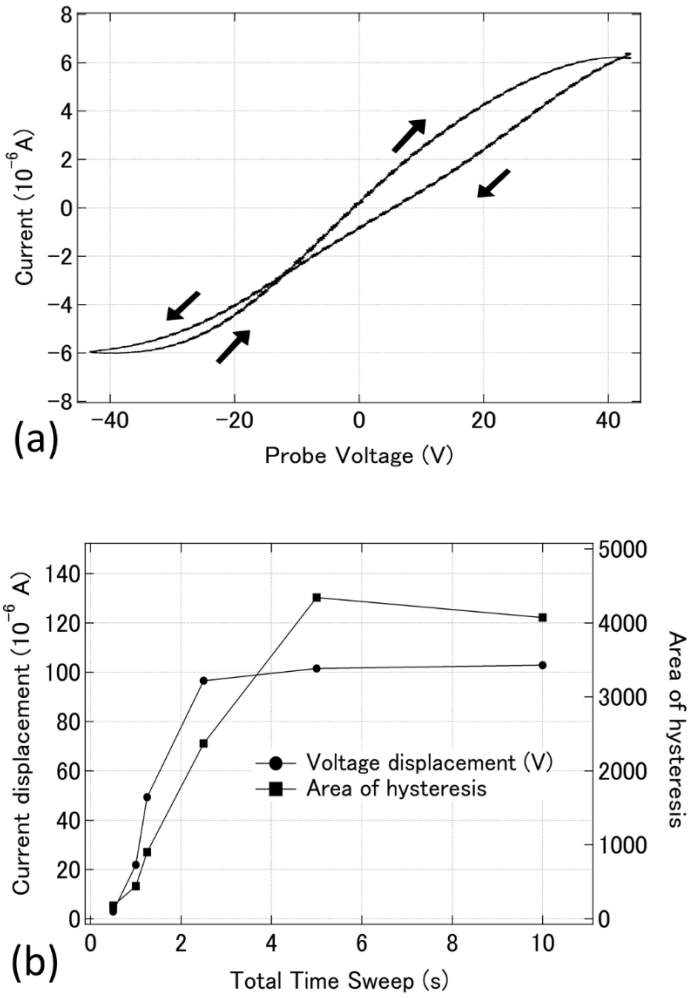

Figure 6.11 Typical hysteresis in the *I-V* measurements of a single electric probe. Changes in current displacement and hysteresis area are measure with varying (b) time sweep.

6.4.3 Signal fluctuation

Figure 6.12 shows the temporal variation of the current saturation for the low power (30 W) and high power (60 W) where higher power measures higher current saturation compared to the low power plasma. The amplitude of the current measurements is greater in the 60 W compared to the 30 W. This could mean that less noise is measured. The word noise was introduced in the early days of radio communication to describe "any unwanted (electrical) signal within a communication system that interferes with the sound being communicated", which is distinct and loud as headphone noise. In the context of the physical experiment, the word noise is more general and refers to "any unintentional fluctuations that appear on top of signals to be measured". In electronic circuits, voltage noise and current noise are caused by among others the thermal fluctuations of the electron carriers. In the radio and microwave region, the electro-magnetic fluctuations are caused by the thermal or spontaneous emission of low-energetic photons.

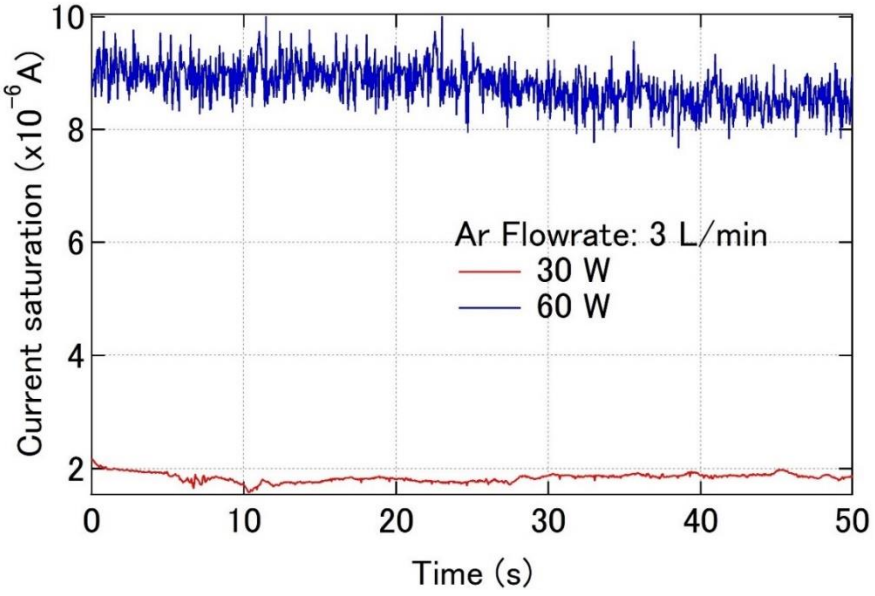

Figure 6.12 Temporal variations of current saturation measure using an electric probe.

Further investigation of the temporal variation of the saturation current shows a linear decrease of the current saturation. Figure 6.13 shows the decrease in the current saturation and the linear fit used for the temporal variations. The linear fit has a negative slope corresponding to smaller plasma density. The seemingly constant fluctuation amplitude is hypothesized to be the increase in thermal noise in the inductive elements through time.

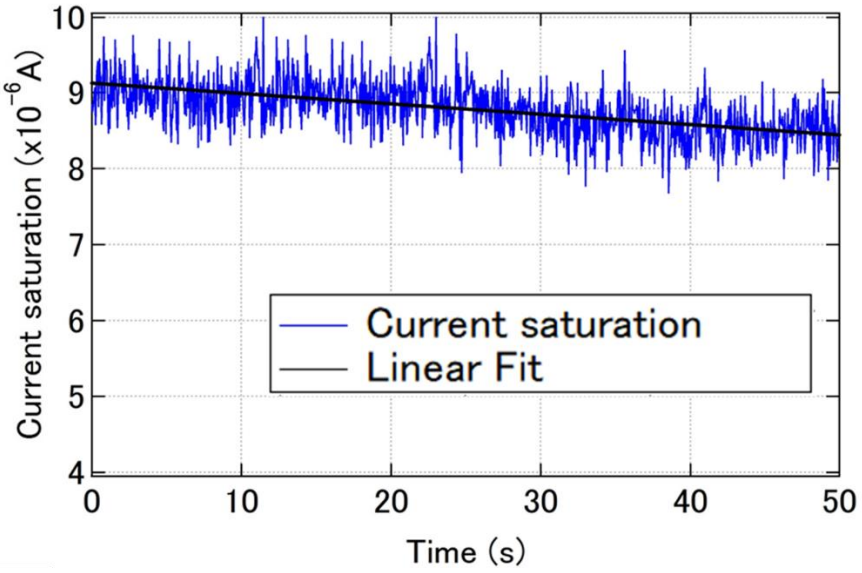

Figure 6.13 Decreasing current saturation through time.

The thermal increase in the inductor can easily be measured using an infrared camera. Figure 6.14(a) and Figure 6.14(b) shows the increase in temperature of the coil used as an inductor element. The graph also shows the ratio of the current saturation at 50 s and 0 s. A ratio of fewer than 1 means a decrease in current saturation through time. Increasing the RF power results in higher coil temperature and decreasing ion saturation.

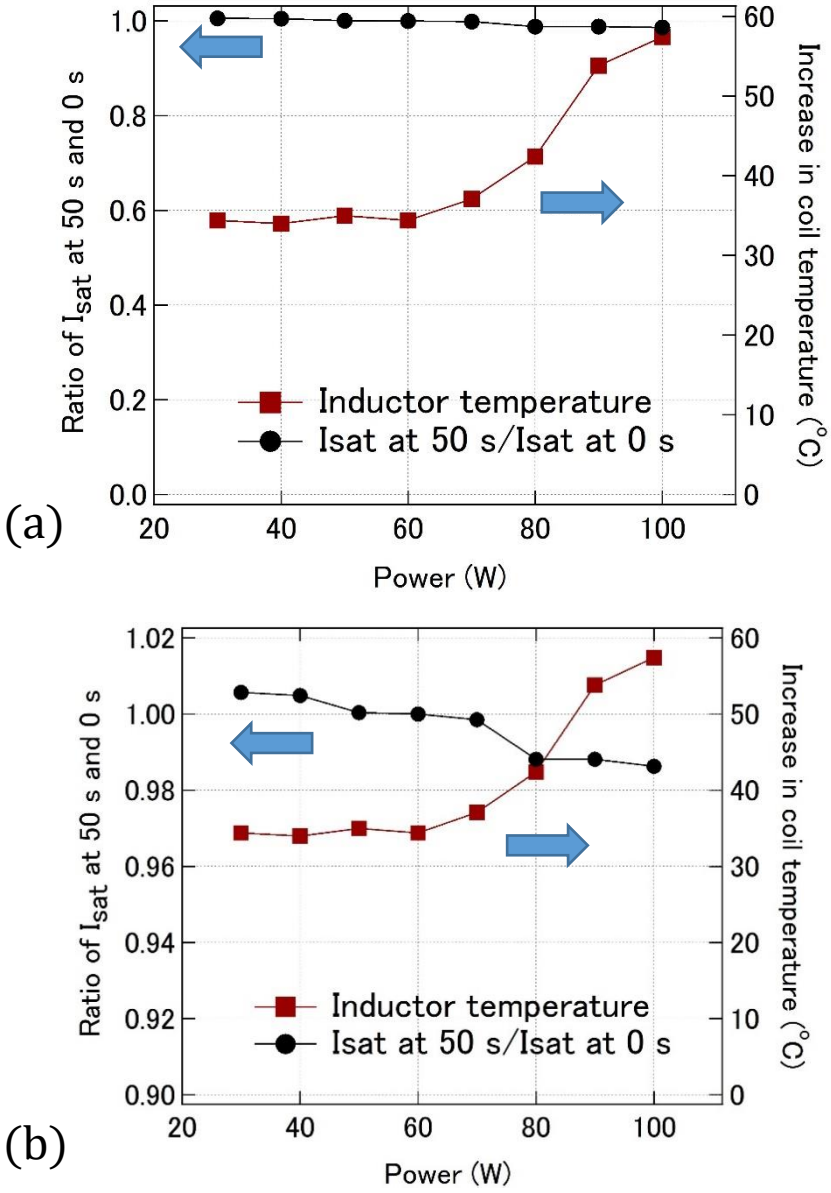

Figure 6.14 (a) Ratio of the current saturation measured at 50 s and 10 s is correlated to the increase in coil temperature. (b) The y-axis range is decreased to 0.90-1.02 to give emphasis on the decreasing trend.

6.5 Summary

The ionization process in the wire stabilized atmospheric pressure plasma is studied using a double electric probe. Noise amplitude and current offset are observed from the *I-V* measurements. The heating of the ignition wire mainly caused the increase in noise amplitude and offset in the *I-V* measurements of the double probe. The electron temperature appeared to range from 5.1 eV to 6.3 eV. Positive bias voltage increased the positive current saturation whilst negative bias voltage decreased the negative current saturation. The bias voltage substantially reduced the slope of the *I-V* curve indicating lower temperature.

Due to the presence of the ignition wire which is connected to the ground terminal, the floating potential of the plasma remained fixed near the zero potential. This lead to the counter double electrostatic probe. Asymmetric *I-V* measurements are collected due to the counterflow of ions and electrons in one of the probes.

The current hysteresis in the *I-V* measurements is observed which is associated with the impurities in the ignition wire. The properties of the surface of the ignition wire are unstable through time caused by thermal fluctuations from turning the device on and off. This presence of hysteresis in the *I-V* measurements, therefore, suggests the desorption process in the ignition wire caused by the surrounding energetic atmospheric pressure plasma.

Chapter 7
Electric Probe Measurements for Simultaneous Spectrometer Analysis

7.1 Introduction

In the previous chapter, the grounded wire with the primary use for plasma stabilization was found out to perform as the reference probe for the determination of plasma potential. This leads to a new structure of the wire-stabilized atmospheric pressure plasma for simultaneous electric probe monitoring while being used for ion mobility spectrometer or mass spectrometry applications.

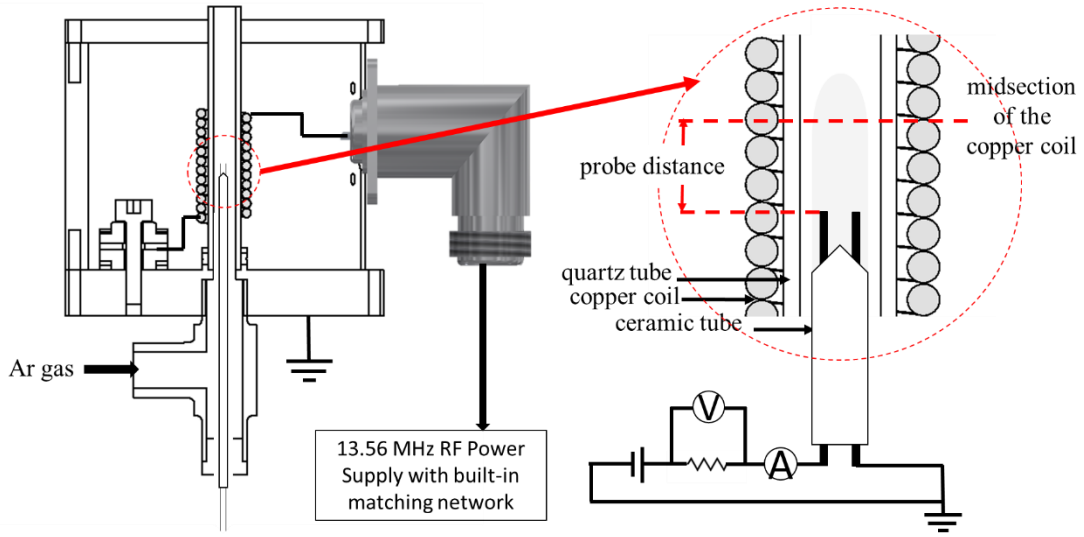

Figure 7.1 Double probe like structure in the upstream flow of Ar gas.

Figure 7.1 shows the double-probe-like structure placed at the upstream flow position of the Ar gas. The structure is composed of two 0.7 mm tungsten wires where

one wire acts as the plasma igniter during plasma production and subsequently as the reference electrode during electric probe measurements.

7.2 *I-V* symmetry

Typical *I-V* measurements show asymmetry where the negative current saturation value is larger than the positive current saturation as shown in Figure 7.2. The first derivative is also shown in the figure where plasma potential is zero. This is expected since it follows the potential of the reference electrode which is connected to the ground terminal.

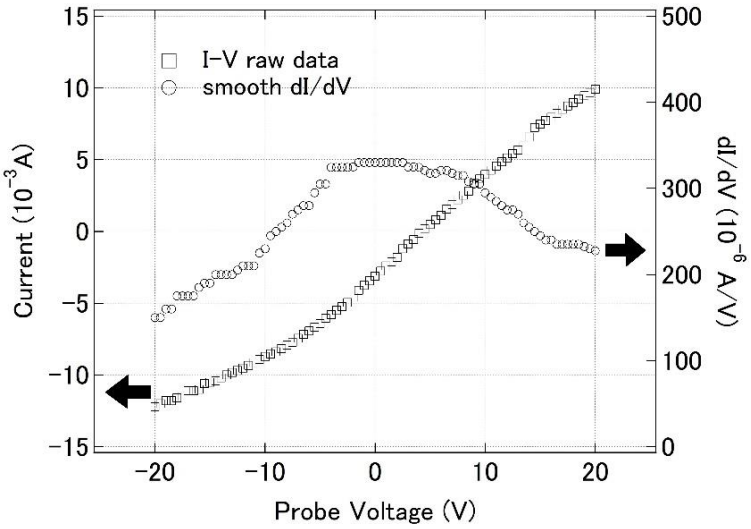

Figure 7.2 Typical *I-V* measurements.

The changes in the current saturation were measured for varied Ar flow rate as shown in Figure 7.3(a). Rapid increase in the negative current saturation is observed while an almost constant positive current saturation is measured. The value of the slope increase with additional Ar flow input. For increasing RF power, an increase in

the negative current saturation was measured as shown in Figure 7.3(b). The positive current saturation is almost constant. The current-voltage derivative at zero voltage slightly increased with additional input of RF power. The visual look of the *I-V* measurements is shown in Figure 7.4 which is comparable to an emissive probe trace for increased probe temperature. The electrons are trapped inside the plasma sheath due to heating of the probe which resulted in constant positive current saturation with increased RF power.

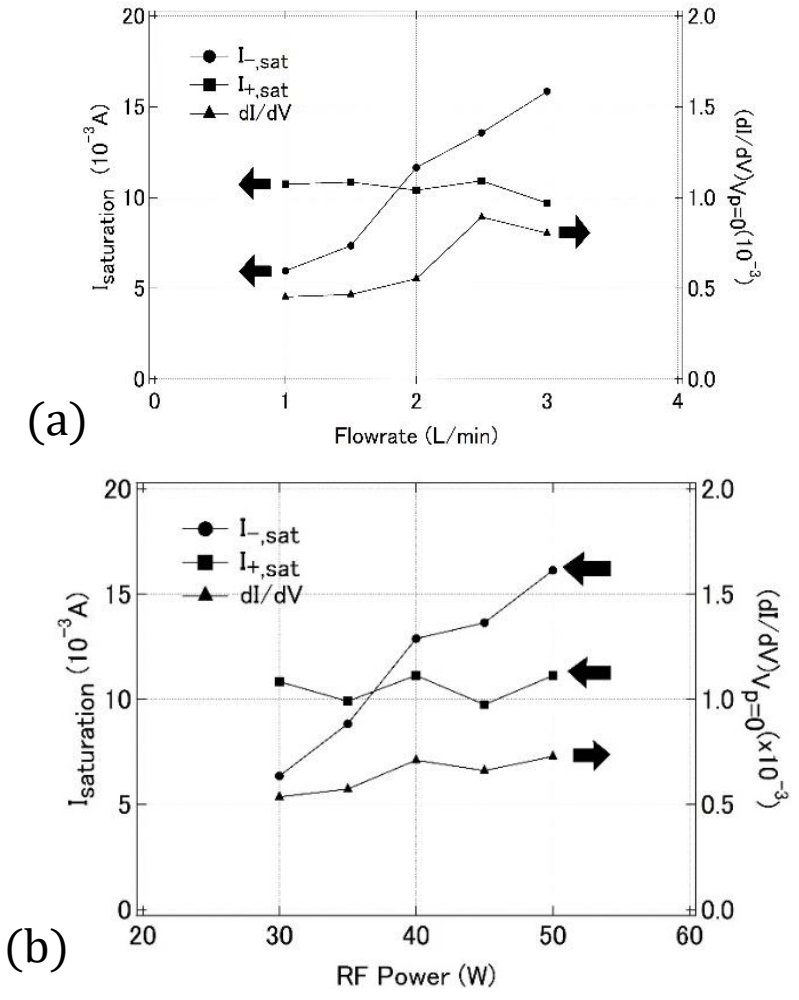

Figure 7.3 Current saturation measurements and first derivative values for (a) varied Ar flowrates and (b) varied RF power.

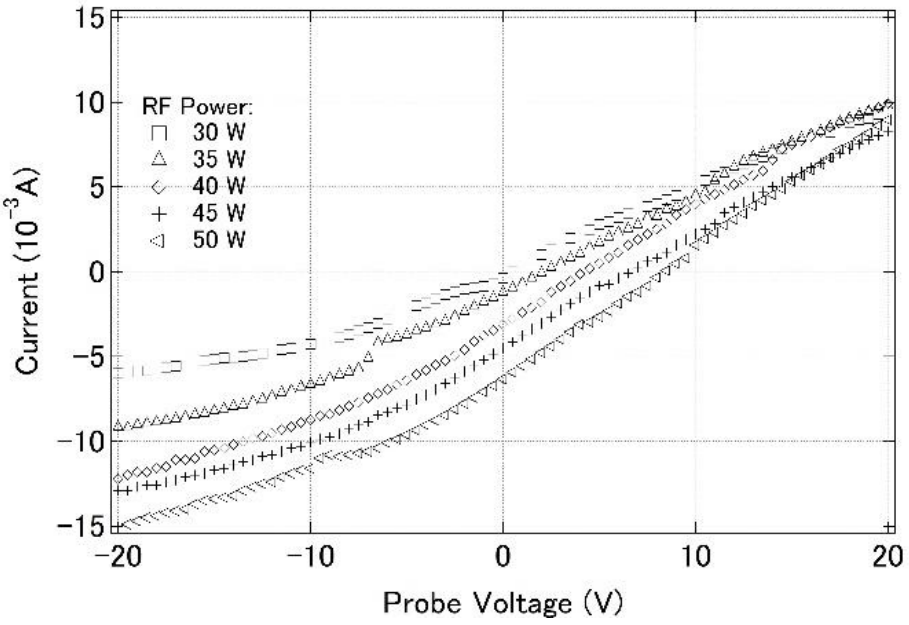

Figure 7.4 *I-V* measurements using various RF power input.

7.3 Summary

Successful electric probe measurements were done when the probe is positioned in the upstream flow of the Ar gas. The plasma potential follows the reference electrode potential which is equal to zero since it is connected to the ground terminal. Rapid increase in the negative current saturation is observed for additional input of RF power and increased Ar gas flow rate since more charge ions and electrons are formed. However, the electrons are trapped inside the plasma sheath due to heating of the probe which resulted in constant positive current saturation win increased RF power and Ar gas flow rate. The values of the slope increase for high RF power and high Ar gas flow rate.

Chapter 8
Conclusions

This dissertation discussed the development of a novel plasma-based ambient desorption/ionization source using inductive coupling. The instrument is designed based upon fundamental theories and fabricated with some practical attempts to optimize the performance. A stable glow is successfully produced by the device. A detailed summary of the results is discussed in the remainder of this chapter. Future prospects on the further development of the new technique are also presented.

8.1 On the design of atmospheric pressure inductively coupled plasma

The first design of the 13.56 MHZ RF atmospheric ICP developed as shown in Figure 8.1. The device is small, portable, and easy to ignite using low power (<100 W) and low Ar gas input (1-5 L/min). The impedance of the circuit is minimum using with 50-80% capacitance loading in matching network capacitor and 2-3 mm coil wire diameter. Ignition power depends on coil wire diameter, gas flow rate, and plasma load. E-discharge facilitates the ignition of the plasma.

Improvement in the ICP was done by using a built-in capacitor presented in Figure 8.2. The built-in capacitor minimized the stray capacitance and parasitic inductance in the circuit resulting in consistent temporal reflected power measurements. The improved design lead to possible changes in the number of coil turns of the inductor

and changes in the coil positions. A better coupling was observed with more number of turns up to twelve. However, the improvements from increasing the turns from six to twelve were not substantial.

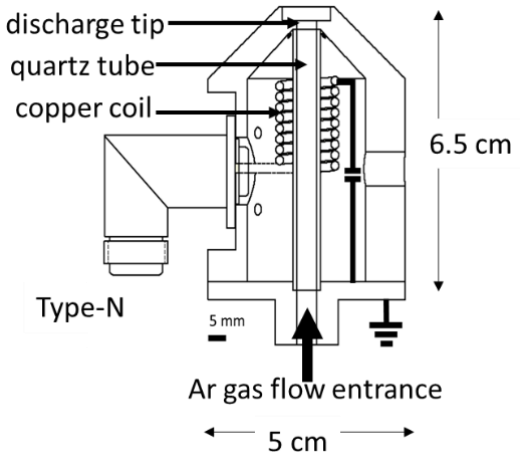

Figure 8.1 The schematic diagram of the first design of the 13.56 MHZ RF atmospheric ICP that was developed as plasma-based ADI.

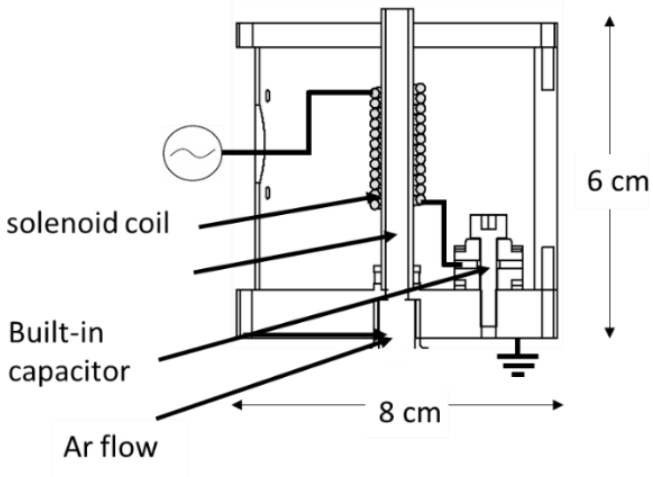

Figure 8.2 Schematic diagram of an improved design of the ICP with a built-in capacitor which minimized the stray capacitance and parasitic inductance in the circuit resulting in consistent temporal reflected power measurements.

Further improvements in the ICP is done by employing a permanent magnet shown in Figure 8.3. The magnet improved the ignition characteristics for 4-5 L/min Ar plasma. The polarity of the magnetic field affects the plume length. Increased collision of positive and negative ion results in equilibrium of positive and negative ion densities.

The grounded wire electrode was added to the system to improve ignition characteristics and plasma stability. The schematic diagram of the wire-stabilized atmospheric pressure ICP is shown in Figure 8.4. Low power ignition, sustaining power, and reflected power in the ICP are observed when using the wire electrode. Improved ignition characteristics were also observed with a change in wire tip location. Ignition power is reduced with increase of the coil turn number.

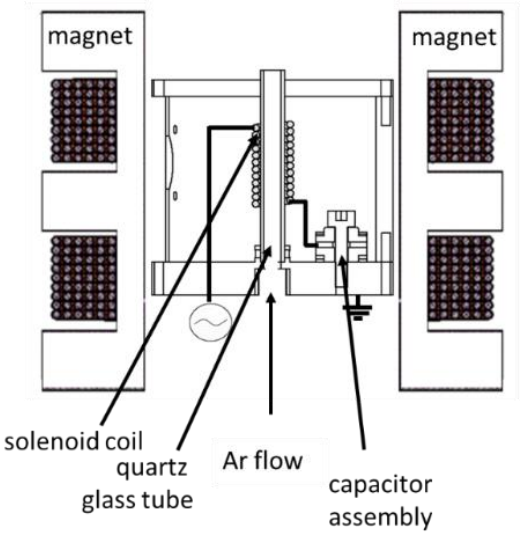

Figure 8.3 Magnet-assisted atmospheric pressure ICP.

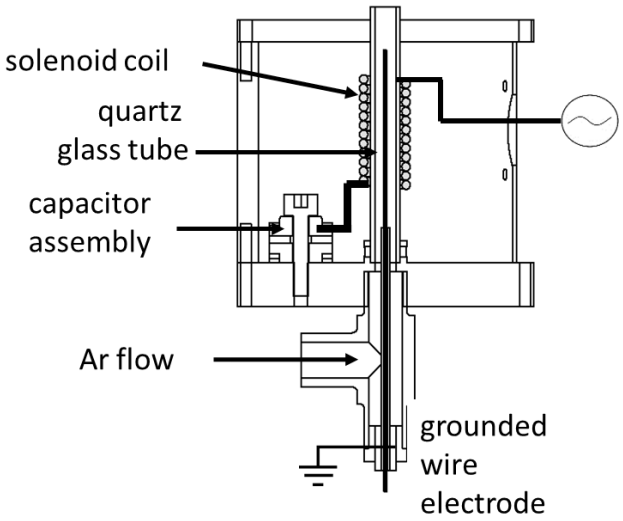

Figure 8.4 Wire-stabilized atmospheric pressure ICP.

8.2 On plasma stability

The homogeneity and stability of the atmospheric pressure plasma are crucial in chemical analysis for a plasma-based ambient desorption/ionization source. The Ar plasma produced using inductive coupling at atmospheric pressure was observed to be a filamentary discharge which is very unstable. A stable homogenous glow plasma was only observed when minimizing the reflected power at 70 W. The homogeneity and stability of the atmospheric pressure plasma are crucial in chemical analysis for a plasma-based ambient desorption/ionization source. The Ar plasma produced by inductive coupling at atmospheric pressure often exhibited filamentary discharge which is very unstable. A stable homogenous glow plasma was only observed the discharge was started at 70 W, and then the reflection power was reduced.

Diagnostics of the filamentary and homogenous glow plasma reveals greater line intensity of the emission spectrum of the filamentary discharge compared with the homogenous glow plasma. The maximum intensity for both modes of operation is

observed at 763.5 nm. Moreover, both modes of operation showed the same line intensity distributions.

Coupling the device to Gerdien condenser, also known as an aspiration ion mobility spectrometer, results in higher total ion density measurements in filamentary discharge compared to the homogenous glow plasma. The filamentary discharge also contains a broader ion spectrum with higher mobility values than in homogenous glow plasma. Identification of the presentions from the *I-V* measurements of the Gerdien condenser reveals the presence of argon, nitrogen, and oxygen ions. It is also observed that O^+ has a minimum density in an inhomogenous glow which is maximum density in filamentary discharge. The observed spectra for the two different modes particularly filamentary discharge shows the presence of large molecules of low mobilities.

8.3 On magnetic enhancements

The minimum magnetic flux density to cause significant effects in the plasma depends on the local electric field applied according to the generated equation when comparing the Larmor radius and mean free path. Results show significant effects of increased magnetic flux to Ar plasma plume where the plume length increased with positive magnet polarity and it decreased with negative polarity. The increased magnetic flux also affects the total ion density measurements. The ion density of nitrogen (N_2^+, O_2^+) drastically increased to 400 Gauss. Although the magnetic flux has significant effects on the ignition characteristics, plasma plume, and ion density, the intensity of the magnetic flux for the electromagnet and that for the permanent magnet is not sufficient to stabilize the atmospheric pressure plasma.

8.4 On wire stabilized atmospheric pressure plasma

The stability of an atmospheric pressure plasma source (APPS) for ion mobility spectrometer applications was investigated. Optimizations of the APPS for the operating conditions such as coil size and position for a plasma inductive excitation and the ignition wire location were attempted. Ignition of Ar plasma is facilitated by the difference in electric potential inside the coil and the distance between the coil and the aluminum base attached to the ground terminal. Characterization of the ignition conditions, *I-V* measurements using a Gerdien condenser, and noise level in the ion current output signals were done for the developed APPS. The insertion of the ignition wire was found to affect the amplitude and value of the transported ion current through the Gerdien condenser.

Smooth ignition of Ar plasma is facilitated by inserting a metal wire inside the glass tube held in the RF coil winding. Improved ignition was also observed with a change in wire tip location. The insertion of ignition wire tip results in more signal but it also increased the noise on the collected current. The power necessary to ignite Ar plasma by the developed APPS was reduced with an increase of the coil turn number and a decrease in the coil aluminum base distance.

8.5 On electric probe measurements

The ionization process in the wire stabilized atmospheric pressure plasma is studied using a double electric probe. Noise amplitude and current offset are observed from the *I-V* measurements. The heating of the ignition wire mainly caused the increase in noise amplitude and offset in the *I-V* measurements of the double probe. The electron temperature appeared to range from 5.1 eV to 6.3 eV. Positive bias voltage increased

the positive current saturation whilst negative bias voltage decreased the negative current saturation. The bias voltage substantially reduced the slope of the *I-V* curve indicating lower temperature.

Due to the presence of the ignition wire which is connected to the ground terminal, the floating potential of the plasma remained fixed near the zero potential. This lead to the counter double electrostatic probe. Asymmetric *I-V* measurements are collected due to the counterflow of ions and electrons in one of the probes.

The current hysteresis in the *I-V* measurements is observed which is associated with the impurities in the ignition wire. The properties of the surface of the ignition wire are unstable through time caused by thermal fluctuations from turning the device on and off. This presence of hysteresis in the *I-V* measurements, therefore, suggests the desorption process in the ignition wire caused by the surrounding energetic atmospheric pressure plasma.

8.6 On electric probe monitoring for simultaneous spectrometer applications

Successful electric probe measurements were done when the probe is positioned in the upstream flow of the Ar gas. The plasma potential follows the reference electrode potential which is equal to zero since it is connected to the ground terminal. Rapid increase in the negative current saturation is observed for additional input of RF power and increased Ar gas flow rate since more charge ions and electrons are formed. However, the electrons are trapped inside the plasma sheath due to heating of the probe which resulted in constant positive current saturation win increased RF power and Ar

gas flow rate. The values of the slope increase for high RF power and high Ar gas flow rate.

8.7 Further work

In this study, the wire stabilized atmospheric pressure plasma is coupled to the ion mobility spectrometer to analyze the plasma stability, measure ion density, and identify the ions present in the plasma. For future works, coupling the wire stabilized atmospheric pressure plasma to a mass spectrometer would establish a more powerful analytical device. Figure 8.5 shows the schematic diagram of the wire stabilized atmospheric pressure plasma -mass spectroscopy. Instead of an ignition wire, a needle connected to a bias voltage source would facilitate the introduction of sample analyte. The bias voltage would control the input of ions to the mass spectrometer.

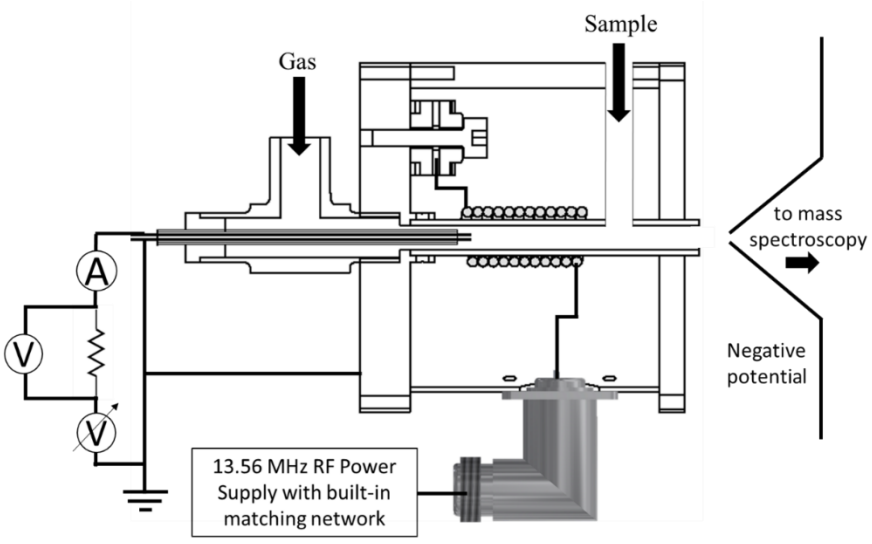

Figure 8.5 schematic diagram of the wire stabilized atmospheric pressure plasma - mass spectroscopy

References

[1] A. Albert, J.T. Shelley, C. Engelhard, Anal. Bioanal. Chem. 406 (2014) 6111–6127.
[2] R.B. Cody, J.A. Laramée, H.D. Durst, Anal. Chem. 77 (2005) 2297–2302.
[3] S.K. Guharay, P. Dwivedi, H.H. Hill, IEEE Trans. Plasma Sci. 36 (2008) 1458–1470.
[4] T.R. Covey, B.A. Thomson, B.B. Schneider, I. Introduction, (2009) 870–897.
[5] C.G. Herbert, A.A.W. Johnstone, MASS BASICS, n.d.
[6] A. Bierstedt, U. Panne, K. Rurack, J. Riedel, J. Anal. At. Spectrom. 30 (2015) 2496–2506.
[7] D. Pröfrock, A. Prange, Appl. Spectrosc. 66 (2012) 843–868.
[8] E.J. Tonnis, D.B. Graves, J. Vac. Sci. Technol. A Vacuum, Surfaces, Film. 20 (2002) 1787–1795.
[9] M.L. Vestal, Chem. Rev. 101 (2001) 361–375.
[10] S. Trimpin, E.D. Inutan, T.N. Herath, C.N. McEwen, Anal. Chem. 82 (2010) 11–15.
[11] M.I. Boulos, P.L. Fauchais, E. Pfender, Handbook of Thermal Plasmas, 2016.
[12] P.K. Chu, X. Lu, Low Temperature Plasma Technology, 1st ed., CRS Press, Florida, 2014.
[13] P.J. Misra, N. N., Schluter, O. K., Cullen, Cold Plasma in Food and Agriculture: Fundamentals and Applications, Academic Press, India, 2016.
[14] M.I. Boulos, P.L. Fauchais, E. Pfender, Handbook of Thermal Plasmas, 2017.
[15] A.D. Weiss, Tech. Instrum. Anal. Chem. 15 (1994) 91–128.
[16] Z.F. Ding, G.Y. Yuan, W. Gao, J.C. Sun, Phys. Plasmas 15 (2008).
[17] J. Hopwood, Plasma Sources Sci. Technol. 109 (1992) 109–116.
[18] H. Lee, I. Yang, K. Whang, 383 (1996).
[19] R. Safari, F. Sohbatzadeh, Indian J. Phys. 89 (2015) 495–502.
[20] S. Pekárek, Eur. Phys. J. D 56 (2009) 91–98.
[21] D.C.M. Field, IEE Transasactions Ind. Appl. 35 (1999) 1198–1204.
[22] W. Jiang, J. Tang, Y. Wang, W. Zhao, Y. Duan, Appl. Phys. Lett. 104 (2014) 1198–1204.
[23] H. Zhang, F. Zhu, X. Li, K. Cen, C. Du, X. Tu, Plasma Chem. Plasma Process. (2016) 1–22.
[24] R. Sato, D. Yasumatsu, S. Kumagai, K. Takeda, M. Hori, M. Sasaki, Sensors Actuators A. Phys. (2013).

[25] F.J.J. Peeters, R.F. Rumphorst, M.C.M. van de Sanden, Plasma Chem. Plasma Process. 38 (2018) 63–74.
[26] P.R. Smy, Adv. Phys. 25 (1976) 517–553.
[27] S. Yan, H. Kamal, J. Amundson, N. Hershkowitz, Rev. Sci. Instrum. 67 (1996) 4130–4137.
[28] K.G. Xu, S.J. Doyle, J. Vac. Sci. Technol. A Vacuum, Surfaces, Film. 34 (2016) 051301.
[29] E.Y. Wang, N. Hershkowitz, T. Intrator, C. Forest, Rev. Sci. Instrum. 57 (1986) 2425–2431.
[30] J.P. Sheehan, N. Hershkowitz, Plasma Sources Sci. Technol. 20 (2011).
[31] M.A. Fink, M. Endler, T. Klinger, Contrib. to Plasma Phys. 44 (2004) 668–676.
[32] D. Strele, M. Koepke, R. Schrittwieser, P. Winkler, Rev. Sci. Instrum. 68 (1997) 3751–3754.
[33] S. Saito, M.A. Razzak, M.R. Talukder, (2010).